2014

Solitary waves in colloidal media

Amirah Azmi
University of Wollongong

Solitary waves in colloidal media

Amirah Azmi

A thesis submitted in the fulfilment of the requirements for

the award of the degree of
Doctor of Philosophy

School of Mathematics and Applied Statistics
University of Wollongong
Australia

September 2014

Thesis supervisor: Professor Timothy Marchant

I, Amirah Azmi, declare that this thesis, is wholly my own work unless otherwise referenced or acknowledged. The document has not been submitted for qualifications at any other academic institution.

Amirah Azmi

3 September 2014

Dedicated to

My dear husband,

Faizal Amri

and

My beloved parents,

Haji Azmi & Hajjah Kartini

Acknowledgement

First of all, I would like to express my special appreciation and gratitude to my supervisor, Professor Timothy Marchant, you have been a tremendous mentor for me. Your advice, expertise, and understanding have been very priceless to make this thesis possible.

I would also like to thank my husband for his love, kindness and support he has shown during the past one year it has taken me to finalize this thesis. Your emotional and spiritual supports keep me going strong. Furthermore I would also like to thank my parents for their endless love and support. Without them, I might not have the opportunity nor the motivation to complete this work.

Special thanks to the staff and fellow students of the School of Mathematics and Applied Statistics who have given time to help me reach this goal. I am also very thankful to the financial supporters of this research; the Ministry of Higher Education Malaysia and Universiti Sains Malaysia.

On top of all the names listed above, I would want to thank God the Almighty for all the chances He has given me to make this thesis becomes surreal.

Abstract

Spatial solitary waves in colloidal suspensions of spherical dielectric nanoparticles are considered. If a laser light beam passes through a colloidal suspension, which consists of spherical dielectric nanoparticles, then the light beam will attract the nanoparticles, increasing the refractive index and creating an optical spatial soliton. Both the one-dimensional and two-dimensional solitary waves are considered with the hard disk and hard sphere theoretical models discussed together with results for a temperature dependent model. The interaction between the colloidal particles in the classical hard disk and sphere models are repulsive and for the temperature dependent model, the interaction between the particles can represent repulsive or attractive interactions. The interaction, or compressibility, of the colloidal particles, is modelled using a series in the particle density, or packing fraction, where the virial (or series) coefficients depend on the type of interaction model. Experimental results show that particle interactions can be temperature dependent and repulsive or attractive in nature, so we model the second virial coefficient using a physically realistic temperature power law.

Semi-analytical solitary waves, for one-dimensional and two-dimensional cases, are derived using an averaged Lagrangian and suitable trial functions for the solitary waves. Power versus propagation constant curves and neutral stability curves are obtained for both cases, which illustrate that multiple solution branches occur for the one-dimensional and two-dimensional cases. For the one-dimensional case, it is found that three solution branches (with a bistable regime) occur, while for the two-dimensional case, two solution branches (with a single stable branch) occur in the limit of low background packing fractions. The temperature dependent properties result in changes to the stability of the solitary waves, which are fully explored.

We also consider the diffraction of an optical beam in a colloidal media, for which an initial jump, or discontinuity, is resolved into a dispersive shock wave. The one-dimensional semi-analytical colloidal solitary wave solutions are used together with con-

servation laws to obtain a semi-analytical description of the amplitude of waves formed at the shock. When the background packing fraction is low, multiple solution branches occur for amplitude versus shock height response curve. Three solutions branches occur, with the upper stable branch detached from the unstable middle branch. At moderate background packing fraction values, an S-shaped response curve exists with all branches occurring for physically realistic parameters. When the background packing fraction is high, only a single stable solution branch occurs. This means that for low and and moderate background packing fractions, the solutions can bifurcate to the high amplitude branch, as the shock height increases.

The hard disk, hard sphere and temperature dependent models are used to describe the one-dimensional case (a line DSW), while for the two-dimensional case (a circular DSW), the hard sphere and temperature dependent models are considered. For the two-dimensional case (circular DSW) at large radius, the one-dimensional analytical results, together with geometrical considerations, provides useful semi-analytical predictions. The semi-analytical predictions and the numerical solutions are found to be in close agreement for both one-dimensional and two-dimensional dispersive shock waves.

Table of Contents

Chapter 1

Introduction and literature review

1.1 Brief history of solitary waves

The initial observation of a soliton was made by John Scott Russell, due to a chance observation on the Edinburgh-Glasgow Canal in 1834. He termed it the great wave of translation and reported to the British Association in his 1844 paper, Report on Waves, see Russell [1]. This phenomenon was later termed a solitary wave in recognition of its single pulse structure. Not long after that, Boussinesq and Rayleigh were among the first researchers who carried out theoretical investigations of solitary waves [2, 3]. Since then, the study of solitary waves has grown to a major field of investigation for mathematicians, physicists and engineers, mainly due to the pioneering paper of Zabusky and Kruskal [4].

In 1895, the Dutch professor Diederik Korteweg and his doctoral student Gustav de Vries (1895) derived a partial differential equation (PDE), the Korteweg de Vries (KdV) equation,

$$u_t + 6uu_x + u_{xxx} = 0, \tag{1.1}$$

which models the solitary wave that Russell had observed. They went beyond the common linear water wave theory to obtain a weakly nonlinear long wave expansion that

describes the solitary wave, see Korteweg and Vries [5]. They made a complete analysis of the solitary wave phenomenon and obtained the invariant pulse like solution for solitary waves, which is consistent with Russell's description of the solitary wave. The second and third terms of (1.1) represent the nonlinear and dispersion effects, respectively. Nonlinearity causes wave steepening, while the dispersion causes the wave to spread. Due to the competition between these two effects, a stable solitary wave exists. Thus, the KdV equation is based on the idea that there exists a balance between the effects of dispersion and nonlinearity.

Zabusky and Kruskal [4] in 1965 found numerical solutions of the collision of solitary waves in a nonlinear crystal lattice. The KdV equation appears as the continuum limit of the one-dimensional anharmonic lattice used by Fermi *et al.* [6], to investigate thermalization. They explored how energy is dispersed among the many possible oscillatory modes. For the solitary wave collisions, they observed that each of the waves retains its shape and speed after they collided. The interacting solitary waves only experience a phase shift, the faster wave moving ahead and the slower wave falling behind, their position without collision. They also coined the word soliton to describe the particle-like behaviour and elastic collision of the solitary waves.

Since the 1970's, the concept of soliton has sparked great interest and the KdV equation and other soliton equations have received great attention, including the exploration of the physical properties and the elegant mathematical theories to describe soliton behaviour. The completely integrable soliton models can be solved using the Inverse Scattering Transform (IST), one of the most important transformations, along with the Fourier Transform, see [7–9]. The IST technique allows an exact solution to be obtained for the KdV equation, see Gardner *et al.* [10]. Since then, the KdV equation has been listed as one of a class of integrable equations, see Newell [11]. Besides the KdV equation, the IST technique can be applied to any integrable equation and allows exact solutions, such as the two-soliton solution to be found. Interacting N-soliton solutions can also be found by Hirota's method [12]. This method quickly proved to be useful in producing solutions of

equations such as the KdV, modified-KdV, Sine-Gordon, and the nonlinear Schrödinger (NLS) equations, see Ablowitz and Clarkson [9].

In many physically important nonlinear problems, the NLS equation is the key model equation

$$iu_t + u_{xx} + 2|u|^2 u = 0. \tag{1.2}$$

The NLS soliton solution occurs due to a balance between dispersion and nonlinear effects. This happens because there is a balance between linear dispersion (u_{xx}, which tends to break up the wave packet) and the self-focusing effect of the cubic nonlinearity ($|u|^2 u$, produced by self interaction of the wave with itself).

The fields for which the NLS is relevant include quantum mechanics, nonlinear water waves, plasma waves, propagation of heat pulses in a solid, self trapping in nonlinear optics, nonlinear waves in a fluid-filled viscoelastic tube, and various nonlinear instability phenomena. The NLS equation is found to describe the evolution of the envelope of modulated wave groups. In 1968, Zakharov [13] described the Hamiltonian structure of water waves in which, for slowly modulated wave groups, the wave amplitude approximately satisfies the NLS equation. The NLS equation was used to consider modulation instability of wavetrains. For waves on deep water, NLS envelope solitons occur and are unstable, see Zakharov [14]. Ma [15] derived other exact NLS solutions which describe the focussing of an initially non-small perturbation and such solutions have been considered as prototypes of rogue waves [16, 17].

The study of optical solitary waves has become an important subject in telecommunications theory because of their capacity of propagating long distances without attenuation, [18, 19]. When the pulse amplitude is small, the NLS equation is used to describe the propagation of light pulses in Kerr media. When the light intensity is higher, then the non-Kerr effects must be included and a NLS equation with higher order terms is needed to describe the propagation of optical pulses in fibers. There are various higher-orders terms which can be included such as third order dispersion, self steepening, the nonlinear

dispersion of the Kerr coefficient and stimulated Raman scattering, see Mitschke and Mollenauer [20]. In the optical context, the NLS equation was first derived from Maxwell's equations, by Hasegawa and Tappert [21] and experimental optical solitons were first observed by Mollenauer *et al.* [22]. It assumes slow variation in the carrier envelope and that the refractive index is linearly dependent on the optical intensity (Kerr dependence), see Zhang and Si [23].

In 1972 Zakharov and Shabat [24] showed that the IST is applicable to the initial value problem (IVP) for the NLS equation. It was the second nonlinear pde whose IVP was discovered to be solvable via the IST method. This was indeed an important discovery because it showed that the IST method was a general one. The associated linear eigenvalue problem for the NLS equation is much more complicated that the KdV case, where the linear Schrödinger equation was solved. Wadati [25] solved the modifed KdV (mKdV) equation and in 1973, Ablowitz *et al.* [7, 26] showed that the IVP for the Sine-Gordon equation is also solvable by the use of the IST. Since then, the IST method has been used to find exact solutions to many other integrable PDEs.

Solutions of the NLS equation (1.2) can be obtained by various methods. These include the use of a Darboux transformation [27], Bäcklund transformation [28], the bilinear method of Hirota [29], and various other techniques [30] based on choosing a solution and adjusting various parameters. The Darboux and Bäcklund transformations are used to obtain new solutions of (1.2) by using the previously known solutions. The Hirota method represents the solution as a ratio of two functions and determines these two functions by solving some corresponding coupled differential equations. The method allows one- , two- and N-soliton solutions to be constructed analytically.

For a general class of nonlinear dispersive wave equations Whitham [31] derived modulation equations to describe the evolution of the fully nonlinear single-phase wavetrain whose parameters (amplitude, wave number and frequency) are slowly varying with respect to the phase in the wavetrain. The idea behind Whitham's theory is to average the

equations for the slow evolution of the parameters over the fast oscillations which leads to a system of pdes for the slowly varying parameters [31, 32]. He used two basic methods to develop modulation equations, via averaged conservation laws [32], and later via an averaged Lagrangian [31]. The amplitude, wavelength and frequency of rapid oscillations associated with the fast scale are assumed to vary adiabatically on the slow scale. The solution, in the form of a slowly modulated wavetrain, was formally constructed by Luke [33] and then extended to the multiphase case by Ablowitz and Benney [34].

The properties of the single phase modulation equations has been described in Whitham [31]. When the modulation equations are strictly hyperbolic, he found that the slowly varying travelling wave is modulationally stable, whereas long wavelength instabilities arise when the equations are elliptic. Therefore, when the modulation equations are strictly hyperbolic, the distinct characteristic speeds are interpreted as the nonlinear generalization of linear group velocity. For general nonlinear dispersive wave equations, most of the additional analysis of the modulation equations is restricted to the small amplitude limit. On the other hand, when the underlying nonlinear wave is integrable, its modulation equations enjoy special properties.

Whitham applied his modulation theory to the KdV equation (1.1) and modulation theory has become an important analytical tool for understanding the evolution of IVP in the KdV system and other hyperbolic systems [32]. Hyperbolic modulation equations possess a simple wave solution which describes an undular bore [35, 36]. This solution describes the resolution of a jump or shock into a dispersive shock wave (DSW), with solitons at the leading edge and linear waves at the trailing edge. The wave properties are given in terms of Elliptic functions. Marchant [37] identified another kind of undular bore problem that consists of sinusiodal waves of finite amplitude as the solution of the mKdV undular bore problem, for certain parameter regimes. He found that there is a difference between the mKdV lead soliton amplitude and the KdV prediction for which the step in mean level is determined by a partial undular bore and a mean height variation that occurs at the same time.

Later, it was realized that there are also a number of important connections between the Whitham theory, the inverse scattering transform (IST) and the general theory of integrable hydrodynamic systems [38]. Flaschka *et al* [38] also derived the general case of modulated quasi-periodic N-phase solutions of the KdV equation in their fundamental paper. This method also permits one to obtain the Whitham equations governing the modulations of sine-Gordon [39] and NLS [40] wavetrains.

For integrable systems, the modulation equations can be set into Riemann invariant form. We may then obtain an explicit result for the simple wave solution that describes an undular bore, see Flaschka *et al.* [41]. Usually, it is not possible to set the modulation equations into Riemann invariant form if the governing equation is not integrable. In these cases, the modulation equations need to be solved numerically or an approximation used obtain the amplitude of the lead soliton. A general approach to determine properties of the leading and trailing edges of the bore has been developed, see El *et al.* [42, 43]. This method requires that the governing equations are hyperbolic outside of the bore region. For elliptic modulation equations, modulational instability (MI) occurs and the IVP is ill-posed and no stable DSW solution exists. However, it is possible that a DSW will form on a length or time scale before the onset of MI, see Assanto *et al* [44].

Marchant and Smyth [45] developed a technique for obtaining the approximate amplitude of the solitary wave at the leading edge in an undular bore for general nonlinear wave equations like the KdV equation, the modified KdV and the Benjamin Ono equation as well as the NLS equation. This technique is applicable to many other equations, providing good predictions for systems with stable undular bore solutions and also for applications, from nonlinear optics, governed by focusing equations for which the bore is unstable.

Grimshaw and Smyth [46] derived a forced KdV equation governing the stratified flow of a fluid over an obstacle. For positive forcing, the flow upstream of the forcing is very nearly a train of solitons. Downstream of the forcing, a flat depression occurs, together with a modulated cnoidal wavetrain which bring the disturbance back to zero. Smyth

[47] considered the near-resonant flow of a stratified fluid over topography in the weakly nonlinear long wave limit. He constructed the upstream and downstream solutions of the topography as simple wave solutions of the KdV modulation equations. Grimshaw and Smyth [46,47] found that the resonant solutions occur only for a resonant band depending on the forcing. The solution is similar to the linear, non-resonant solution, outside this resonant band.

1.2 Solitary waves in colloidal media

Spatial solitary waves are self-trapped optical beams for which there is a balance between nonlinearity and diffraction. The nonlinearity is due to an intensity dependent refractive index, such as the Kerr response, see [48,49]. A planar dielectric waveguide is an example of such a waveguiding system. For spatial solitons in (1+1)-D, propagation occurs along one coordinate (say, z) and guidance occurs along a single transverse coordinate x with the assumption that the guided beam is uniform in the other transverse direction y. For a (2+1)-D waveguiding system, spatial guidance occurs in both transverse dimensions, an example being optical fibres, see [50].

Over recent years, the phenomenon of optical spatial solitary waves has been widely explored, experimentally, theoretically and numerically, for many media, including nematic liquid crystals, [51], photorefractive crystals [52], lead glasses [53] and thermal media [54] and many other optical media. One example is soft media, so termed because they have properties in between those of liquids and solids. In the last two decades, a new generation of optical techniques has emerged, and the mechanical interaction between light and soft matter has received considerable attention.

One of the more interesting materials that supports spatial solitary waves is nematic liquid crystals (NLCs). This is due to their unique physical and optical properties. The nature of the medium-light beam interaction is reorientional as the dipole like molecules

reorientiate according to the light intensity, changing the refractive index. The existence of solitary waves in NLC systems has been investigated from both from theoretical and experimental points of view [55–59], with one of its experimental advantages being a large nonlinear response, over a short propagation distance.

Assanto and Peccianti [60] briefly identified several characteristics which contribute to make NLCs an ideal medium for the investigation of spatial solitons, their interactions, and various applications. They found a nonlinearity orders of magnitude larger than in standard Kerr-like materials, allowing self-localization effects to take place in NLC at milliwatt power levels under proper anchoring and biasing conditions. Assanto and Kapierz [61] reviewed the substantial developments on light self-localisation into spatial optical solitons. They also summarized the basic physics and models, outlined the main properties of NLS solitary waves (termed nematicons) and provided a summary of successful experiments in undoped, planar, twisted and chiral nematic liquid crystals.

In the early 1970s, Arthur Ashkin built the first three-dimensional optical traps at the Bell Telephone Laboratories and over the years, the newly established laser trapping and manipulation techniques were found to work on a wide range of particle types that includes colloids, see Ashkin [62]. Optical traps use the propagation of light in order to manipulate microscopic objects as small as 10 nanometers using the radiation pressure from a focused laser beam. Other than the mechanism discussed above, there is another mechanical mechanism that can also give rise to an optical nonlinearity which is termed electrostriction. Electrostriction is caused by dielectric polarization in an electric field and causes dielectric particles to drift towards regions of high electric field intensity.

In the most basic form of an optical trap as shown in figure 1.1(a), a light beam is focused to a spot in the specimen plane where the radiation pressure from the light beam is able to trap small particles. This spot produces an 'optical trap' which allows small particles to be held at its centre. Figure 1.1(b) shows how the interaction of the particle with the light will cause the detection of light scattering and the gradient forces. Most

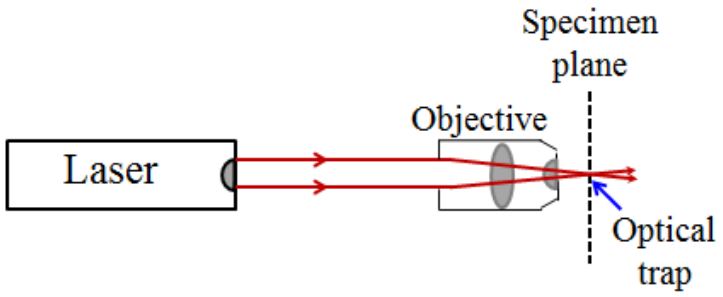

(a)

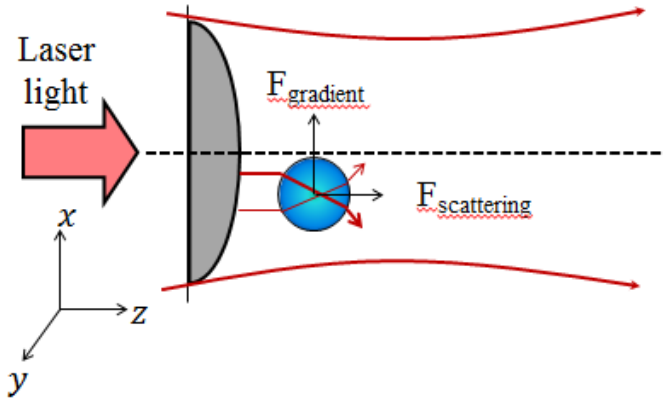

(b)

Figure 1.1: (color online) The basic principles of optical traps

studies in the field consider the emergence of new tools in optics such as optical tweezers and traps while some possible new applications in colloidal media include optical sensors or selective particle trapping and manipulation, see [62–64]. The ideas behind these powerful optical manipulation techniques and recent applications in soft matter science are discussed by Molloy and Padgett in [65], while Kishan *et al.* [66] summarize recent developments in this area.

In this research we focus on one significant part of this broad and interdisciplinary subject, namely spatial solitary waves in colloidal media. Colloidal systems are constructed of particles of size r which are very small to make sure that the surface effects (αr^2) will have a greater influence than the bulk effects (αr^3). It consists of mesoscopically (on a scale between microscopic and macroscopic) large colloidal particles, dispersed in a sol-

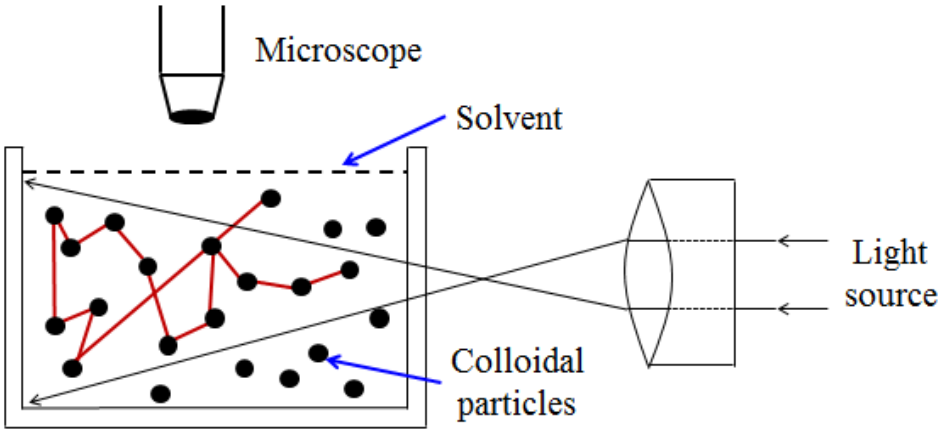

Figure 1.2: (color online) Brownian motion of colloidal particles dispersed in a solvent

vent and are usually a few hundred nanometers in size. According to Levine [67], colloids represent a group of very fine particles dispersed in a solution lying in the approximate range between 1 nanometre and 1000 nanometres.

While atoms are tiny, colloidal particles dispersed in a solvent are big enough to be seen with light and are visible under laser light scattering. The colloidal particles exhibit Brownian motion, where there exist constant bombardment of the particles by the solvent molecules, as described in figure 1.2. It has also been established that the intensity of the Brownian motion is influenced by the temperature. Colloids are a very useful model system for investigating the structure and properties of all sorts of different kinds of colloidal particles dispersed in media, such as crystals, gels, fluids, and gases. The phenomenon of optical spatial solitons has been predicted and demonstrated in numerous colloidal media. Terborg *et al* [68] experimentally observed a light induced waveguide in an artificial nonlinear medium (polystyrene), consisting of a colloidal suspension of dielectric nanoparticles. They also illustrated that the steering of the solitary waves was possible.

In the colloidal medium considered here, the optical forces, due to electrostriction, resulting from the propagation of an optical beam through the medium and causes the concentration of the colloidal particles to change. This will alter the refractive index,

leading to a nonlinear interaction between the colloidal particles and the light beam. So the formation of spatial solitary waves in a colloidal medium is due to the balance between diffraction of the light beam and this nonlinear particle-light interaction.

The compressibility of a colloid is usually defined via the non-ideal gas law where the pressure is given as a function of the density, or packing fraction, in a series form. The nature of the interactions between the colloidal nanoparticles defines the virial coefficients of the perturbation series. The classical theoretical repulsive interaction models are the hard disk model, valid in (1+1)-D, and hard sphere model, valid in (2+1)-D. For these models the virial coefficients can be found using integral theories, for the lower-order coefficients, and numerical simulations for the higher-order ones. Typically a series of nine or ten terms is used but uncertainty in the exact values for the higher-order coefficients leads to uncertainties in the occurrence of phase transitions, from liquid to solid. Many authors have explored the calculation of accurate higher-order virial coefficients for the hard disk and sphere models, see, for example [69–71]. For the hard sphere model, the Carnahan-Starling (CS) formula represents an accurate analytical approximation, valid for low to medium densities. For the hard disk model, the Scaled Particle Theory (SPT) provides a useful approximation at low to medium densities. The compressibility of a fluid is a measure of the change in density that will be produced by a specific change in pressure and temperature. The generalized equation of state, for the compressibility factor is a function of the reduced temperature and pressure. The compressibility factor, Z, is

$$Z = \frac{P}{\rho k_B T} = 1 + B_2\eta^1 + B_3\eta^2 + B_4\eta^3 + \cdots , \tag{1.3}$$

where P is the pressure, ρ is the density, T is the temperature and k_B is Boltzmann's constant, and the B_i are the virial coefficients. The packing fraction η describes the ratio between the volume occupied by the particles and the total volume. The virial coefficients represent the chosen particle interaction model. The virial expansion of the equation of state has long been known to provide an accurate theoretical description for fluids.

Santos *et al.* [71] listed the various theories that can be used to calculate the virial coefficients; SPT [72], Handerson equation [73, 74], Andrews equation [75], Baram and Luban equation [76], Woodcock equation [77], Levin approximant [78] and Padé approximant [79]. For the theoretical models, the first few virial coefficients can be found analytically. However, for real fluids, the virial coefficients are usually obtained experimentally. A variety of experimental methods have been applied to determine the virial coefficients for the compressibility formula of the colloidal mixtures. However, these measurements usually give only the the second and third virial coefficients. Most studies focus on obtaining the second virial coefficients and data are readily available in previous works for many gases and colloids, see Dymond [80]. However, the third coefficients and any other higher virial coefficients are usually not available.

Two long standing theoretical particle interaction models are the hard disk (HD) and hard sphere (HS) models, valid in (1+1)-D and (2+1)-D, respectively. Maeso *et al* [69, 70] considered the HD and HS fluids by using current available accurate values for the first ten coefficients. Tian *et al.* [70] extended the asymptotic expansion method to arrive at a new equation of state with values for the higher coefficients. The proposed virial coefficients and compressibility factor accurately reproduces the results obtained using computer simulations in both the stable and meta-stable ranges. Maeso and Solana [69] obtained the equation of state from a generalization of the CS approximation, by a direct summation of the virial series.

Studies on colloidal solitary waves by [81–83] represented the colloidal suspension using the HS model with the CS formula used to describe the compressibility factor. The colloidal equations were derived in one and two spatial dimensions, and numerical results for exact propagation constant versus power curves of the colloidal solitary waves were obtained. Matuszewski *et al.* [82] used the hard-sphere CS formula and derived numerically exact propagation constant versus power curves for the (1+1)-D and (2+1)-D cases. In the (1+1)-D case they found bistable behaviour and examined solitary wave interactions for solitary waves of the same power, from the same and different solution branches.

Qualitatively different interactions occurred for solitary wave interactions for waves from the same and different branches. Matuszewski *et al* [83] considered a colloidal suspension of two different types of nanoparticles. One type was approximated by the CS formula, for which the refractive index is higher than the background medium and the other has refractive index lower than that of the background medium. Numerical solitary wave solutions showed that bistability can occur in the (2+1)-D case, but does not occur for the single nanoparticle species case.

Marchant and Smyth [81] considered the hard-sphere CS model to obtain semi-analytical solutions via an averaged Lagrangian approach, where trial functions are chosen for the solitary waves. The semi-analytical solutions allowed accurate estimates, of the regions of parameter space, for which multiple solution branches occur, to be found. Azmi and Marchant [84] found the (1+1)-D and (2+1)-D semi-analytical solitary colloidal wave solutions for which the colloidal particle compressibility has a general series form. Their results were presented for the repulsive HD and HS models and for a temperature dependent model where the second virial coefficient can change sign, from repulsive to attractive. They also provided a detailed explanation on the effect of varying the temperature, on the properties of the solitary waves.

Focusing on real colloids, for both pure substances and colloidal mixtures, many experimental results are available for the second virial coefficient, which describes the leading density dependent correction to the ideal gas law. This is regarded as one of the key thermodynamic properties and is closely related to the intermolecular forces between two molecules, and is usually temperature dependent, see Harvey and Lemmon [85]. Striolo *et. al* [86] obtained experimental results for semiconductor nanocrystals in a Toluene solution. Experimental results show that the second virial coefficient is an increasing function of temperature, with the coefficient changing from a negative value to a positive one. This change in sign indicates that the pairwise forces on the molecules change from attractive to repulsive as the temperature increases. Striolo *et. al* [87] considered synthetic polymeric materials with nanoscale particle inclusions, termed polyhedral oligomeric sislesquiox-

anes (POSS). Molecular simulations predict an increase in the second virial coefficient from negative to positive, as temperature increases, for one type of POSS monomers. Another type of POSS monomer initially shows an increase in the second virial coefficient, as the temperature increases, but it then decreases to larger negative values as the temperature rose further.

Tian [88] summarised the behaviour of the second virial coefficient for many types of fluid. They found that the temperature dependence of the coefficient is accurately modeled by a power law form

$$B_2 = b - \frac{a}{RT^{1+\lambda}}, \tag{1.4}$$

where the parameters a, b and λ are obtained by fitting experimental data, R is the gas constant and T is the temperature.

For colloidal media an initial jump in packing fraction amplitude will be resolved by the formation of a DSW. For a focusing NLS-equation, as is the case in colloidal media, the modulation equations are elliptic and the DSW is modulationally unstable. However, on a short length-scale DSW exists in nematic liquid crystal and colloidal media, see the numerical and experimental studies [89–92]. The propagation of light beams in nonlinear optical media has generated DSW structures [93, 94], where the existence of solitary waves at its leading edge and linear waves at its trailing edge is identified. Hence a DSW plays an important role in providing a smooth resolution of the initial discontinuity.

In 2008 Assanto *et al.* [44] considered the development of bores in a self-focusing NLC medium. They showed that the DSW, caused by the jump, continues for experimentally relevant length-scales due to nonlocality delaying the onset of modulational instability. They considered both (1+1)-D and (2+1)-D cases, termed line and circular bores. By approximating the DSW as a train of uniform solitary waves, they obtained a semi-analytical solution for line undular bores. Both semi-analytical and numerical results were in a very good agreement for the line and circular bores. This semi-analytical solution method was first used to solve a KdV undular bore, and was termed uniform soli-

ton theory. Marchant and Smyth [95] developed the semi-analytical solutions for DSW in colloidal media by using the hard sphere CS model. They found that the results are dependent to the background packing fraction values with three different types of solitary wave amplitude versus jump height diagrams possible.

1.3 Objective

The general objective of this thesis is to examine the stability of colloidal solitary waves and the formation of dispersive shock waves in a colloidal media, described by a focusing NLS equation with a general series form for the compressibility. The thesis aims to answer the following questions:

- Can a series form for the compressibility be used to model colloidal solitary waves?
- Is the averaged Lagrangian trial function method useful in obtaining accurate semi-analytical solutions for solitary waves in colloidal media?
- How do the solutions describe the changes in bistable behaviour that occur at different background packing fractions and temperatures?
- How effective is the semi-analytical model in describing the properties of dispersive shock waves in focusing colloidal media?
- How does the bifurcation patterns describing the solitary wave amplitude as a function of shock height vary with temperature?

Note that in this study the virial coefficients used to describe the compressibility formula correspond to the HS model, HD model and also to a physically realistic temperature dependent model.

1.4 Plan of the thesis

This thesis consists of five chapters. Chapter 2 discusses the modulation theory used in this research to find solutions for solitary waves in colloidal media, for one and two-dimensional cases, for a general compressibility law. Following this, in Chapter 3, semi-analytical power versus propagation constant and neutral stability curves for both (1+1)-D and (2+1)-D colloidal solitary waves are obtained by solving the modulation equations. These curves illustrate the bi-stability behaviour of the solitary wave solution branches and the regions of parameter space in which multiple solution branches occur. The effect of temperature variation for physically realistic colloids is also examined. In chapter 4, we look at the evolution of a DSW in the focusing NLS-type equation describing colloidal media. Uniform soliton theory is developed to obtain a semi-analytical expression for the amplitude of the solitary waves, created by the initial shock or the jump. Bifurcation patterns show three different types of amplitude versus shock height diagrams are possible. These are the unique, S-shaped and separated upper branches patterns. Again, the effect of changes in temperature for physically realistic colloids are examined for the DSW problem. Finally, some concluding remarks and recommendations for future work are discussed in Chapter 5. Appendices and references are at the end of this thesis.

Chapter 2

Modulation equations

2.1 Introduction

In this chapter, we present the governing equations for solitary wave propagation in colloidal media and develop modulation equations for the semi-analytical solutions. The Nonlinear Schrödinger (NLS) type equation that governs the nonlinear propagation of the beam through a colloidal suspension, see [82], is

$$\begin{aligned} &i\frac{\partial u}{\partial z} + \frac{1}{2}\nabla^2 u + (\eta - \eta_0)u = 0, \quad |u|^2 = g(\eta) - g_0, \\ &g(\eta) = \ln(\eta) + 2B_2\eta + \frac{3}{2}B_3\eta^2 + \cdots, \quad g(\eta_0) = g_0, \end{aligned} \tag{2.1.1}$$

where u is the electric field envelope, η is the packing fraction of the colloid particles, and η_0 is the background packing fraction. The governing equation is independent of time t but the propagation variable z plays a time like role. Physically it is assumed that the light beam causes the colloidal particles to drift towards the region of higher light intensity, due to electrostriction. Also, the colloidal particles have a higher refractive index than the background liquid medium. So when an optical beam passes through the medium the optical gradient force acts against particle diffusion, increasing the concentration of colloidal

particles and hence the refractive index, in regions of higher light intensity, allowing self-focusing to occur. It is well known that selective scattering (or Rayleigh scattering) might occur when the light beam propagates through individual atoms or molecules. However, in this case, any damping due to Rayleigh scattering can be ignored as the dielectric sphere particle diameter is much smaller than the laser wavelength, see [83, 96].

The relationship $|u|^2 = g(\eta) - g_0$, between the light intensity and the packing fraction, represents an integration of the generalised Fick's law for the optical force on the nanoparticles, see [83, 96]. The particle interactions, or compressibility, is governed by a non-ideal gas law, which is written in series form with general coefficients B_i. The second, B_2, and third, B_3, virial coefficients are written explicitly in (2.1.1). The choice of these coefficients allows the effect of different particle interaction models on the properties of the colloidal solitary waves to be considered. When the packing fraction η is close to the background level, $|\eta - \eta_0| \ll 1$, then $|u|^2 \sim g'(\eta_0)(\eta - \eta_0)$ and the colloid equation (2.1.1) approaches the NLS equation limit,

$$i\frac{\partial u}{\partial z} + \frac{1}{2}\nabla^2 u + \frac{1}{g'(\eta_0)}|u|^2 u = 0. \tag{2.1.2}$$

It is well known that there exists no exact solitary wave solution for the NLS-type equation (1.2) governing colloidal solitary waves, so this study has the objective of serving as a general test for our theoretical techniques. One useful theoretical method for this problem is to use a Lagrangian formulation and choose suitable trial functions [97, 98]. Based on employing a trial function that represents the soliton-like pulse into the variational formulations of the governing equations (2.1.1), it is believed that this is the most useful approximate technique to solve the theoretical solitary wave problem. This method of obtaining semi-analytical solutions is similar to the modulation theory of Whitham and other interrelated perturbation techniques [31].

The colloid equations (2.1.1) have the Lagrangian formulation

$$L = i(u^* u_z - u_z{}^* u) - |\nabla u|^2 + 2(\eta - \eta_0)|u|^2 - 2\eta \ln \eta + 2\eta_0 \ln \eta_0 \qquad (2.1.3)$$
$$+2(\eta - \eta_0)(1 + g_0) - 6\eta - 2B_2\eta^2 - B_3\eta^3 + 6\eta_0 + 2B_2\eta_0^2 + B_3\eta_0^3 + \cdots ,$$

where the asterisk superscript denotes the complex conjugate. Previously researchers have developed approximate solutions for NLS-type equations using a Lagrangian formulation with a choice of suitable trial functions [97, 98]. This is based on employing a trial function, that represents the solitary wave, in the variational formulation of the governing equations (2.1.1). The trial function approximation method has proved to generate very accurate solutions that match the numerical and experimental results closely, see [44, 99]. To obtain accurate solutions for (2.1.1) it is important to identify suitable trial functions for u and η to substitute into the Lagrangian. However, some characteristics of the beam, such as its velocity and position, are independent of the form of the trial functions used for the solitary wave profile, see [100, 101]. Here we apply the technique to (2.1.1) to obtain both (1+1)-D and (2+1)-D solitary waves.

2.2 The (1+1)-D colloidal waves

We will now look at the solitary wave solutions for the (1+1)-D form of the colloid equations (2.1.1), which are functions of the two spatial coordinates, x and z, where z plays the time-like role. We are only concerned here with steady-state envelope solitary waves (where the envelope is only a function of x) and we choose trial functions for the electric field and colloid packing fraction in (1+1)-D as

$$u(x, z) = a \operatorname{sech}\frac{x}{w} e^{i\sigma z}, \quad \eta(x) = \eta_0 + \alpha \operatorname{sech}^2 \frac{x}{\beta}. \qquad (2.2.4)$$

This trial functions consists of a soliton-like pulse with variable parameters plus a

term which represents linear dispersive radiation. The usage of this trial function is also very convenient in deriving approximate equation that describes transient evolution via the Lagrangian formulation of the NLS equation. The choice of trial functions allows the amplitude and width to vary explicitly, see [98]. The solitary wave (2.2.4) can be chosen as stationary without loss of generality, as a non-zero velocity can be scaled out of the equations. The electric field component of the solitary wave is based on the NLS soliton sech profile, which is a close approximation in the $|\eta - \eta_0| \ll 1$ case. The form for the packing fraction η is chosen as a sech^2 profile as η is a function of the light intensity $|u|^2$ and $\eta \to \eta_0$ far from the light pulse. The parameters in equation (2.2.4) are the amplitudes a and α while the widths are w and β and finally σ is the propagation constant of the solitary wave. Note that the amplitudes and the widths of the two pulses are related, as the relation $|u|^2 = g(\eta) - g_0$ implies. A more complete version of the trial functions could be chosen, which describes the evolution of an initial beam, to a steady solitary wave solution, however these details are not necessary for this study.

We may now substitute the trial functions (2.2.4) into the Lagrangian (2.1.3) and the averaged Lagrangian is obtained by integrating in x over the infinite domain, giving

$$\begin{aligned}
\mathcal{L} &= -4a^2 w\sigma - \frac{2}{3}\frac{a^2}{w} + 4\alpha a^2 \Omega_1(w,\beta) - 4\beta\Theta_1(\alpha) \\
&+4\alpha\beta(1+g_0) - 8B_2\alpha\beta\eta_0 - \frac{8}{3}B_2\alpha^2\beta - 6B_3{\eta_0}^2\alpha\beta - 4B_3\eta_0\alpha^2\beta \\
&-\frac{16}{15}B_3\alpha^3\beta, \quad \text{where} \quad \Omega_1(w,\beta) = \int_0^\infty \mathrm{sech}^2\frac{\zeta}{\beta}\mathrm{sech}^2\frac{\zeta}{w}\mathrm{d}\zeta \\
\Theta_1(\alpha) &= \int_0^\infty \left[\eta_0 \ln(1+\frac{\alpha}{\eta_0}\mathrm{sech}^2\zeta) + \alpha\mathrm{sech}^2\zeta\ln(\eta_0+\alpha\mathrm{sech}^2\zeta)\right]\mathrm{d}\zeta.
\end{aligned} \tag{2.2.5}$$

We then take the variations of the averaged Lagrangian (2.2.5) with respect to the

variables w, β, α, and a to obtain the following

$$
\begin{aligned}
&3\alpha w(\Omega_1 - w\Omega_{1w}) - 1 = 0, \;\; \sigma = -\frac{1}{2w^2} + \frac{\alpha}{w}(2\Omega_1 - w\Omega_{1w}), \\
&4a^2\alpha(\Omega_1 - \beta\Omega_{1\beta}) - 4\beta(\alpha\Theta_{1\alpha} - \Theta_1) - \frac{8}{3}B_2\alpha^2\beta - 4B_3\eta_0\alpha^2\beta \\
&-\frac{32}{15}B_3\alpha^3\beta = 0, \\
&\alpha a^2\Omega_{1\beta} - 4\Theta_1 + 4\alpha(1+g_0) - 8B_2\alpha\eta_0 - \frac{8}{3}B_2\alpha^2 - 6B_3\eta_0^2\alpha \\
&-4B_3\eta_0\alpha^2 - \frac{16}{15}B_3\alpha^3 = 0.
\end{aligned}
\tag{2.2.6}
$$

There are three equations for the five unknowns w, β, α, a and η_0 with the propagation constant σ given by an explicit expression. Hence they represent a two-parameter family of solitary waves. By solving these transcendental equations, it is possible to obtain the optical power,

$$P = \int_{-\infty}^{\infty} |u(x)|^2 \mathrm{d}x, \tag{2.2.7}$$

for a (1+1)-D semi-analytical colloidal solitary wave. For the 1-D case, the power of semi-analytical solitary wave is given by $P = 2a^2w$.

From the solution of the equations (2.2.6), we obtain the semi-analytical power versus propagation constant curves. We can conclude that a region of stability is described by solution branches with $\frac{dP}{d\sigma} > 0$. This is the Vakhitov-Kolokolv criterion for solitary wave stability, see Kaplan [102]. Hence, solitary waves of neutral stability have the property $\frac{dP}{d\sigma} = 0$. By adding this condition to (2.2.6), we have a set of four equations for five unknowns. Solving this new set of equations will result in curves of neutral stability that are lines in the σ versus η_0 plane.

2.3 The (2+1)-D colloidal waves

Let us now look at the propagation of a (2+1)-D beam where the modulation equations of the (1+1)-D beam from the previous part are extended. Using a natural extension of those

in (1+1)-D, the trial functions in (2+1)-D are

$$u(x,y,z) = a\text{sech}\frac{\phi}{w}e^{i\sigma z}, \;\; \eta(x,y) = \eta_0 + \alpha\text{sech}^2\frac{\phi}{\beta}, \;\; \phi = \sqrt{x^2+y^2} \tag{2.3.8}$$

Here the waves are functions of the three spatial dimensions but again z is time like, hence they are termed (2+1)-D solitary waves. We will obtain the averaged Lagrangian for the (2+1)-D case by integrating the new Lagrangian with respect to x and y from $-\infty$ to ∞ to get

$$\begin{aligned}
&\mathcal{L} = -1.386a^2w\sigma - 0.3977a^2 + 2\alpha a^2\Omega_2(w,\beta) + 1.386\alpha\beta^2(1+g_0) \qquad (2.3.9)\\
&-2\beta^2\Theta_2(\alpha) - 4.1589\;\alpha\beta^2 - 2.773\;B_2\eta_0\alpha\beta^2 - 0.5909\;B_2\alpha^2\beta^2\\
&-2.080\;B_3{\eta_0}^2\alpha\beta^2 - 0.8863\;B_3\eta_0\alpha^2\beta^2 - 0.1864\;B_3\alpha^3\beta^2,\\
&\Omega_2(w,\beta) = \int_0^\infty \zeta\text{sech}^2\frac{\zeta}{\beta}\text{sech}^2\frac{\zeta}{w}\text{d}\zeta,\\
&\Theta_2(\alpha) = \int_0^\infty \zeta\left[\eta_0\ln(1+\frac{\alpha}{\eta_0}\text{sech}^2\zeta) + \alpha\text{sech}^2\zeta\ln(\eta_0+\alpha\text{sech}^2\zeta)\right]\text{d}\zeta.
\end{aligned}$$

Again, just like in the (1+1)-D case, the variations of the averaged Lagrangian with respect to the variables w, β, α, and a are obtained by following the behaviour of soliton solutions via perturbation theory that yields equations for the evolution of the soliton parameters called modulation equations. By assuming a steady state condition in this (2+1)-D case, we may set $g = V = \xi = 0$ in the modulation equations. The coefficients of (2.3.9) represent integrals, for which explicit exact expressions do not exist, so they are written here to four significant figures. The modulation equations are found by taking the partial derivatives of the averaged Lagrangian, with respect to the variables w, β, α and a. They are

$$
\begin{aligned}
&\alpha(2\Omega_2 - w\Omega_{2w}) - 0.3977 = 0, \;\; \sigma = -\frac{0.5737}{w^2} + 0.7214\frac{\alpha}{w^2}(4\Omega_2 - w\Omega_{2w}),\\
&2a^2\Omega_2 - 2\beta^2\Theta_{2\alpha} + 1.386\beta^2(1+g_0) - 4.159\beta^2 - 2.773B_2\eta_0\beta^2 \qquad (2.3.10)\\
&-1.182B_2\alpha\beta^2 - 2.080B_3{\eta_0}^2\beta^2 - 1.773B_3\eta_0\alpha\beta^2 - 0.5591B_3\alpha^2\beta^2 = 0,\\
&\alpha a^2\Omega_{2\beta} - 2\beta\Theta_2 + 1.386\alpha\beta(1+g_0) - 8.3180\alpha\beta - 5.545B_2\eta_0\alpha\beta\\
&-1.182B_2\alpha^2\beta - 4.159B_3{\eta_0}^2\alpha\beta - 1.773B_3\eta_0\alpha^2\beta - 0.3727B_3\alpha^3\beta = 0,
\end{aligned}
$$

From the transcendental equations (2.3.10) in the (2+1)-D case we obtain a semi-analytical description of the two-parameter family of colloid solitary waves. The optical power is given by

$$P = \int_0^\infty r|u(r)|^2 \mathrm{d}r. \qquad (2.3.11)$$

So that the power of a semi-analytical (2+1)-D solitary wave is given by $P = \ln 2a^2w^2$.

Chapter 3

Bi-stability behaviour of solitary waves in colloidal media

3.1 Introduction

This chapter discusses the semi-analytical solutions for colloidal solitary waves that have been formulated in Chapter 2. The results of this chapter appear in Azmi and Marchant [84]. Both the (1+1)-D and (2+1)-D cases are considered with the HD and HS theoretical particle interaction models discussed together with results for a temperature dependent model. The classical HD model is appropriate in a (1+1)-D geometry, and the HS model is appropriate in a (2+1)-D geometry. For both models, the interaction between colloidal particles is repulsive. However, our interest also involve real colloids with temperature dependent virial coefficients, where the interaction between the particles can represent repulsive or attractive interactions. Further discussion about this, and the effect on solitary wave stability will be described throughout this chapter.

Semi-analytical approximations for the power versus propagation constant and neutral stability curves are obtained. From the power versus propagation constant curve, we can identify the existence of multiple solution branches and determine solitary wave sta-

bility. From the neutral stability curves, parameter values corresponding to the region of parameter space, in which multiple solution branches occur are found.

For the HS and HD models, the virial coefficients used are obtained theoretically or via computer simulation, see Tian et. al [70]. Equation (3.1.1) and (3.1.2) below describe the compressibility series for the HS and HD models. For both models typically five or six series terms are needed, to obtain equivalent results to the CS and SPT theories, at large packing fractions. Here we use the seven term series,

$$Z_1 = 1 + 4\eta + 10\eta^2 + 18\eta^3 + 28\eta^4 + 40\eta^5 + 54\eta^6 + \cdots , \tag{3.1.1}$$

$$Z_2 = 1 + 2\eta + 3\eta^2 + 4\eta^3 + 5\eta^4 + 6\eta^5 + 7\eta^6 + \cdots , \tag{3.1.2}$$

where equation (3.1.1) is the HS series, obtained from Table 3 in Tian *et al.* [70] while equation (3.1.2) is the HD series from Table I in Santos *et al.* [71]. Note that the HS model is appropriate for (2+1)-D geometries while the HD model is appropriate in (1+1)-D geometries.

We also develop a temperature dependent model by using known experimental results as a guide. Tian *et. al* [70] use the following general relationship

$$B_2 = b - \frac{a}{T^{\lambda+1}}, \tag{3.1.3}$$

where the second virial coefficient is given as a power law. Tian *et al.* [70] summarizes the parameter values in (3.1.3) for many different choices of fluid. As the non-dimensional temperature T varies, the second coefficient B_2 can change from positive to negative, which changes the particle interaction forces from repulsive to attractive. To model temperature effects for (1+1)-D colloid solitary waves, we use the HD coefficients (3.1.2) but with (3.1.3) as the second virial coefficient where $B_2 = 2 - \frac{100}{T}$. So in the limit as the temperature becomes large, the model approaches the repulsive HD one, as $B_2 \to 2$. For (2+1)-D colloid solitary waves we use the HS coefficients (3.1.1) but with (3.1.3) as the

second virial coefficient coefficient where $B_2 = 4 - \frac{100}{T}$, so $B_2 \to 4$ as the temperature becomes large. From (2.1.1) we see that, for a given packing fraction, that the wave intensity $|u|^2 = g(\eta) - g_0$ increases as B_2 increases. Hence for a given packing fraction, our chosen temperature dependence (3.1.3) means that higher temperatures are associated with higher wave intensities.

The temperature effects on colloidal solitary waves are explored by using the semi-analytical solutions of (2.2.6) and (2.3.10) for the (1+1)-D and (2+1)-D cases respectively. This choice of B_2 allows us to explore the effects on the solitary waves and their stability as the temperature changes and the interaction forces vary between repulsive and attractive cases. Note that for real fluids all the series coefficients would be temperature dependent but experimental data for higher-order virial coefficients is generally not available, so we only consider B_2 as temperature dependent.

In (1+1)-D the numerical solutions of the colloid equation (2.1.1) are obtained by an analytical integration of the steady-state governing equation, which gives an energy conservation law. The energy conservation law is then numerically integrated to obtain exact solitary wave profiles on all solution branches, both stable and unstable, of the power versus propagation constant curves, see the Appendix for details. In (2+1)-D the imaginary time iterative method (ITEM) is used to obtain numerically exact solitary wave profiles, see Yang and Lakoba [103]. The ITEM does not allow unstable solution branches to be found. Again, see the Appendix for details.

3.2 (1+1)-D hard sphere model

The HS model with the virial coefficients (3.1.1) is examined, to confirm that the approximate solutions are accurate and also to examine any differences that occur between this series and the CS formulation, $Z = \frac{1+\eta+\eta^2-\eta^3}{(1-\eta)^3}$, as used by [81, 82], in their studies of colloidal solitary waves. In figure 3.1, we plot the electric field $|u|$ versus x for (1+1)-D

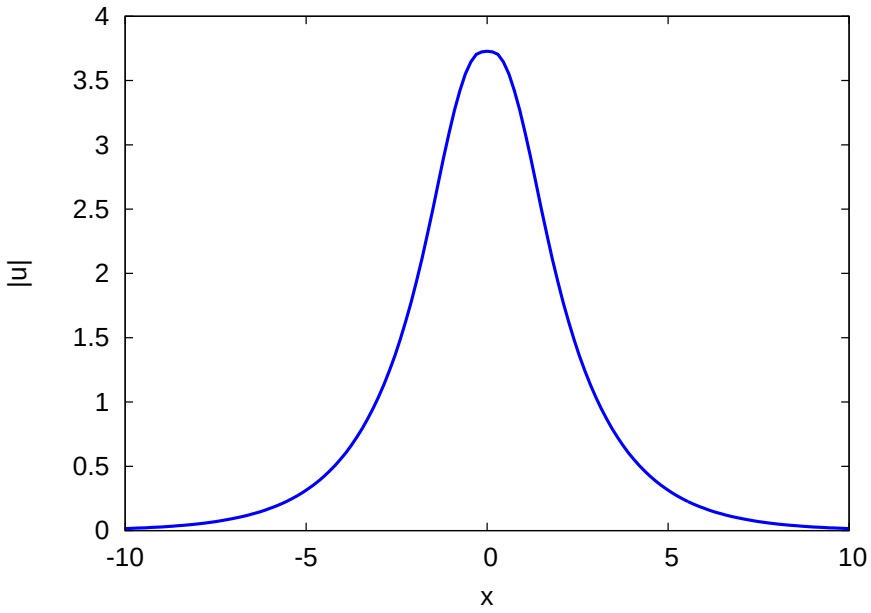

Figure 3.1: (color online) Soliton profile of (1+1)-D HS model. Shown is the electric field $|u|$ versus x for parameters $\eta_0 = 1 \times 10^{-3}$ and $P = 35$.

HS model, for the parameters $\eta_0 = 1 \times 10^{-3}$ and $P = 35$. This figure shows that the electric field has the form of a localized beam with a peak amplitude of $a = 3.727$.

Figure 3.2 shows the power versus propagation constant, P versus $\log \sigma$, curve for (1+1)-D HS colloidal solitary waves. The background packing fraction $\eta_0 = 1 \times 10^{-3}$. The same parameters as in Figure 1 of Marchant and Smyth [81] are used. Shown are the semi-analytical solutions (2.2.6) for the HS series and the CS model and the numerical solutions of (2.1.1) for the HS series. The figure shows the existence of two stable branches, separated by an unstable branch. On the low power branch broad solitary waves of small amplitude occur, while on the high power branch the solitary waves are narrower with higher amplitudes.

The semi-analytical HS series unstable branch exists for

$$\begin{aligned} -2.73 < \log \sigma < -1.25 \ \text{ and } \ 33.26 < P < 51.27, \\ 4.28 \times 10^{-3} < \alpha < 0.19 \ \text{ and } \ 1.31 < a < 2.28, \\ 3.31 < \beta < 6.62 \ \text{ and } \ 4.93 < w < 9.69. \end{aligned} \tag{3.2.4}$$

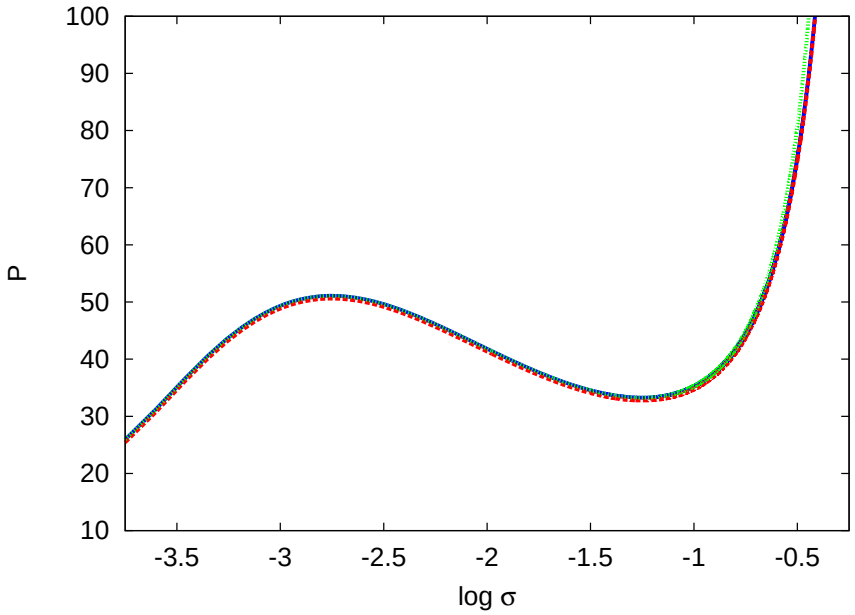

Figure 3.2: (color online) The power versus propagation constant, P versus $\log\sigma$, curve for (1+1)-D HS model. Shown are the semi-analytical solutions for the HS series (3.1.1) (solid blue line) and CS model (dotted green line) and the numerical HS series (dashed red line) solutions. The background fraction is $\eta_0 = 1 \times 10^{-3}$.

The limits of the unstable branch, and the properties of these marginally stable solitary waves are very close to the equivalents for CS solitary waves, with variations less than 1%, see (36) in Marchant and Smyth [81]. These limits and the figure indicate that the series (3.1.1) generates solitary wave solutions very similar to those found by the CS formula with both curves the same to graphical accuracy. An excellent comparison with numerical solutions is also found.

Figure 3.3 shows the power versus propagation constant, P versus $\log\sigma$, curve for (1+1)-D HS colloidal solitary waves with a different background packing fraction $\eta_0 = 1 \times 10^{-2}$. Shown are the semi-analytical solutions (2.2.6) for the HS series and the CS model and the numerical solutions of (2.1.1) for the HS series. Here we increase the background packing fraction value to show that bistability has vanished and only a single stable solutions branch exists. The larger value of background packing fraction has resulted in the loss of the multiple solution branches. Again the HS series, the CS formulations and numerical solutions are all very close. The results show that the HS series

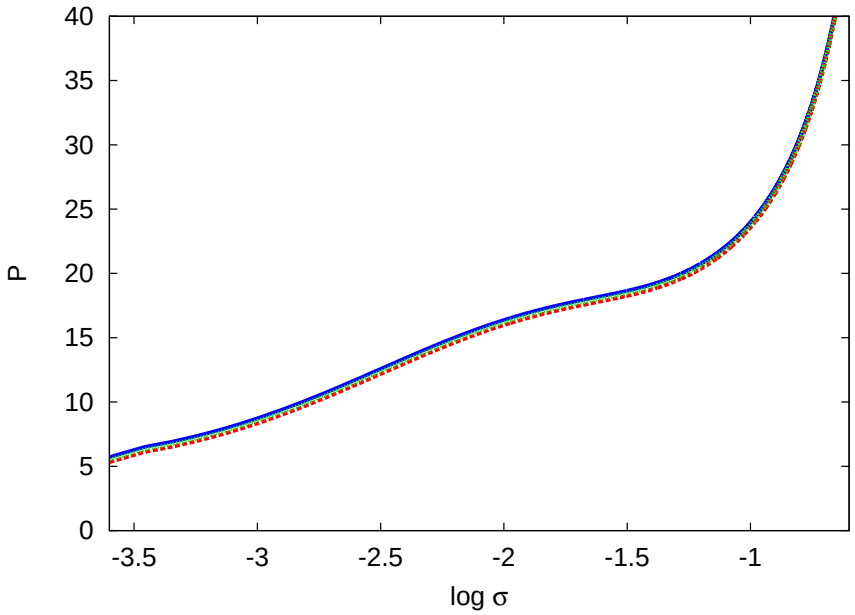

Figure 3.3: (color online) The power versus propagation constant, P versus $\log\sigma$, curve for (1+1)-D HS model. Shown are the semi-analytical solutions for the HS series (3.1.1) (solid blue line) and CS model (dotted green line) and the numerical HS series (dashed red line) solutions. The background fraction is $\eta_0 = 1 \times 10^{-2}$.

differ from the CS results, by less than 4%, over the presented range. This is due to the fact differences between the series (3.1.1) and the CS formula, occur for high amplitude solitary waves, which have high packing fractions.

Figure 3.4 shows the neutral stability curve in the propagation constant versus background packing fraction, η_0 versus $\log\sigma$, plane for the (1+1)-D HS colloidal solitary waves. Shown are the semi-analytical solutions (2.2.6) for the HS series and the CS model and the numerical solutions of (2.1.1) for the HS series. The region under the curves represents parameter values corresponding to the existence of the middle, unstable branch of solitary wave solutions. The region of parameter space in which unstable solutions occur is reduced and then eliminated as the background packing fraction increases. The parameters of the solitary wave with neutral stability at the turning point are $(\log\sigma, \eta_0) = (-1.66, 5.66 \times 10^{-3})$ for the semi-analytical HS series solution and $(\log\sigma, \eta_0) = (-1.66, 5.61 \times 10^{-3})$ for the numerical solution. This limiting parameter value is also very close to that found by Marchant and Smyth [81] for CS solitary waves,

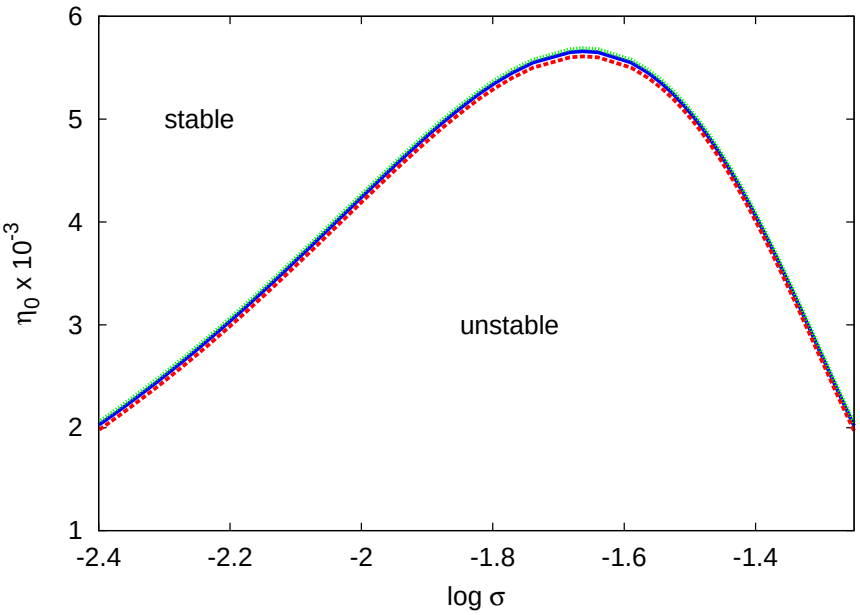

Figure 3.4: (color online) The neutral stability curve in the propagation constant-background packing fraction, $\log\sigma$ versus η_0, plane for the (1+1)-D HS models. Shown are the semi-analytical solutions for the HS series (3.1.1) (solid blue line) and the CS formula (dotted green line), and the numerical HS series (dashed red line) solutions.

$(\log\sigma, \eta_0) = (-1.67, 5.69 \times 10^{-3})$.

From these results, we can confirm that for (1+1)-D HS series, bistable behavior only occurs when background packing fraction, $\eta_0 \leq 5.66 \times 10^{-3}$ and a single stable branch exists for background packing fractions greater than this value. The two semi-analytical predictions and the numerical solutions are all very close to each other with less than a 1% difference.

3.3 (1+1)-D hard disk model

In this section, semi-analytical and numerical solutions for the HD model are presented. Most previous studies have used the CS compressibility formula even though it is based on the interactions between spherical particles. This is not appropriate for modelling (1+1)-D colloidal solitary waves, as they only involve the x and z spatial coordinates. In (1+1)-D scenarios the interaction model should be based on a 2-D geometry, which is consistent

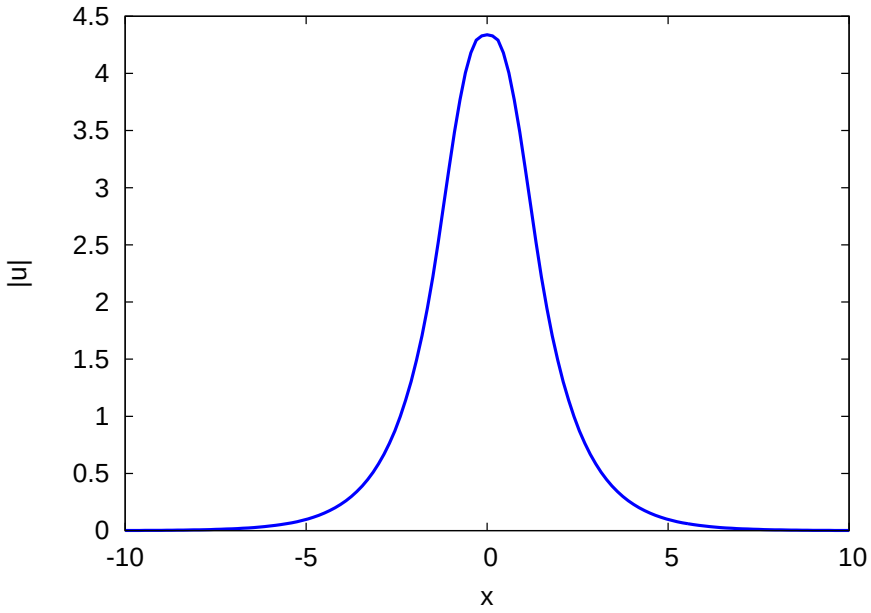

Figure 3.5: (color online) Soliton profile of (1+1)-D HD model. Shown is the electric field $|u|$ versus x for parameters $\eta_0 = 1 \times 10^{-2}$ and $P = 35$.

with the HD model. Here we find more physically realistic (1+1)-D HD colloidal solitary waves and compare the results with those obtained for the HS model. In figure 3.5, we plot the electric field $|u|$ versus x for (1+1)-D HD model, which is the example of soliton profile for the parameters $\eta_0 = 1 \times 10^{-2}$ and $P = 35$. This figure shows that the pulse has the form of a localized beam with a peak amplitude of $a = 4.219$.

Figure 3.6 shows the power versus propagation constant, P versus $\log \sigma$, curve for (1+1)-D HD solitary waves. The background packing fraction used is $\eta_0 = 1 \times 10^{-3}$. Shown are the the semi-analytical solutions (2.2.6) and numerical solutions of (2.1.1). Qualitatively the curve is similar to figure 3.2, for the HS model, with bistability occurring, but some quantitative differences occur between the two models. For the HD model the middle unstable branch exists for

$$\begin{aligned} &-2.76 < \log \sigma < -0.93 \ \text{ and } \ 23.8 < P < 50.3, \\ &4.47 \times 10^{-3} < \alpha < 0.42 \ \text{ and } \ 1.31 < a < 2.78, \\ &0.80 < \beta < 10.9 \ \text{ and } \ 1.54 < w < 14.6. \end{aligned} \tag{3.3.5}$$

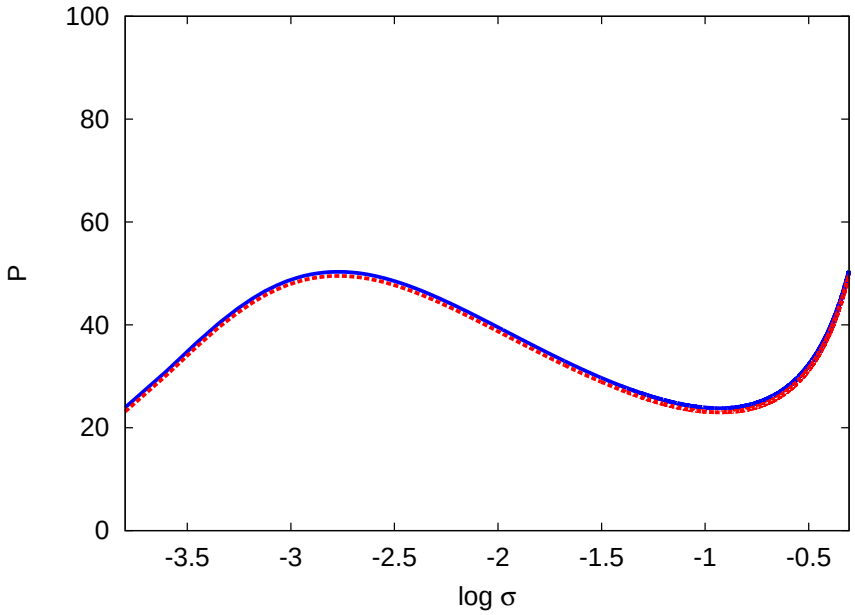

Figure 3.6: (color online) The power versus propagation constant, P versus $\log\sigma$, curve for the (1+1)-D HD model. Shown are the semi-analytical (solid blue line) and the numerical (dashed red line) solutions. The background fraction is $\eta_0 = 1 \times 10^{-3}$.

The end points of the unstable branch, for the HD and HS models, are very similar. If we compare the HS and HD solitary waves for $P = 50$ on the high power branch there are differences in parameter values of about 10% with the HD solitary wave a little steeper and narrower than the HS one. Figure 3.7 shows the power versus propagation constant, P versus $\log\sigma$, curve for (1+1)-D HD model for colloidal solitary waves. The background packing fraction, $\eta_0 = 1 \times 10^{-1}$. Shown are the the semi-analytical solutions (2.2.6) and numerical solutions of (2.1.1). Again this behaviour is qualitatively similar to the HS case but there are quantitative differences when $\log\sigma > -2$. If we compare the HS and HD solitary waves for $P = 10$ there are significant differences in the wave properties with the HD wave much steeper, by about 30%, and narrower, by about 40%, than the CS wave.

Figure 3.8 shows the neutral stability curve in the propagation constant versus background packing fraction, η_0 versus $\log\sigma$, plane for (1+1)-D HD colloidal solitary waves. Both semi-analytical and numerical solutions are shown. The parameters of the solitary waves at the turning point are $(\log\sigma, \eta_0) = (-1.35, 1.14 \times 10^{-2})$ for the semi-analytical solution, and $(\log\sigma, \eta_0) = (-1.35, 1.11 \times 10^{-2})$ for the numerical solution. Hence the

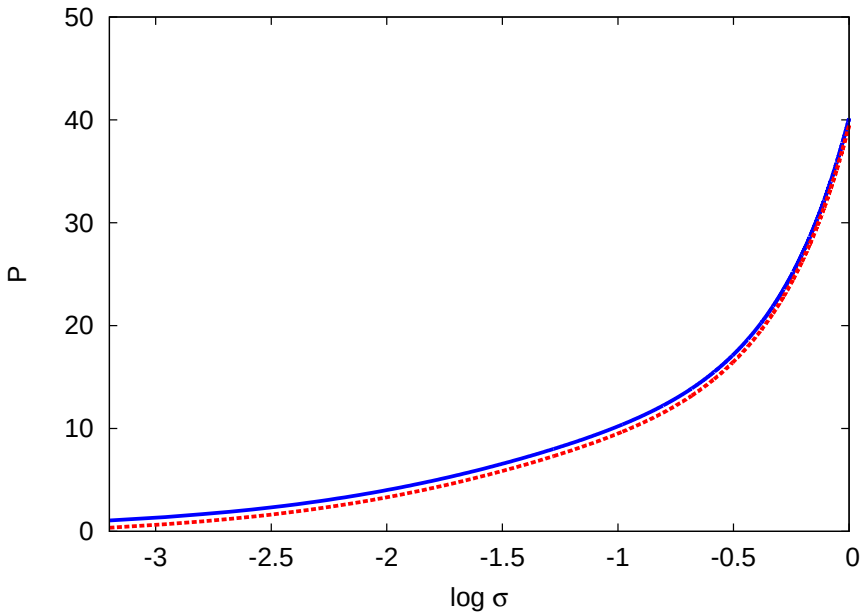

Figure 3.7: (color online) The power versus propagation constant, P versus $\log \sigma$, curve for the (1+1)-D HD model. Shown are the semi-analytical (solid blue line) and the numerical (dashed red line) solutions. The background fraction is $\eta_0 = 1 \times 10^{-1}$.

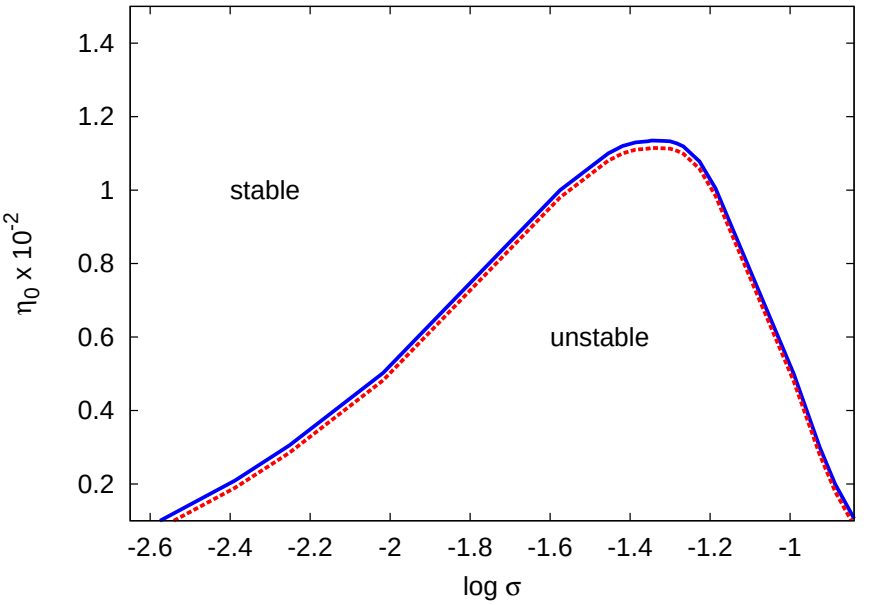

Figure 3.8: (color online) The neutral stability curve in the propagation constant-background packing fraction, $\log \sigma$ versus η_0, plane for the (1+1)-D HD model. Shown are the semi-analytical (solid blue line) and the numerical (dashed red line) solutions.

semi-analytical model predicts that bistable behaviour occurs for a much greater region of parameter space, compared with the HS model, for which $\eta_0 \leq 5.6 \times 10^{-3}$. Given the significant differences in these predictions of the HD and HS models, and that the HS model is not geometrically appropriate in this scenario, we believe that the HD model should be used instead of the HS model (or the related CS formula), when modelling (1+1)-D colloidal solitary waves.

3.4 (1+1)-D temperature dependent model

We now consider the (1+1)-D HD coefficients but now use a temperature dependent second coefficient given by (3.1.3) and $B_2 = 2 - \frac{100}{T}$. The choice of $\lambda = 0$ means that the second coefficient has an inverse temperature dependence. Therefore, in the limit as the temperature becomes large this model approaches the HD case, as $B_2 \to 2$. We are interested in exploring the changes in solitary wave properties due to temperature effects. The values of T are some scale of temperatures where any larger value of T will make B_2 approaches the HD case. Here we use $T = 10, 50$ and 100. In figure 3.9, we plot the electric field $|u|$ versus x for (1+1)-D temperature dependent model, which is the example of soliton profile for the parameters $\eta_0 = 1 \times 10^{-2}$ and $P = 35$. This figure shows that the electric field has the form of a localized beam with peak amplitudes of $a = 3.692$ for $T = 10$, $a = 3.752$ for $T = 50$ and $a = 3.789$ for $T = 100$. Hence increasing temperature causes the profile to narrow and the amplitude to increase.

Figure 3.10 shows the power versus propagation constant, P versus $\log \sigma$, curves for the (1+1)-D temperature dependent model. The background packing fraction $\eta_0 = 1.0 \times 10^{-3}$ and the temperature is $T = 10, 50$ and 100. Multiple solution branches occur for both $T = 50$ and 100, while for $T = 10$, a single stable branch occurs. The second virial coefficient $B_2 = 0$ at $T = 50$ so for temperatures larger than this the particle interactions are repulsive and for lower temperatures the interactions are attractive. Hence, as the

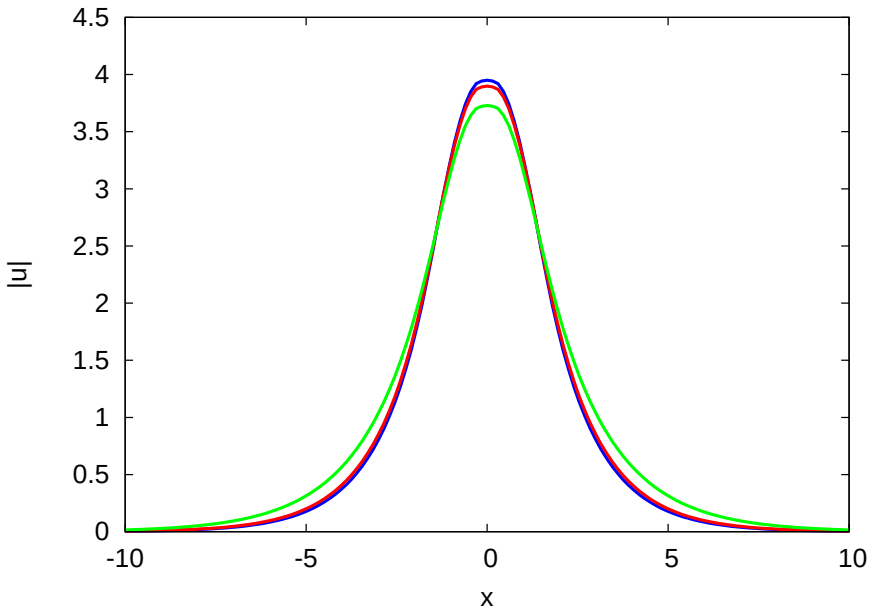

Figure 3.9: (color online) Soliton profile of (1+1)-D temperature dependent model. Shown is the electric field $|u|$ versus x results for $T = 10$ (top green line), $T = 50$ (middle red line) and $T = 100$ (bottom blue line). The parameters used are $\eta_0 = 1 \times 10^{-2}$ and $P = 35$.

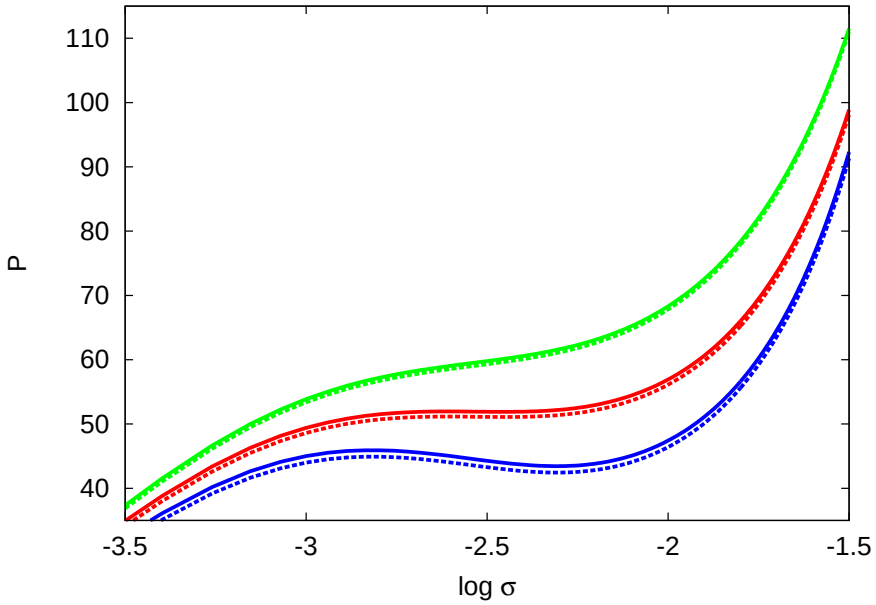

Figure 3.10: (color online) The power versus propagation constant, P versus $\log \sigma$, curve for the (1+1)-D temperature dependent model. The background fraction is $\eta_0 = 1 \times 10^{-3}$. Shown are the semi-analytical (solid lines) and numerical (dashed lines) results for $T = 10$ (top green lines), $T = 50$ (middle red lines) and $T = 100$ (bottom blue lines).

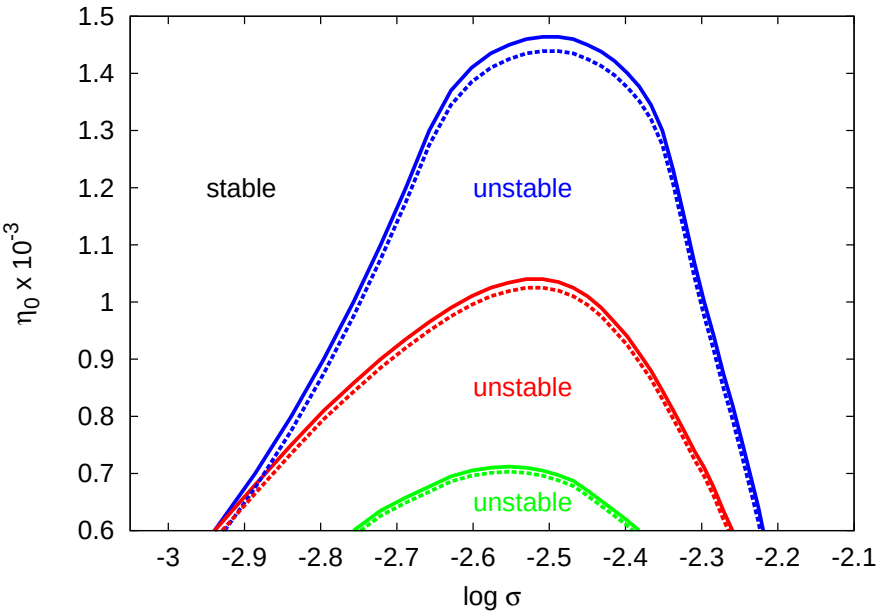

Figure 3.11: (color online) The neutral stability curve in the propagation constant-background packing fraction plane $(\log\sigma, \eta_0)$ for the (1+1)-D temperature dependent model. Shown are the semi-analytical (solid lines) and numerical (dashed lines) for $T = 10$ (bottom green lines), $T = 50$ (middle red lines) and $T = 100$ (top blue lines).

nature of the particle interactions change from repulsive to attractive the bistable nature of the solution disappears. For colloidal solitary waves of the same power, $P = 60$, the solitary waves are much steeper and narrower as the temperature increases as the particle interactions become more repulsive.

Figure 3.11 shows the neutral stability curve in the propagation constant versus background packing fraction, η_0 versus $\log\sigma$, plane for the (1+1)-D temperature dependent model. Both the semi-analytical and numerical solutions are shown. At $T = 100$ bistable behavior occurs for the (1+1)-D geometry for $\eta_0 \leq 1.47 \times 10^{-3}$, and single stable solution branch exists for background packing fractions greater than this value. For $T = 10$ and $T = 50$ the bistable behavior is possible for $\eta_0 \leq 7.12 \times 10^{-4}$ and $\eta_0 \leq 1.04 \times 10^{-3}$, respectively. As the temperature goes up, the region of parameter space, in which bistability occurs, also increases.

Figure 3.12 shows the maximum background packing fraction, for which bistability occurs, versus temperature. Shown are semi-analytical and numerical solutions for

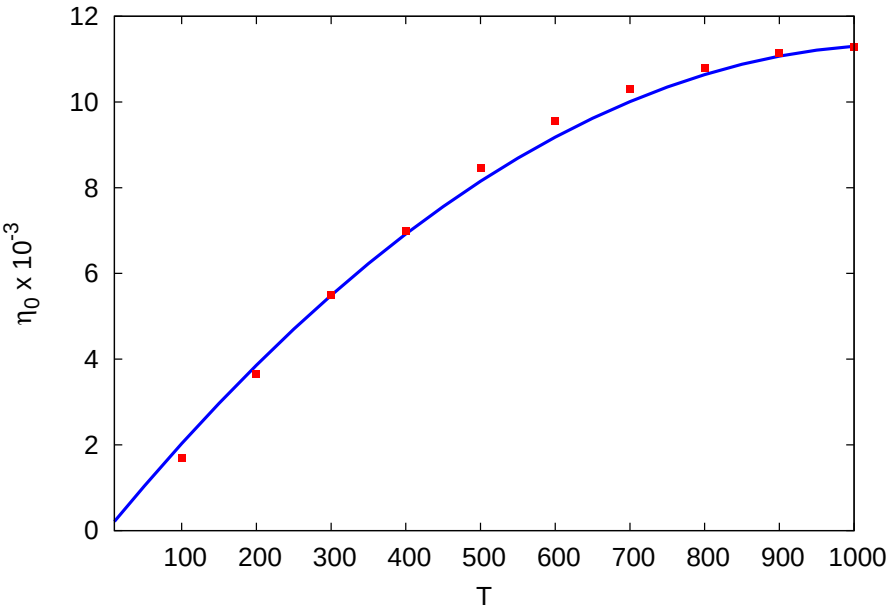

Figure 3.12: (color online) The maximum background packing fraction, for which bistability occurs, versus temperature. Shown are the semi-analytical (solid blue line) solutions and numerical solutions (red squares) for the (1+1)-D temperature dependent model.

the (1+1)-D temperature dependent model. As the temperature increases, the maximum background packing fraction, for which bistability is possible, increases. At $T = 1000$ the maximum packing fraction is $\eta_0 = 1.12 \times 10^{-3}$, which is very close to the HD limit of $\eta_0 = 1.14 \times 10^{-3}$. The differences between the semi-analytical and numerical solutions are less than 5%. From these solutions, it is shown that (1+1)-D colloids with temperature dependent compressibility will approach the results obtained from (1+1)-D HD model for $T \approx 1000$. At lower values of temperature there is a significant drop in the maximum background packing fraction, for which bistability occurs.

3.5 (2+1)-D hard sphere model

We have previously mentioned that the HS model is appropriate to describe the (2+1)-D geometry, thus for this research, we employ the HS compressibility formula (3.1.1) to model (2+1)-D semi-analytical HS colloidal solitary wave solutions. In order to verify the results obtain in this research, we also examine any differences that occur with the CS

formulation as used by Marchant and Smyth [81] and see how close the solutions are to the HS model developed here. In figure 3.13, we plot the electric field $|u|$ versus x for (2+1)-D HS model, for the parameters $\eta_0 = 1 \times 10^{-2}$ and $P = 35$. This figure shows that the electric field has the form of a localized beam with a peak amplitude of $a = 4.11$.

Figure 3.14 shows the power versus propagation constant, P versus $\log \sigma$, curves for (2+1)-D HS colloidal solitary waves. The background packing fraction $\eta_0 = 1 \times 10^{-3}$. Shown are the semi-analytical solutions (2.3.10) for the HS series and the CS model and the numerical solutions of (2.1.1) for the HS series. This figure indicates the existence of two solution branches, one stable and one unstable. This is qualitatively different to the (1+1)-D case where bistable behavior occurs. The (2+1)-D colloidal solitary waves are unstable at small σ (large negative values of $\log \sigma$) because no stable small σ, low power, solutions exists. This is related to the fact that (2+1)-D NLS solitons are unstable, see, for example, [104]. When the power decreases the intensity $|u|$ and packing fraction η of the colloidal solitary waves decrease and the governing equation (2.1.1) approaches the Kerr limit, resulting in instability for low power (2+1)-D colloidal solitary waves. (1+1)-D colloidal solitary waves also become Kerr-like for small σ and low powers but (1+1)-D NLS solitons are stable, hence the occurrence of a low amplitude stable branch for (1+1)-D colloidal solitary waves.

Comparing the semi-analytical and numerical solutions for the HS series at $\log \sigma = -1.25$ (the smallest value of $\log \sigma$ for which the numerical solution is stable) there is a 7% difference in the power. The semi-analytical solution predicts that the stable branch occurs for

$$\log \sigma > -1.21, \quad \alpha > 0.48, \quad a > 3.83. \tag{3.5.6}$$

Comparing the semi-analytical HS series and CS solutions, we find less than a 1% difference over the range of the figure.

Figure 3.15 shows the power versus propagation constant, P versus $\log \sigma$, curve for (2+1)-D HS colloidal solitary waves. The background packing fraction $\eta_0 = 1.5 \times 10^{-1}$.

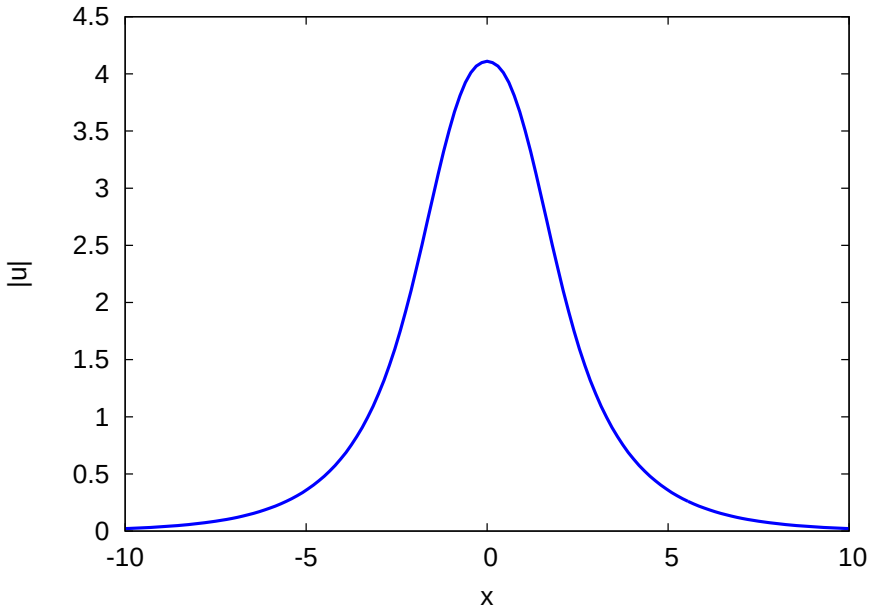

Figure 3.13: (color online) Soliton profile of (2+1)-D HS model. Shown is the electric field $|u|$ versus x for parameters $\eta_0 = 1 \times 10^{-2}$ and $P = 35$.

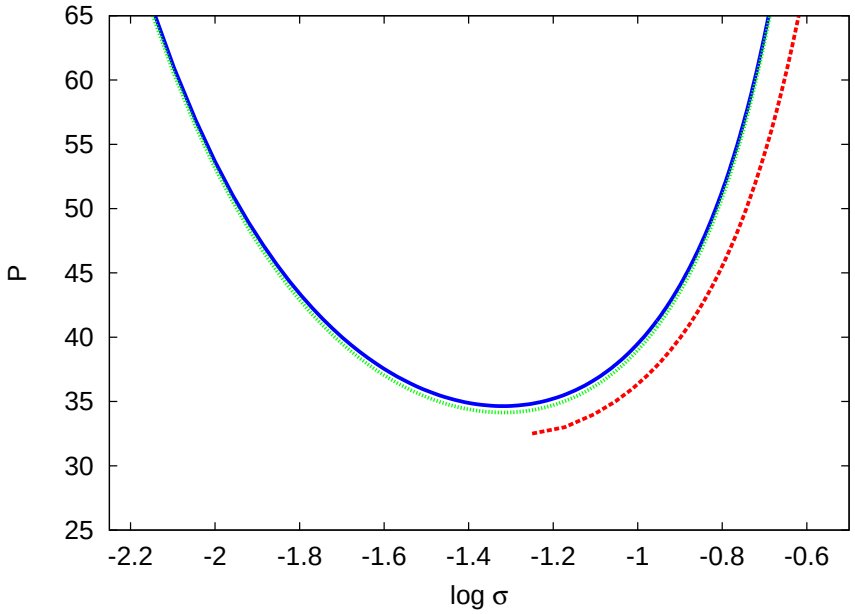

Figure 3.14: (color online) The power versus propagation constant, P versus $\log \sigma$, curve for (2+1)-D HS models. Shown are the semi-analytical solutions for the HS series (3.1.1) (solid blue line) and CS model (dotted green line) and the numerical HS series (dashed red line) solutions. The background fraction is $\eta_0 = 1 \times 10^{-3}$.

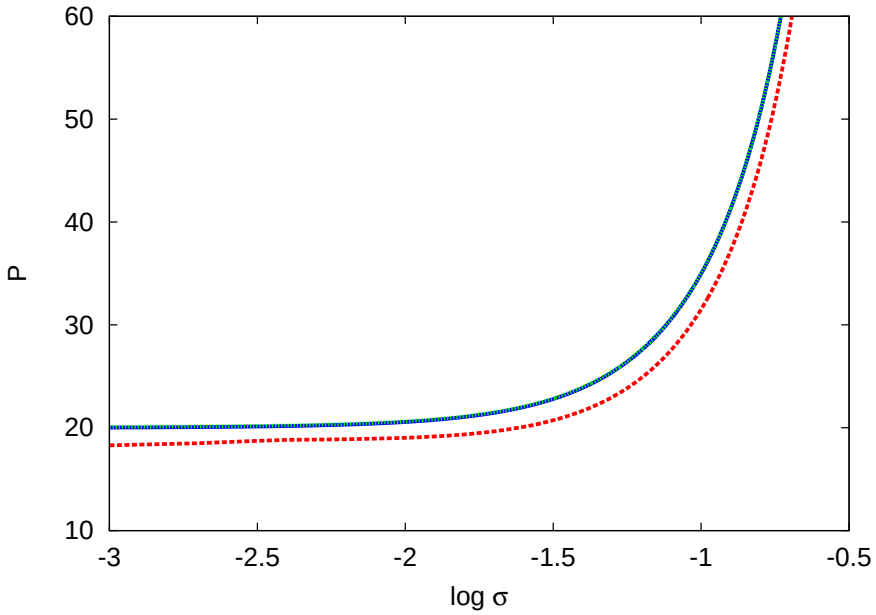

Figure 3.15: (color online) The power versus propagation constant, P versus $\log\sigma$, curve for (2+1)-D HS models. Shown are the semi-analytical solutions for the HS series (3.1.1) (solid blue line) and CS model (dotted green line) and the numerical HS series (dashed red line) solutions. The background fraction is $\eta_0 = 1.5 \times 10^{-1}$.

Shown are the semi-analytical solutions (2.3.10) for the HS series and the CS model and the numerical solutions of (2.1.1) for the HS series. In this case there is a single stable solution branch and the comparison between the semi-analytical and numerical solutions is good, with no more than a 10% error. There is also an excellent comparison between the HS series and CS semi-analytical solutions, with the solutions the same to graphical accuracy.

Figure 3.16 shows the neutral stability curve in the propagation constant versus background packing fraction, η_0 versus $\log\sigma$, plane for the (2+1)-D HS colloidal solitary waves. Shown are the semi-analytical solutions (2.3.10) for the HS series and the CS models and the numerical solutions of (2.1.1) for the HS series. Multiple solitary wave solution branches occur for parameter values below the curves. The maximum background packing fraction, for which multiple semi-analytical HS series solution branches occur, is $\eta_0 \leq 0.124$. This is very close to the numerical estimate of $\eta_0 \leq 0.126$. For the CS case multiple solution branches occur for $\eta_0 \leq 0.125$, so the CS and HS series (3.1.1)

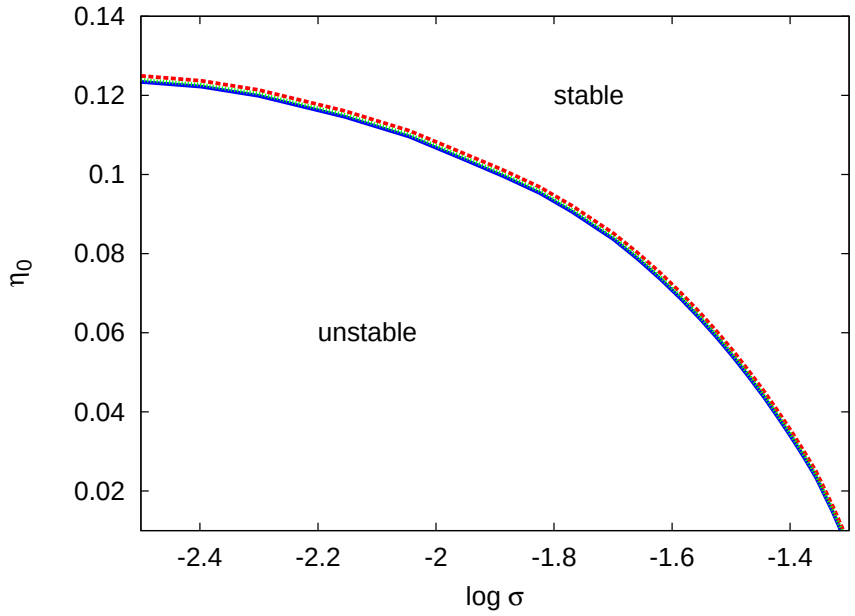

Figure 3.16: (color online) The neutral stability curve in the propagation constant-background packing fraction, $\log \sigma$ versus η_0, plane for the (2+1)-D HS models. Shown are the semi-analytical solutions for the HS series (3.1.1) (solid blue line) and the CS formula (dotted green line), and the numerical HS series (dashed red line) solutions.

predictions are very close in this case with a 1% error. Therefore, from these results, it is appropriate to say that the HS series describes the (2+1)-D colloidal solitary wave with a very high accuracy, compared to the results of Marchant and Smyth in [81], for the CS formulation.

3.6 (2+1)-D temperature dependent model

This section discusses the (2+1)-D colloids with a temperature dependent compressibility. Here we consider the HS virial coefficients but with a temperature dependent second coefficient given by (3.1.3) and $B_2 = 4 - \frac{100}{T}$. Similar to the discussion for the (1+1)-D problem, where the second virial coefficient approaches the HD model when temperature increases, here, for the (2+1)-D solitary wave, we know that as the temperature becomes large, the second virial coefficient $B_2 \to 4$, and the HS model is approached. In figure 3.17, we plot the electric field $|u|$ versus x for (2+1)-D temperature dependent model, for

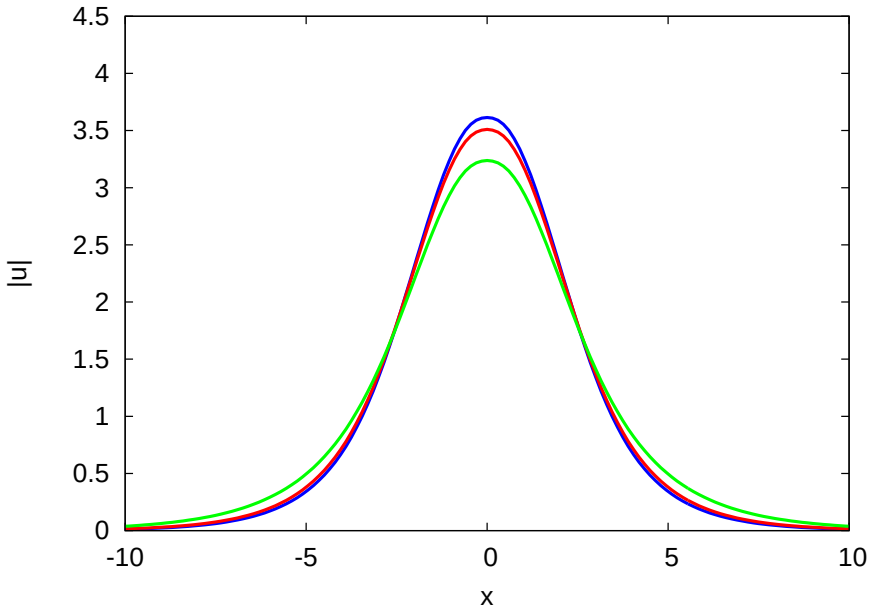

Figure 3.17: (color online) Soliton profile of (2+1)-D temperature dependent model. Shown is the electric field $|u|$ versus x for parameters $\eta_0 = 1.3 \times 10^{-1}$ and $P = 35$ for $T = 25$ (top blue line), $T = 50$ (middle red line) and $T = 100$ (bottom green line).

the parameters $\eta_0 = 1.3 \times 10^{-1}$ and $P = 35$. This figure shows that the electric field has the form of a localized beam with the peak amplitudes of $a = 3.614$ for $T = 25$, $a = 3.51$ for $T = 50$ and $a = 3.238$ for $T = 100$. Hence the soliton profile decreases and broadens, as the temperature increases.

Figure 3.18 shows the power versus propagation constant, P versus $\log \sigma$, curve. The background packing fraction $\eta_0 = 1.3 \times 10^{-1}$. Shown are the semi-analytical and numerical results for $T = 25$, 50 and 100. The two curves corresponding to lower temperatures have multiple solution branches while the curve for the highest temperature has a single stable solution branch. The second virial coefficient $B_2 = 0$ at $T = 25$ so solution multiplicity occurs in a larger region of parameter space, as the temperature decreases and the particle interactions become less repulsive, or attractive, in nature. The $T = 50$ curve is very close to the transition between a single solution branch and multiple solution branches. The results from figure 3.19 show that, for $T = 50$, multiple solution branches occur for $\eta_0 \leq 1.35 \times 10^{-1}$. The comparison between the numerical and semi-analytical solutions is excellent with less than a 5% error. For colloidal solitary waves of the same

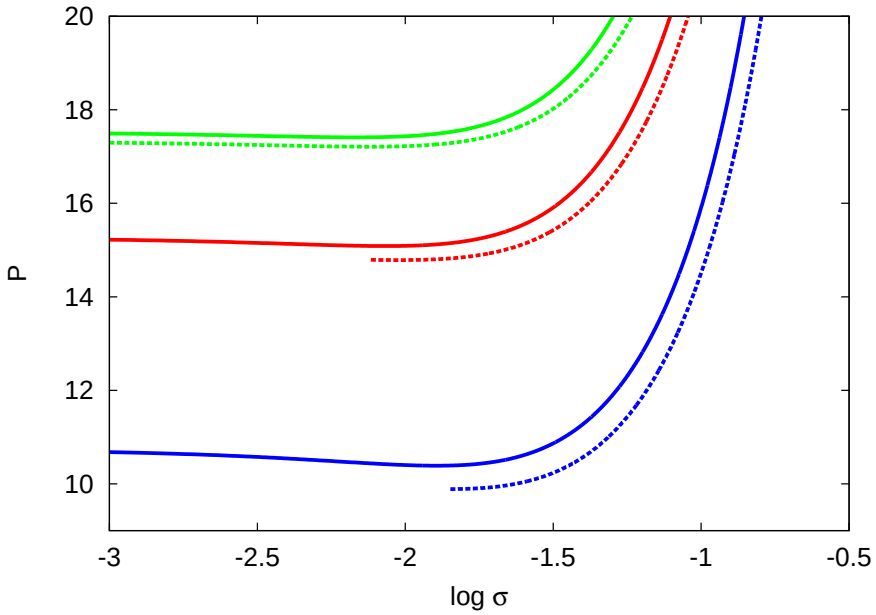

Figure 3.18: (color online) The power versus propagation constant, P versus $\log \sigma$, curve for the (2+1)-D temperature dependent model. The background fraction is $\eta_0 = 1.3 \times 10^{-1}$. Shown are the semi-analytical (solid lines) and numerical (dashed lines) results for $T = 25$ (bottom blue lines), $T = 50$ (middle red lines) and $T = 100$ (top green lines).

power, $P = 20$, the solitary waves are much steeper and narrower as the temperature decreases and as the particle interactions become more attractive.

Figure 3.19 shows neutral stability curves in the propagation constant versus background packing fraction, η_0 versus $\log \sigma$, plane for the (2+1)-D temperature dependent model. Shown are the semi-analytical and numerical results for $T = 25$, 50 and 100. At $T = 25$ multiple solution branches occurs for background packing fraction $\eta_0 \leq 1.44 \times 10^{-1}$, while at higher temperatures $T = 50$ and $T = 100$, the limits for multiple solutions are $\eta_0 \leq 1.35 \times 10^{-1}$, and $\eta_0 \leq 1.27 \times 10^{-1}$, respectively. As the temperature increases, and the repulsion between the particles increases, the parameter region in which multiple solution branches occur, decreases. The comparison between the numerical and semi-analytical solutions is excellent with less than a 1% error.

Figure 3.20 shows the maximum background packing fraction, for which multiple solutions occur, versus temperature. Shown are the semi-analytical and numerical solutions for the (2+1)-D temperature dependent model. We see that as the temperature increases,

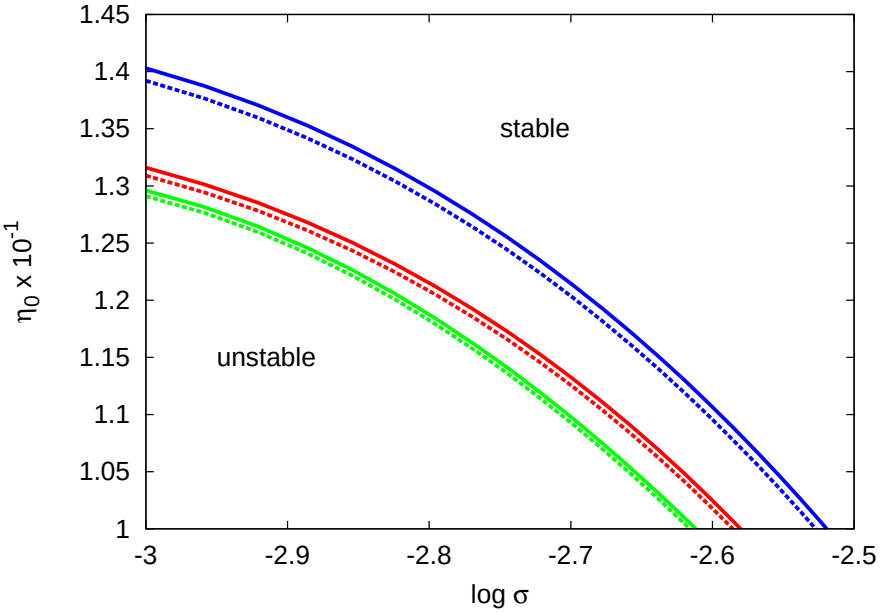

Figure 3.19: (color online) The neutral stability curve in the propagation constant-background packing fraction plane, $(\log \sigma, \eta_0)$ for the (2+1)-D temperature dependent model. Shown are the semi-analytical (solid lines) and numerical (dashed lines) for $T = 25$ (top blue lines), $T = 50$ (middle red lines) and $T = 100$ (bottom green lines).

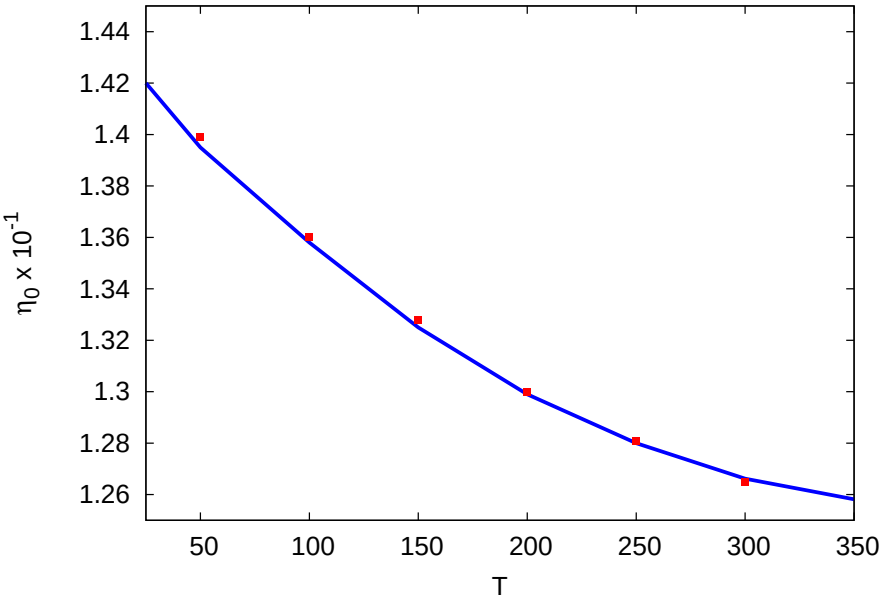

Figure 3.20: (color online) The maximum background packing fraction, for which multiple solution branches occur, versus temperature. Shown are the semi-analytical (solid blue line) and numerical (red square-point) solutions for the (2+1)-D temperature dependent model.

the maximum background packing fraction, for which multiple solution branches occur, decreases. At $T = 350$ the maximum packing fraction is $\eta_0 = 1.26 \times 10^{-1}$, which is close to the HS limit. The differences between the semi-analytical and numerical solutions are less than 4%.

3.7 Summary

This chapter thoroughly examines semi-analytical solutions for colloidal solitary waves in the (1+1)-D and (2+1)-D geometries. These solutions are described using a series for the non-ideal gas law with hard sphere, hard disk and temperature dependent models are considered. It is shown that, for low to medium packing fractions, the hard sphere formulation is close to the CS approximations, with some differences occurring at large packing fractions. The hard sphere model and its related CS approximation are commonly used to model (1+1)-D colloidal waves, however the interactions between spherical particles is not physically appropriate in this two-dimensional geometry. The (1+1)-D results shown that significant differences occur between the hard disk and hard sphere predictions which indicates that the hard disk model, or some other interaction model consistent with a two-dimensional geometry should be used instead.

From the results obtained in this chapter, we found that there is a systematic and more-or less-uniform estimation between the the semi-analytical and the numerical solutions. We believe this happens because the choice of the trial function chosen for the (1+1)-D and (2+1)-D models does not exactly match the solitary waves profiles.

The results of this chapter show that the stability of (2+1)-D colloidal solitary waves is temperature dependent, with the region of parameter space, in which multiple solution branches occurs, decreasing as the temperature increases. For the (1+1)-D temperature dependent model the opposite effect occurs, with as the region of parameter space increasing as the temperature increases (see figure 3.12). Here, the effect of varying the

coefficients in the temperature dependent second virial coefficient (3.1.3) have been fully explored; for all positive choices of a and b the qualitative trends, seen in figure 3.12, for (1+1)-D colloidal solitary waves, and in figure 3.20, for (2+1)-D colloidal solitary waves, are the same.

The temperature dependent models allow the effects of temperature dependency, on the particle interactions, to be explored. The results show that the regions of parameter space in which multiple solution branches occur vary significantly with temperature. For the (1+1)-D geometry increasing the temperature increases the parameter region in which multiple solutions occur, while for the (2+1)-D geometry the opposite effect occurs, with the parameter region shrinking as the temperature increases. This indicates the importance of geometrical effects on colloidal solitary wave properties and the need to use an appropriate particle interaction model.

Chapter 4

Dispersive shock waves in colloidal media

4.1 Introduction

This chapter considers the evolution of dispersive shock waves (DSW) in focusing colloidal media. We use the solitary wave solutions developed in Chapter 3, together with conservation laws to obtain semi-analytical expressions for the amplitude of the solitary waves generated in the DSW. This chapter which appears in Azmi and Marchant [105] forms a natural extension to the semi-analytical solutions for colloidal solitary waves, presented in Chapter 3. The (1+1)-D HS and HD models together with the temperature dependent results are used to understand the colloidal DSW, such as its behaviour for different background packing fractions and the bifurcation patterns that develop. A semi-analytical solution is also developed for the (2+1)-D circular DSW for the HS and the temperature dependent models, for the case in which the radius of the DSW is large. We obtain different bifurcation patterns which are compared with the numerical solutions for the (1+1)-D line DSW and also show that our theoretical estimates for the (2+1)-D DSW are very accurate.

4.2 Uniform soliton theory

In this section, we investigate the development of a DSW for the focusing colloidal equation (2.1.1) by looking at an IVP with the jump initial condition

$$u = \begin{cases} a_m e^{ikx}, & x < 0, \\ 0, & x > 0, \end{cases} \qquad \eta = \begin{cases} \eta_m, & x < 0, \\ \eta_0, & x > 0, \end{cases} \tag{4.2.1}$$

where a_m is the amplitude of the jump in electric field and k is the wavenumber of the continuous wave. The first of (4.2.1) is the jump in the electric field amplitude $|u|$ and there also exists a corresponding jump in the packing fraction, as in the second of (4.2.1). The correlation between these two jumps is linked by the state equation, ${a_m}^2 = g(\eta_m) - g_0$. In $x < 0$, the initial condition is always a continuous wave and there is nothing in $x > 0$.

We assume that the DSW generates a train of solitary waves of uniform amplitude, given by (2.1.1). In [44], this assumption was used by Assanto et. al for the related problem of shock resolution for the NLS-type equations governing nematic liquid crystals and led to accurate results. Their focusing equations are subject to MI, but the approximate method gives accurate predictions for the bore which develops at short propagation distances before the onset of MI. Marchant and Smyth [45] presented an approximate method for calculating the amplitude of the lead solitary waves of a DSW for general nonlinear wave equations. Their approximation is good when the DSW develops because as the bore evolves, it is dominated by the solitary waves. From here, they use conservation equations for the governing equations to determine the amplitude of these solitary waves. They also checked the validity of the approximate method by comparing its predictions with the known DSW solutions of the KdV equation, the Benjamin-Ono equation, the modified KdV equation and NLS equation. Their approximate theory gives a very good approximation for the amplitude of the solitary wave at the leading edge of the bore.

The mass conservation equation of (2.1.1) is

$$i\frac{\partial}{\partial z}|u|^2 + \frac{1}{2}\frac{\partial}{\partial x}(u^* u_x - u u_x{}^*) = 0. \tag{4.2.2}$$

The energy conservation equation for the colloid equations (2.1.1) is obtained by applying N$\ddot{o}$rther's Theorem to the Lagrangian (2.1.3). This energy equation is given by

$$\begin{aligned} &i\frac{\partial}{\partial z}[|u_x|^2 - 2(\eta-\eta_0)|u|^2 + 2\eta\ln\eta + 2\eta_0\ln\eta_0 - 2(\eta-\eta_0)(1+g_0) \\ &+6\eta + 2B_2\eta^2 + B_3\eta^3 - 6\eta_0 - 2B_2\eta_0^2 - B_3\eta_0^3 + \cdots] \\ &+\frac{1}{2}\frac{\partial}{\partial x}[u_x{}^* u_{xx} - u_x u_{xx}^* - 2(\eta-\eta_0)(u^* u_x - u u_x{}^*)] = 0. \end{aligned} \tag{4.2.3}$$

Next, we integrate the conservation laws from $x = -\infty$ to $x = \infty$. As the boundary condition at $x = -\infty$ is non-zero, as described by (4.2.1), the x derivative terms are non-zero at $x = -\infty$. Integrating the conservation equations then gives

$$\begin{aligned} &\frac{d}{dz} < M >= k a_m{}^2, \quad \frac{d}{dz} < H >= k a_m{}^2[k^2 - 2(\eta_m - \eta_0)], \quad \text{where} \\ &M = |u|^2, \quad H = [|u_x|^2 - 2(\eta-\eta_0)|u|^2 + 2\eta\ln\eta + 2\eta_0\ln\eta_0 \\ &-2(\eta-\eta_0)(1+g_0) + 6\eta + 2B_2\eta^2 + B_3\eta^3 - 6\eta_0 - 2B_2\eta_0^2 \\ &-B_3\eta_0^3 + \cdots], \quad < . >= \int_{-\infty}^{\infty} . \ \mathrm{d}x. \end{aligned} \tag{4.2.4}$$

Note that the total mass and energy of the system is unbounded but growth rates are bounded, and described by (4.2.4). We see that the conservation laws depend on k, which is the wavenumber of the initial condition. However, evolution of the DSW does not depend on k, so the ratio of the two equations in (4.2.4) in the limit of $k \to 0$ gives

$$\frac{d < H >}{d < M >} = -2(\eta_m - \eta_0). \tag{4.2.5}$$

Equation (4.2.5) is the condition that describes, for small wavenumber, the mass to energy ratio generated by the initial condition. We assume that solitary waves generated by the

DSW have this same mass to energy ratio. However, for NLS-type equations, the solitary waves amplitude is independent of wavenumber, so (4.2.5) applies for all wavenumber, see Assanto *et al* [44]. We now use the semi-analytical expression for a single colloidal solitary wave (2.2.4) which gives

$$\begin{aligned} &< M >= 2a^2 w, \;\; < H >= P, \;\; \text{where} \\ &P = \frac{2}{3}\frac{a^2}{w} - 4\alpha a^2 \Omega_1 - 4\alpha\beta(1+g_0) + 4\beta\Theta_1 + 8B_2\alpha\beta\eta_0 + \frac{8}{3}B_2\alpha^2\beta \\ &+6B_3{\eta_0}^2\alpha\beta + 4B_3\eta_0\alpha^2\beta + \frac{16}{15}B_3\alpha^3\beta + 2(\eta_m - \eta_0)(2a^2 w). \end{aligned} \tag{4.2.6}$$

Substituting (4.2.6) into (4.2.5) and integrating then gives the transcendental equation

$$\begin{aligned} &\frac{2}{3}\frac{a^2}{w} - 4\alpha a^2 \Omega_1 - 4\alpha\beta(1+g_0) + 4\beta\Theta_1 + 8B_2\alpha\beta\eta_0 + \frac{8}{3}B_2\alpha^2\beta \\ &+6B_3{\eta_0}^2\alpha\beta + 4B_3\eta_0\alpha^2\beta + \frac{16}{15}B_3\alpha^3\beta + 4a^2 w(\eta_m - \eta_0) = 0. \end{aligned} \tag{4.2.7}$$

From equation (4.2.7), together with the transcendental equations (2.2.6) for (1+1)-D solitary waves, we then obtain the amplitude a and α together with the width w and β of the electric field and packing fraction solitary waves in the DSW. These solitary wave properties are given in terms of the initial jump a_m. We can implicitly find the jump in the electric field amplitude a_m by finding the value of η_m, which is the jump in the packing fraction density. It is important to note that the wavenumber can be non-zero because the waves can move to the right in the speed of $V = k$, but the value of the wavenumber does not effect the amplitude or number of the waves in the dispersive shock wave.

The uniform soliton theory developed here will be used to obtain bifurcation patterns (a versus a_m graphs) which occur for the HS and HD models as well as the temperature dependent model. We also consider the evolution for the DSW at different background packing fraction values and examine how changes in temperature affect the DSW.

We must take note that the development of a DSW in a colloidal medium is subject to modulational instability (MI) and does not persist at long length scales. MI is a

well-known phenomenon that destabilizes wave propagation in dispersive media. It signifies the exponential growth of a small perturbation of the plane-wave amplitude during propagation. However the DSW can develop at a length scale shorter than for which MI dominates, hence experimentally can occur.

In the following sections, we will compare the numerical solutions of the colloidal equations (2.1.1) with the semi-analytical solutions developed for line (1+1)-D and circular (2+1)-D DSWs for HS, HD and temperature dependent models. The numerical solutions were found using a hybrid Runge-Kutta finite-difference scheme. A fourth-order Runge-Kutta scheme was used for the evolution in the propagation direction z (the time-like coordinate) and central finite-differences were used in the spatial domain x.

4.3 The (1+1)-D line DSW

For (1+1)-D colloids, the HD model is geometrically appropriate but the HS model has been widely used in previous studies. So, both the HS and HD models are examined here, to see what differences occur, together with the temperature dependent model.

Figure 4.1 shows the dispersive shock height, a_m at the bifurcation point versus the background packing fraction η_0 as described by (2.2.6), (4.2.7) and $\frac{da_m}{da} = 0$ for the (a) HS and (b) HD models. The uniform soliton theory is presented. If a solitary wave amplitude a versus shock height a_m diagram is considered, then $\frac{da_m}{da} = 0$ is the condition for a bifurcation point to occur in this diagram. The figure shows that for any value of $\eta_0 > 5.65\times10^{-3}$ for the HS model and $\eta_0 > 10.5\times10^{-3}$ for the HD model, no bifurcation point exists. This indicates that a single, stable, a versus a_m solution branch will occur beyond these values of η_0. Referring to [81, 82], they are the parameter values that separate the bi-stable and mono-stable regimes for the solitary wave solution for the (1+1)-D colloids. We also get two other types of a versus shock height a_m diagrams. The first type occurs for $3.96\times10^{-3} < \eta_0 < 5.65\times10^{-3}$ for the HS model and $7.4\times10^{-3} < \eta_0 < 10.5\times10^{-3}$

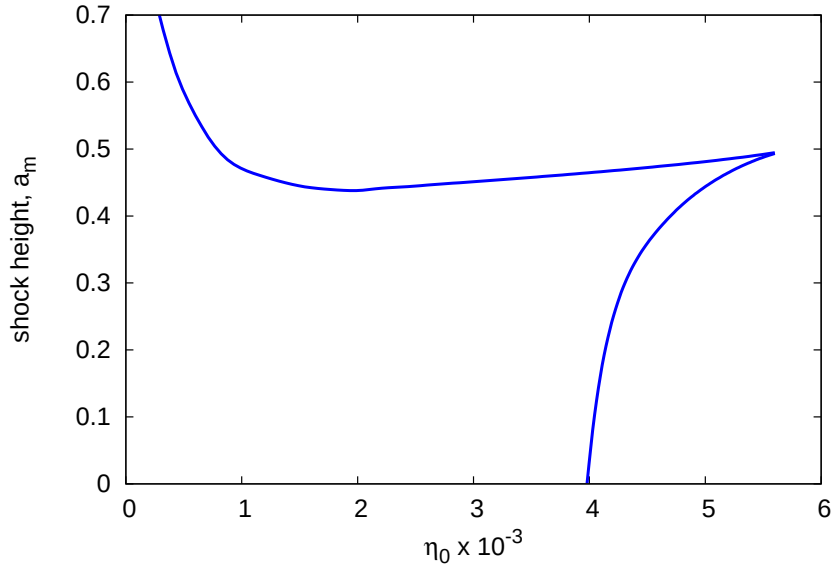

(a)

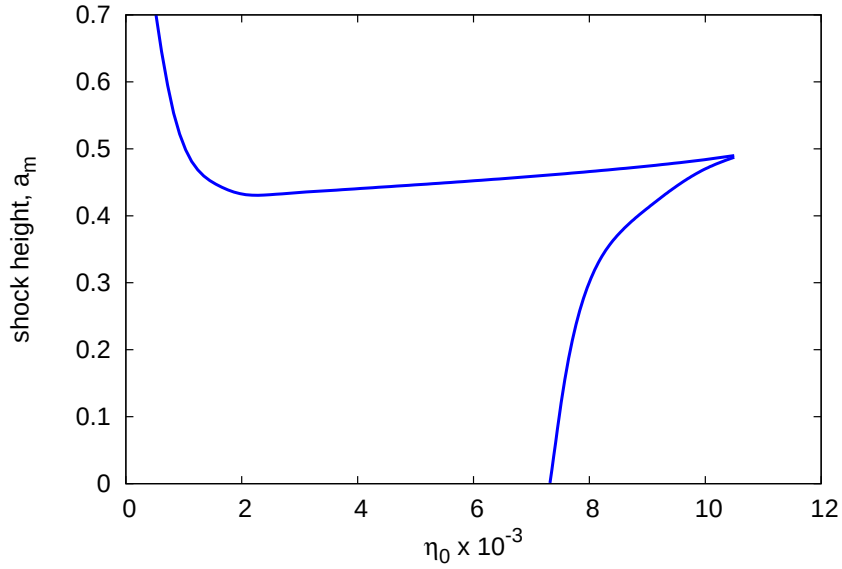

(b)

Figure 4.1: The dispersive shock height, a_m, at the bifurcation point, versus the background packing fraction η_0 for (a) HS and (b) HD models.

for the HD model, where S-shaped response curves are obtained. This kind of S-shaped response curve is similar to the multiple steady-state response curve seen in combustion theory for reaction-diffusion systems with an Arrhenius law, see Arrhenius [106]. In combustion theory, an S-shaped response curve is considered a classical result; it has two turning points along the bifurcation curve. If the solution jumps from the low temperature to the high temperature branch, this will cause a thermal runaway [107, 108]. However it is very unusual to observe this behaviour in optical solitary wave applications.

For $\eta_0 < 3.96 \times 10^{-3}$ in the HS model and $\eta_0 < 7.4 \times 10^{-3}$ in the HD model, we get the three solution branches, but now, the upper branch in the a versus shock height a_m diagram is separated from the lower two branches. It can be seen that the results obtained for the HD and HS models, while qualitatively similar, they vary significantly in the quantitative details. This indicates that the series (3.1.2) generates DSW which are quite different to those found by the series (3.1.1), as shown by the differences in the shock height-solitary wave amplitude response diagrams. For the geometrically appropriate HD model, S-shaped response curves occurs at much larger values of background packing fraction η_0 than for the HS model.

Figure 4.2 shows the solitary wave parameters a and α (amplitudes) with w and β (widths) of the uniform solitary waves in the DSW versus η_0. Shown is the uniform soliton theory given by (2.2.6) and (4.2.7). The shock height $a_m = 0.5$, for both the HS and HD models. Large amplitude solitary waves of narrow width are generated when the background packing fractions are smaller whilst for large background packing fractions, the amplitudes are smaller with broader solitary waves occurring. At $\eta_0 \approx 5.65 \times 10^{-3}$ for the HS model and $\eta_0 \approx 10.5 \times 10^{-3}$ for the HD model, the solitary wave parameters undergo a sharp variation which is associated with the existence of three solitary wave solution branches. When $\eta_0 \to 0$, the solitary wave amplitude a increases indefinitely until the model breaks down. For small η_0, the solutions obtained here are related to the upper branch of high amplitude, solitary waves.

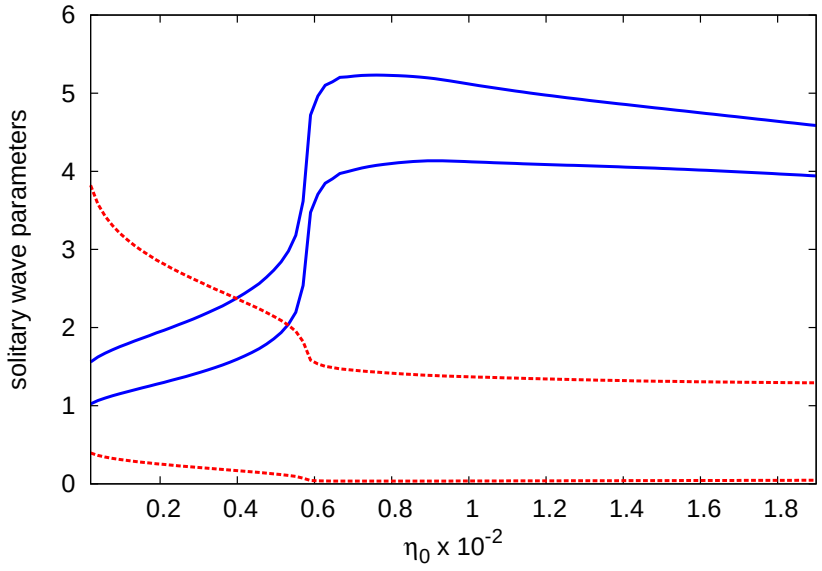

(a)

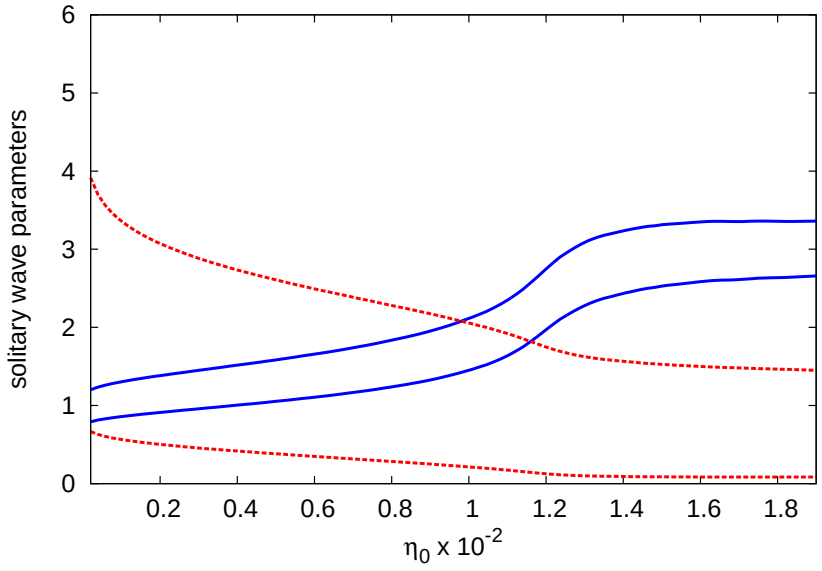

(b)

Figure 4.2: Variations of the solitary wave parameters in the DSW versus η_0 for (a) HS and (b) HD models. Shown are a (red upper dashed line), α (red lower dashed line), w (blue upper solid line) and β (blue lower solid line) from uniform soliton theory at $a_m = 0.5$.

4.3.1 Hard sphere and hard disk models

In this section, the numerical solutions of the colloidal equations (2.1.1) will be compared with the semi-analytical solutions developed for the (1+1)-D line DSW. We use a hybrid Runge-Kutta finite difference scheme for the numerical solutions. The details of the scheme are given in Appendix A.

Figure 4.3 shows the solitary wave amplitude, a versus the shock height a_m for the (a) HS and (b) HD (1+1)-D line DSW with the background packing fraction, $\eta_0 = 1 \times 10^{-2}$ and $k = 0$. The figures show uniform soliton theory and numerical solutions. Here, two different numerical estimates of the solitary wave amplitude are given. One estimate is the amplitude of the first solitary wave generated by the shock (the initial jump) at the z value for which this first wave has fully formed. The other estimate is the average maximum amplitude in the DSW. This approximation is obtained by taking the average between the z position at which the first solitary wave has formed and the z value where MI dominates. Here, the averaging process is needed because the largest amplitude is always changing, and the average value provides a good estimate. For this background packing fraction value, the HS model predicts a single stable solution branch, as the shock height a_m increases. For the HD model, the qualitative behaviour is different with an S-shaped response curve occurring. The solution undergoes a bifurcation at $a_m = 0.48$ at which it jumps from the low amplitude branch to the high amplitude branch. At the bifurcation point the amplitude of the solitary waves generated by the initial shock jumps from the low power to the high power stable branch, with a corresponding jump from (a,α)=$(1.56, 0.071)$ to (a,α)=$(1.85, 0.142)$. For both the HS and HD models, the comparisons are very good with errors between theory and numerics of up to 16% in the amplitude a.

Figure 4.4 shows the solitary wave amplitude, a versus the shock height a_m for the (a) HS and (b) HD (1+1)-D line DSW with the background packing fraction, $\eta_0 = 4 \times 10^{-3}$ and $k = 0$. Shown are the predictions of uniform soliton theory and numerical solutions.

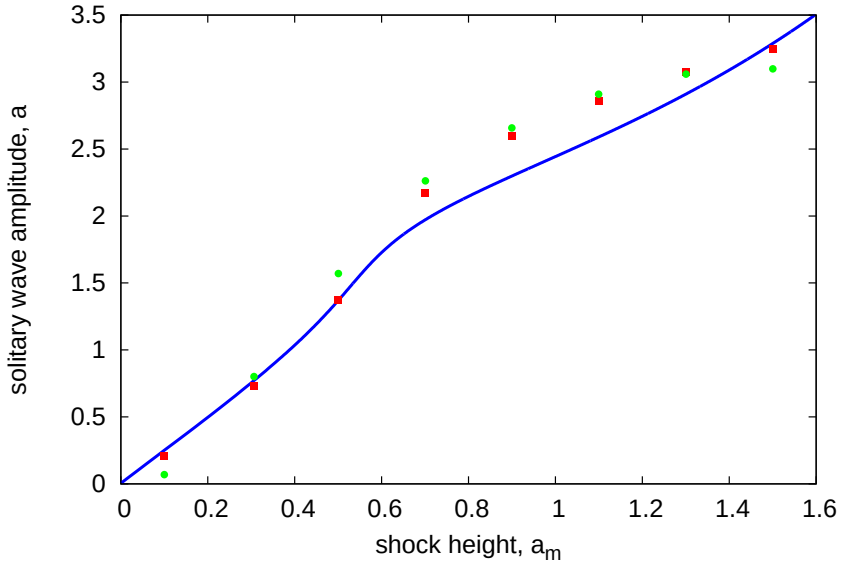

(a)

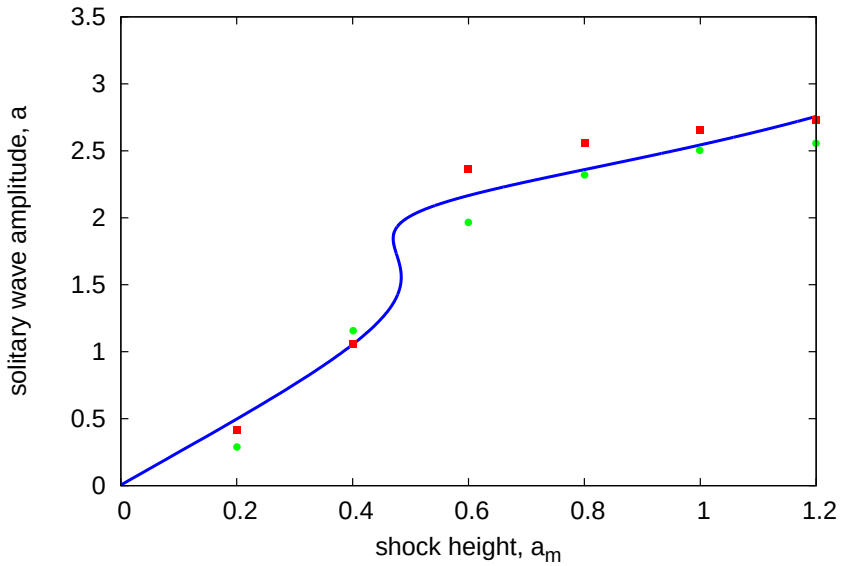

(b)

Figure 4.3: Solitary wave amplitude versus shock height, a versus a_m, for the (1+1)-D line DSW for (a) HS and (b) HD models. Shown are a (solid blue line) from uniform soliton theory, numerical estimates for the amplitude of the first solitary wave (red squares) and the average maximum amplitude (green circles). The other parameters are $\eta_0 = 1 \times 10^{-2}$ and $k = 0$.

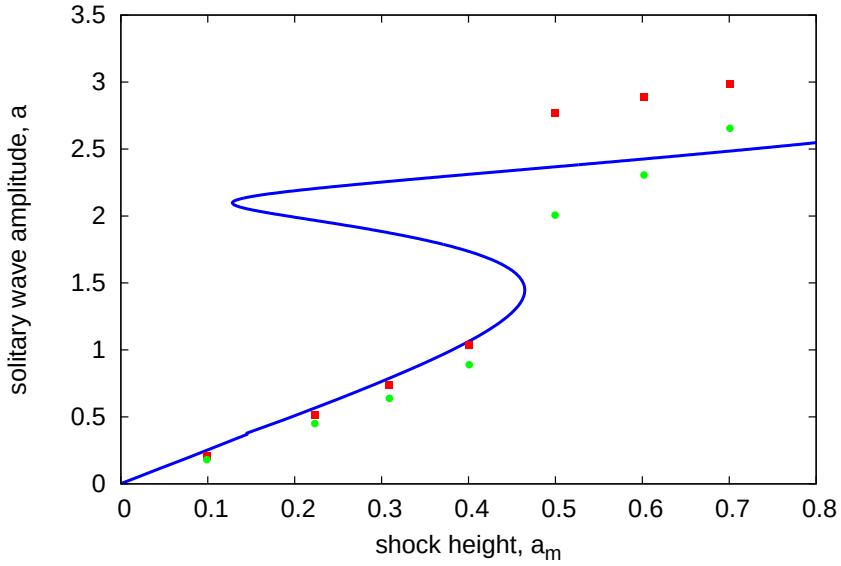

(a)

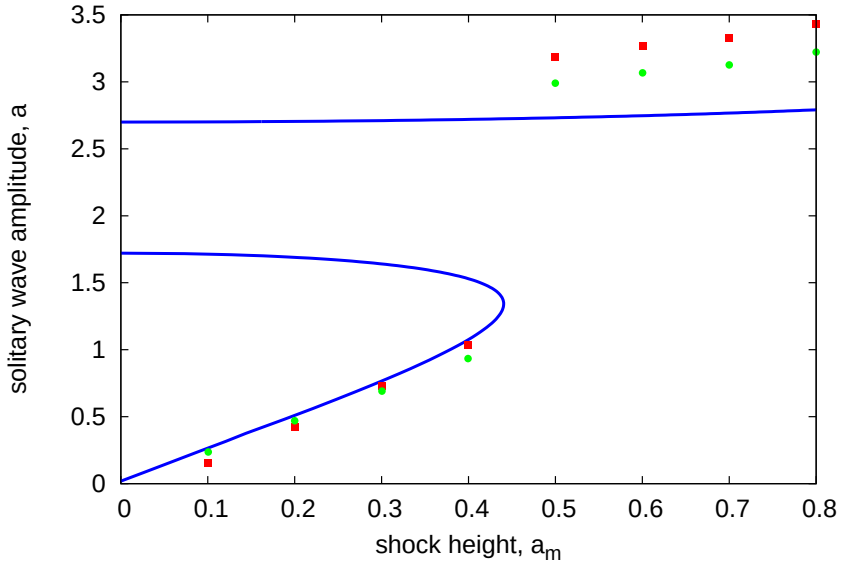

(b)

Figure 4.4: Solitary wave amplitude versus shock height, a versus a_m, for the (1+1)-D line DSW for (a) HS and (b) HD models. Shown are a (solid blue line) from uniform soliton theory, numerical estimates for the amplitude of the first solitary wave (red squares) and the average maximum amplitude (green circles). The other parameters are $\eta_0 = 4 \times 10^{-3}$ and $k = 0$.

For this background packing fraction value, the HS model has an S-shaped response curve with two turning points along the curve. The bifurcation point at which the solution jumps from the lower to the upper branch is at $a_m = 0.464$, from (a,α)=($1.45, 0.022$) to (a,α)=($2.34, 0.164$). However for the HD model, the upper stable branch has separated from the middle unstable branch. The jump occurs at $a_m = 0.44$ from (a,α)=($1.35, 0.018$) to (a,α)=($2.72, 0.413$). This bistable behaviour is related to the bistable power versus propagation constant curves, for low background packing fraction, as shown in Figure 3.2 and Figure 3.6 in Chapter 3. There is a good comparison between the theory and the numerical solutions with a maximum 16% error occurring for the range of the shock height values shown on the figure. The errors are higher on the upper branch as the wave amplitudes are higher there. The difference in the value of a_m at which the bifurcation occurs for the HS and HD models is very small with a 5% difference. The theoretical and numerical solutions for both colloids are quite similar before the jump, but the estimates start to differ on the upper branches.

Figure 4.5 shows the solitary wave amplitude, a versus the shock height a_m for the (a) HS and (b) HD (1+1)-D line DSW with background packing fraction $\eta_0 = 1 \times 10^{-3}$ and $k = 0$. Shown are the predictions of uniform soliton theory and numerical solutions. For this lower value of background packing fraction, both the HS and HD models have upper stable branches that have separated from the unstable branch. This separation happens because the jump amplitude a_m for the missing portion of the S-shaped curve has negative values. For the HS model, the bifurcation point at which the jump occurs is at $a_m = 0.42$. The jump is from (a,α)=($1.35, 4.89 \times 10^{-3}$) to ($a$,$\alpha$)=($3.19, 0.307$). For the HD model, the bifurcation point is at $a_m = 0.41$ with the jump from (a,α)=($1.34, 4.89 \times 10^{-3}$) to ($a$,$\alpha$)=($3.35, 0.564$). The difference in the HS and HD bifurcation points is very small, being only 2%. The amplitude of the flat upper branches for the HS and HD models have a variation up to 7% at $a_m = 0.8$. There exists a good comparison between the semi-analytical and the numerical solutions of the HS and HD models with errors of less than 10% on the lower branch and about 20% error on the upper branch.

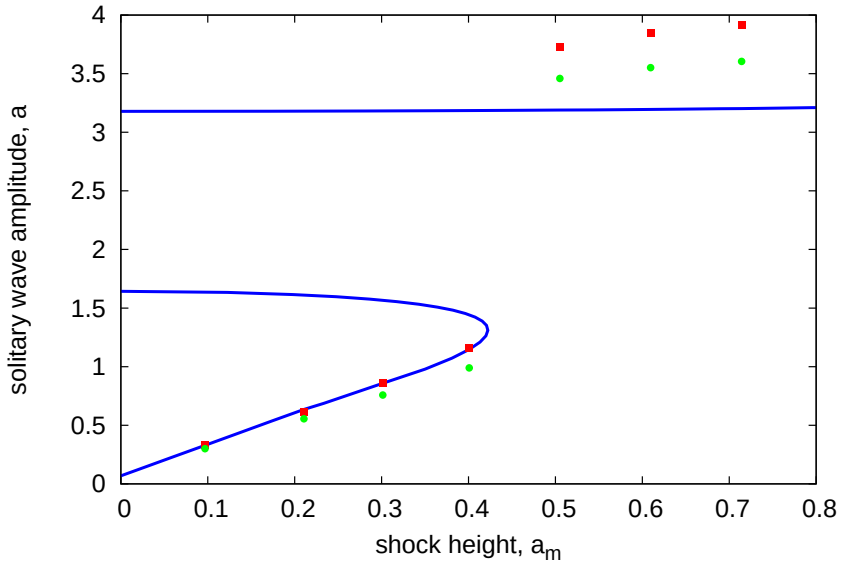

(a)

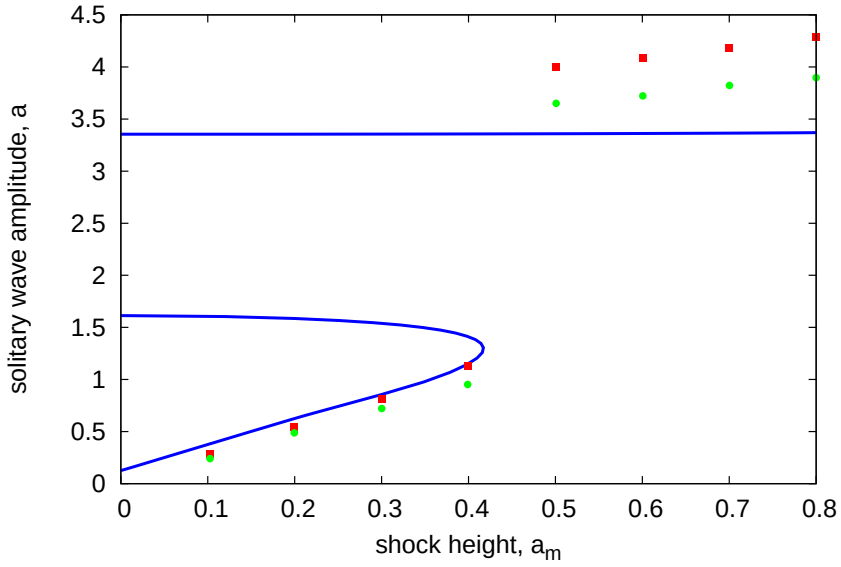

(b)

Figure 4.5: Solitary wave amplitude versus shock height, a versus a_m, for the (1+1)-D line DSW for (a) HS and (b) HD models. Shown are a (solid blue line) from uniform soliton theory, numerical estimates for the amplitude of the first solitary wave (red squares) and the average maximum amplitude (green circles). The other parameters are $\eta_0 = 1 \times 10^{-3}$ and $k = 0$.

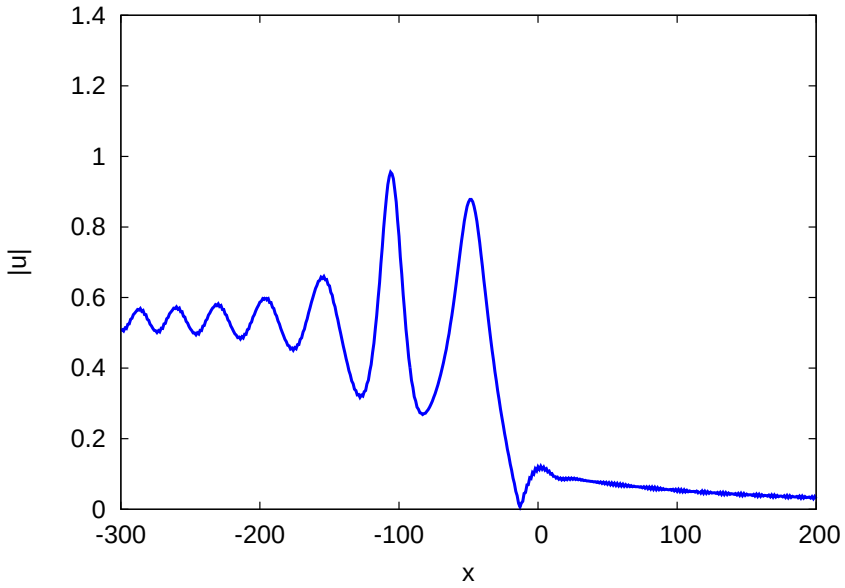

(a)

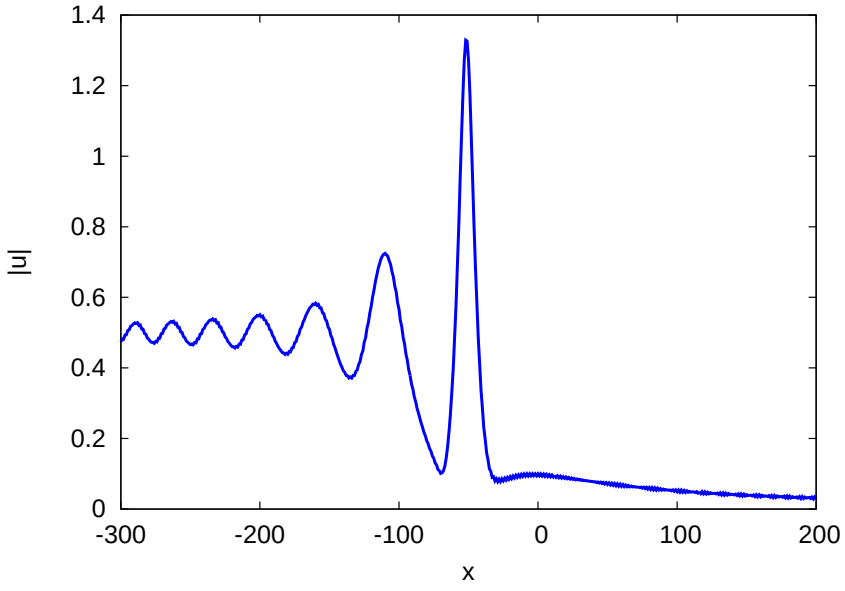

(b)

Figure 4.6: The electric field amplitude $|u|$ versus x for the (1+1)-D line DSW. Shown are the numerical solutions for (a) HS and (b) HD at $z = 1100$. The initial and background packing fractions are $\eta_0 = 1 \times 10^{-2}$ and $\eta_m = 1.29 \times 10^{-2}$.

Figure 4.6 shows the numerical solution for $|u|$ versus x for the (1+1)-D line DSW for both the (a) HS and (b) HD models at $z = 1100$. The initial and background packing fractions are $\eta_0 = 1 \times 10^{-2}$ and $\eta_m = 1.29 \times 10^{-2}$. For the HS model, two solitary waves have formed where the leading edge occurs at $x = -48.5$ and the highest peak is $a = 0.95$. The first HS solitary wave has a maximum amplitude $a = 1.59$, which forms at a slightly shorter length of $z = 920$. Between $z = 920$ and $z = 1100$ a second wave forms, which can interact with the first wave, causing the amplitudes to vary. The uniform soliton theory predicts a solitary wave amplitude of $a = 1.51$ and $\alpha = 0.05$ which is quite close to the numerical value with less than 5% error. For the HD model at $z = 1100$, the first solitary wave has developed to its maximum amplitude $a = 1.33$. Uniform soliton theory predicts $a = 1.37$ and $\alpha = 0.043$ which is again close to the numerical value with less than 3% error.

For both HS and HD models we can see the differences between the semi-analytical solutions and numerical predictions for the solitary wave amplitudes are very small. We do not show the packing fraction η_m because it has the same profile as $|u|$. For the HS model, the solitary waves will have a higher maximum amplitude, which occurs at a smaller value of z.

Figure 4.7 shows the numerical solution for $|u|$ versus x for the (1+1)-D line DSW for both the (a) HS and (b) HD models at $z = 2500$. The initial and background packing fractions are $\eta_0 = 1 \times 10^{-2}$ and $\eta_m = 1.29 \times 10^{-2}$ respectively. For a DSW described by a hyperbolic system of modulation equations, the DSW consists of an expansion fan. Here, as the modulation equations form an elliptic system and there is no hyperbolic expansion fan, the individual waves do not completely separate, see [109, 110]. Hence, the waves continue to interact with each other and they are not ordered by amplitude. For the HS model, there are five solitary waves formed where the fourth wave is the largest with $a = 1.11$. The maximum amplitude in the DSW, averaged over z is 1.09. The semi-analytical solitary wave for the HS model has amplitude $a = 1.51$ hence, the comparison between the semi-analytical solutions and numerical predictions differs by 26%. For the

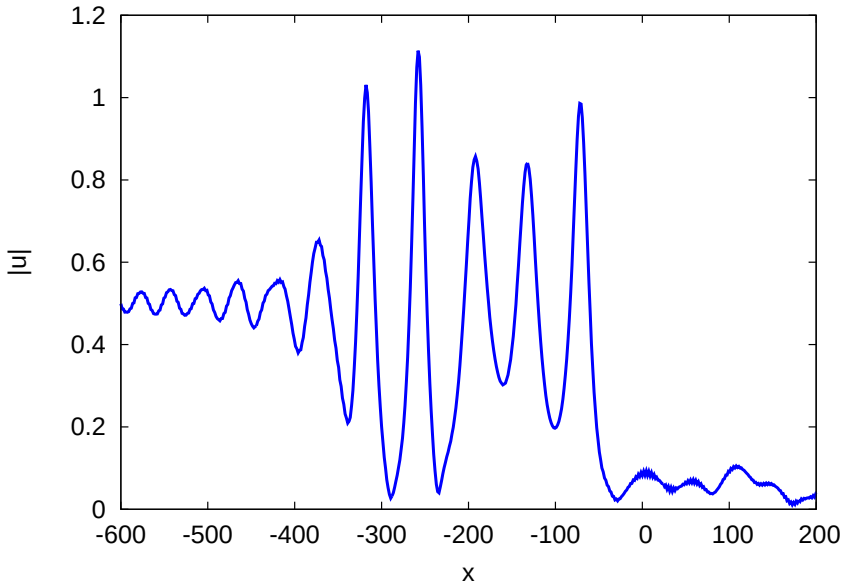

(a)

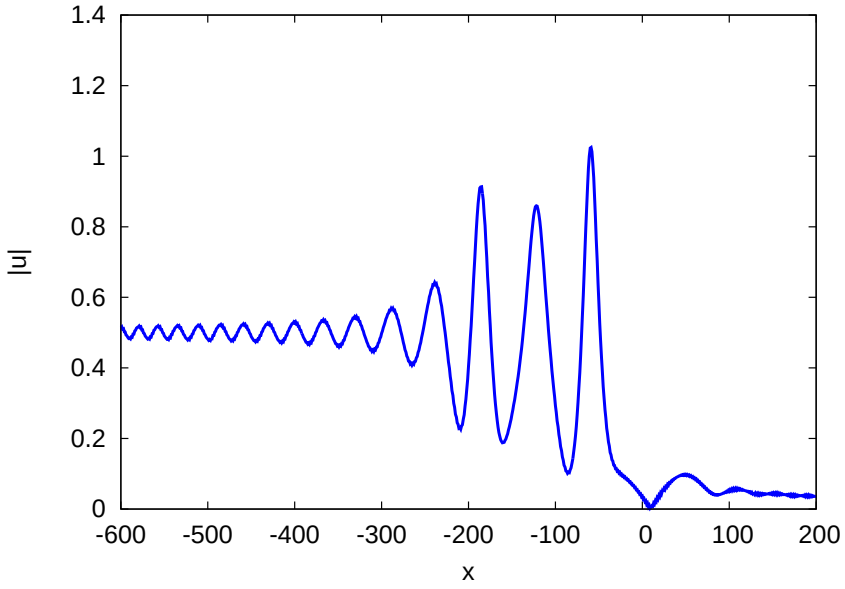

(b)

Figure 4.7: The electric field amplitude $|u|$ versus x for the (1+1)-D line DSW. Shown are the numerical solutions at the initial jump for (a) HS and (b) HD at $z = 2500$. The initial and background packing fractions are $\eta_0 = 1 \times 10^{-2}$ and $\eta_m = 1.29 \times 10^{-2}$.

HD model, only three solitary waves have formed where the leading edge solitary wave is the largest, with maximum amplitude of $a = 1.02$. The maximum amplitude in the DSW, averaged over z is $a = 0.94$. The semi-analytical solitary wave for the HS model has amplitude $a = 1.37$ hence, the comparison between the semi-analytical solutions and numerical predictions differ by 31%. The difference between these predictions is due to the large amplitude of the waves for which the semi-analytical sech profile is not as accurate, compared to actual solitary waves. The HS model predicts larger solitary waves amplitudes than the HD model.

4.3.2 Temperature dependent model

We now consider the HD model but with a temperature dependent second virial coefficient given by (3.1.2) where $B_2 = 2 - \frac{100}{T}$ and $B_2 \to 2$, the HD case, as the temperature becomes large. The choice of $\lambda = 0$ means that variation with temperature is inverse linear. This form of the second virial coefficient allows us to consider temperature dependent effects on the formation and structure of DSW.

Figure 4.8 shows the dispersive shock height, a_m at the bifurcation points versus the background packing fraction η_0 for the temperature dependent (1+1)-D line DSW. Three cases, $T = 50, 100,$ and 500 of the uniform soliton theory are shown. For $T = 50$, bifurcation points exists for $\eta_0 < 2.8 \times 10^{-2}$, while for $T = 100$ and $T = 500$, bifurcation points exist for $\eta_0 < 1.55 \times 10^{-2}$ and $\eta_0 < 1.12 \times 10^{-2}$ respectively. So, as temperature increases, the region of parameter space in which multiple steady-state solutions decreases, and the S-shaped response curve occurs only at lower values of η_0. A single, stable, a versus a_m solution branch will occur beyond these bifurcation points; these are the parameter values that separates the bi-stable and mono-stable regimes for the solitary wave solution of the (1+1)-D temperature dependent model. We see three solution branches (two stable, one unstable) when η_0 is less than the critical values mentioned above. As the temperature increases, the HD model limit is approached, for which the bifurcation

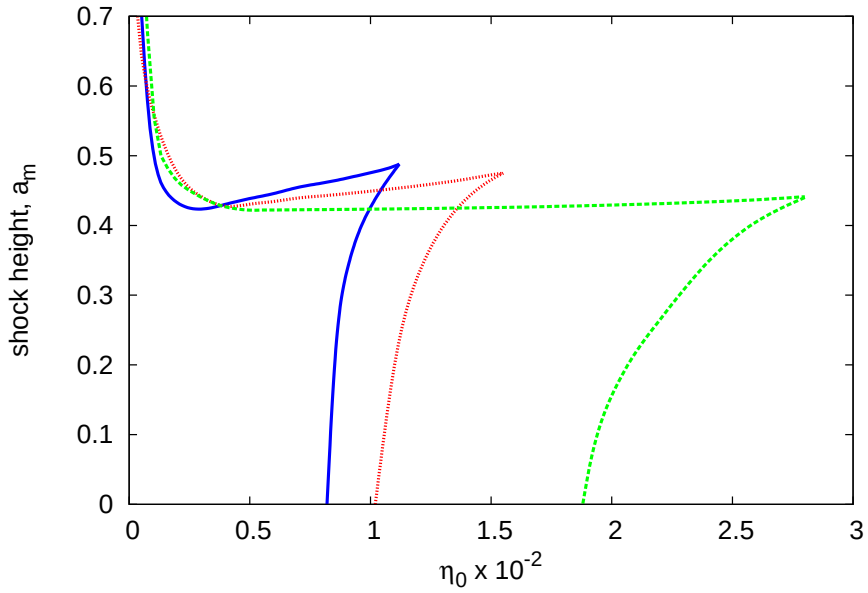

Figure 4.8: The dispersive shock height, a_m, at the bifurcation point versus the background packing fraction η_0 for the (1+1)-D line DSW. Shown are $T = 50$ (dashed green line), $T = 100$ (red dotted line) and $T = 500$ (solid blue line).

points occur when $\eta_0 < 1.05 \times 10^{-2}$.

Figure 4.9 shows the solitary wave properties, (the widths w and β and amplitudes α and a of the solitary waves) versus η_0 for the temperature dependent line DSW, as given by (2.2.6) and (4.2.7). The temperatures are (a) $T = 50$, (b) $T = 100$ and (c) $T = 500$ and the shock height $a_m = 0.52$. Each figure shows a jump in the width of the solitary waves, as η_0 increases. As the temperature increases, this jump occurs at a smaller value of η_0 and becomes more pronounced. This jump in the width of the wave occurs for $\eta_0 \approx 1.8 \times 10^{-2}$ for $T = 50$, $\eta_0 \approx 1.6 \times 10^{-2}$ for $T = 100$ and $\eta_0 \approx 1.1 \times 10^{-2}$ for $T = 500$. The solitary wave amplitudes decrease, as η_0 increases, and the rate of increase is faster for larger temperatures.

Figure 4.10 shows the solitary wave amplitude versus the shock height, a versus a_m for the temperature dependent line DSW for $T = 50$, $T = 100$ and $T = 500$ with the background packing fraction, $\eta_0 = 2 \times 10^{-2}$ and $k = 0$. Shown is the predictions of uniform soliton theory and numerical solutions. An S-shaped curve exists for $T = 50$, and unique curves for $T = 100$ and $T = 500$. The S-shaped response curve disappears

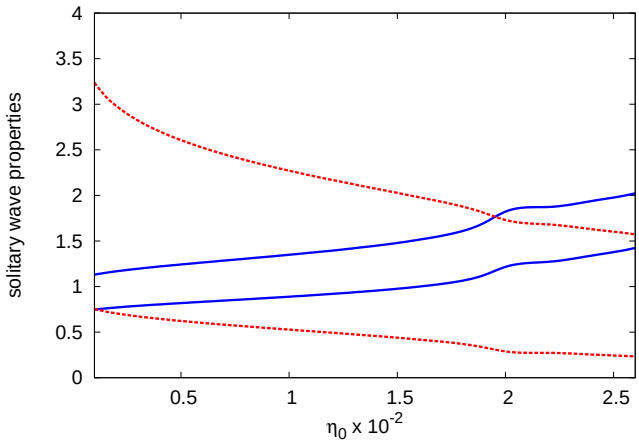

(a)

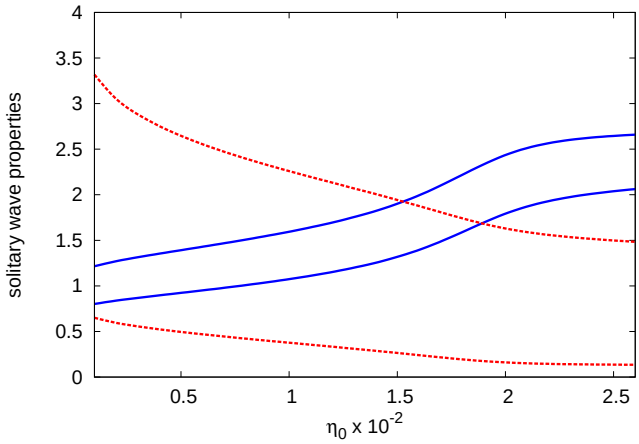

(b)

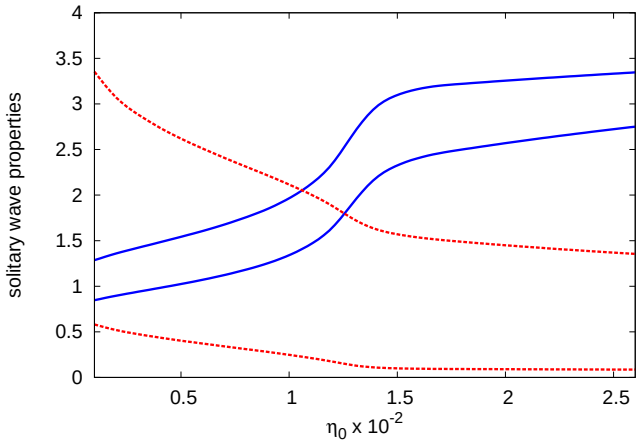

(c)

Figure 4.9: Variations of the solitary wave parameters in the DSW versus η_0 for the temperature dependent line DSW at (a) $T = 50$, (b) $T = 100$, and (c) $T = 500$. Shown are a (upper dashed red line), α (lower dashed red line), w (upper solid blue line) and β (lower solid blue line) from uniform soliton theory at $a_m = 0.52$ for all temperatures.

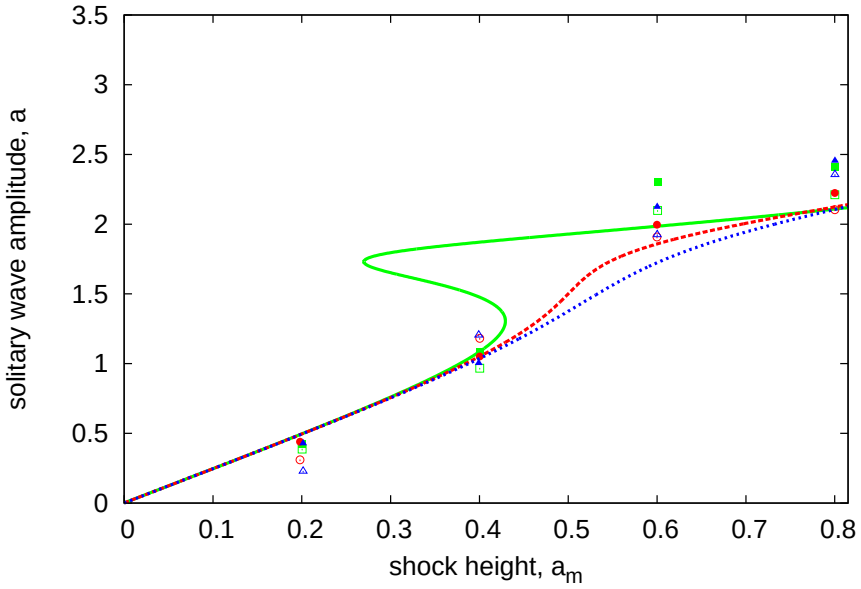

Figure 4.10: Solitary wave amplitude versus shock height, a versus a_m, for the temperature dependent line DSW. Shown are the uniform solitary theory for $T = 50$ (solid green line), $T = 100$ (dashed red line) and $T = 500$ (dotted blue line), numerical estimates for $T = 50$ (green squares), $T = 100$ (red circles) and $T = 500$ (blue triangles) for the first solitary wave and average maximum amplitude for $T = 50$ (green hollow squares), $T = 100$ (red hollow circles) and $T = 500$ (blue hollow triangles). The other parameters are $\eta_0 = 2 \times 10^{-2}$ and $k = 0$.

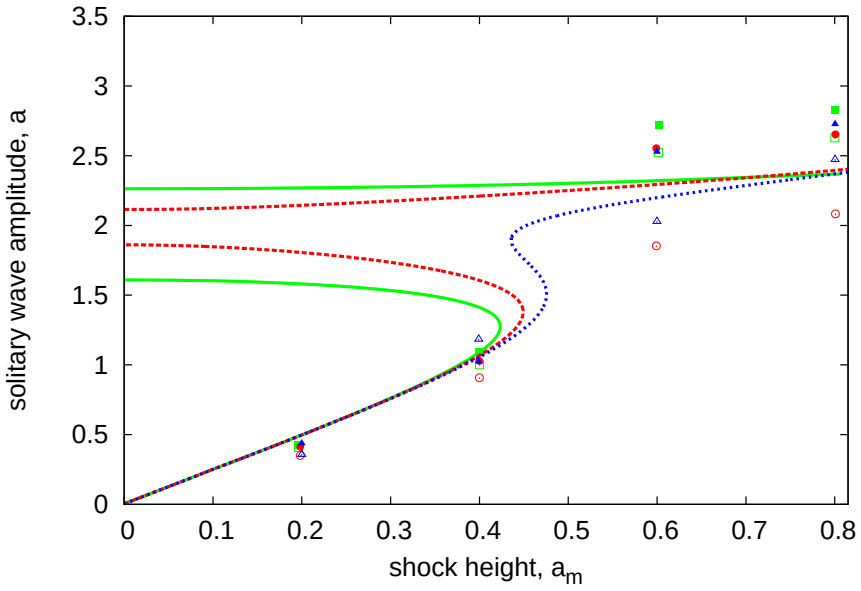

Figure 4.11: Solitary wave amplitude versus shock height, a versus a_m, for the temperature dependent line DSW. Shown are the uniform solitary theory for $T = 50$ (solid green line), $T = 100$ (dashed red line) and $T = 500$ (dotted blue line), numerical estimates for $T = 50$ (green squares), $T = 100$ (red circles) and $T = 500$ (blue triangles) for the first solitary wave and average maximum amplitude for $T = 50$ (green hollow squares), $T = 100$ (red hollow circles) and $T = 500$ (blue hollow triangles). The other parameters are $\eta_0 = 1 \times 10^{-2}$ and $k = 0$.

at $T \approx 90$. For $T = 50$, the bifurcation point occurs at $a_m = 0.43$ and the amplitude jumps from $(a, \alpha) = (1.31, 0.08)$ to $(a, \alpha) = (1.89, 0.39)$. For $T = 100$ and $T = 500$, single solution branches exist. This figure illustrates that temperature variations can have a dramatic effect on the solitary wave amplitude in the DSW. For low temperatures, a bifurcation point exists, at which a significant jump in solitary wave amplitude can occur. However at high temperatures this bifurcation in amplitude does not occur. There is a good comparison between the theoretical solutions and numerical estimates over the range of the graph, with is a maximum error of up to 19%. The curve for $T = 500$ is very close to the HD model with a maximum of 1% difference in the curve.

Figure 4.11 shows the solitary wave amplitude versus the shock height, a versus a_m for the temperature dependent line DSW at $T = 50$, $T = 100$ and $T = 500$ with the background packing fraction, $\eta_0 = 1 \times 10^{-2}$ and $k = 0$. The figure shows uniform soliton theory and numerical solutions. Multiple solution branches exist for all temperatures

except that the upper stable branches are separated from the middle unstable branch for $T = 50$ and $T = 100$. The S-shaped curves become separated at around $T \approx 120$. For $T = 50$, the bifurcation point at which the jump from the lower to the upper branch occurs is at $a_m = 0.42$, from (a,α)=($1.28, 0.04$) to (a,α)=($2.29, 0.54$). For $T = 100$, the bifurcation point occurs at $a_m = 0.46$ and the jump occurs at (a,α)=($1.38, 0.05$) to (a,α)=($2.23, 0.36$). For $T = 500$, the bifurcation point occurs at $a_m = 0.48$ and the jump occurs at (a,α)=($1.51, 0.06$) to (a,α)=($2.06, 0.22$). We can see here that as temperature increases, the bifurcation point also increases in magnitude. These results show excellent comparisons between the theoretical solutions and numerical estimates.

Figure 4.12 shows the numerical solution for $|u|$ versus x for the temperature dependent line DSW with $T = 50$ and $T = 100$. The initial packing fraction is $\eta_m = 1.27\times10^{-2}$ and the background packing fraction $\eta_0 = 1 \times 10^{-2}$. (a) shows the z values at which the first wave has fully formed. For $T = 50$, the first wave has fully formed at $z = 975$ while for $T = 100$, the wave has fully formed at $z = 1085$. (b) shows the result at z=1200 where the properties of the waves start to differ. The first solitary wave in (b) has developed to its maximum height at $a = 2.28$ for $T = 50$ and $a = 1.65$ for $T = 100$. Here we can see that as temperature increases, the maximum height for the solitary wave decreases. We then consider a longer propagation distance as shown in (c) where $z = 2500$ and we can see that a DSW has formed with four solitary waves for both models, but with significantly different maximum amplitude. The leading wave is the largest with $a = 2.32$ for $T = 50$ and $a = 1.33$ for $T = 100$. Again, the maximum height for the largest solitary wave decreases when temperature increases. The average maximum amplitude is $a = 1.55$ and $a = 0.97$ for $T = 50$ and $T = 100$, respectively, with corresponding semi-analytical solutions of $a = 1.31$ and $a = 1.24$. Thus, the differences between the semi-analytical solutions and the numerical predictions are 15% and 22%, for $T = 50$ and $T = 100$, respectively.

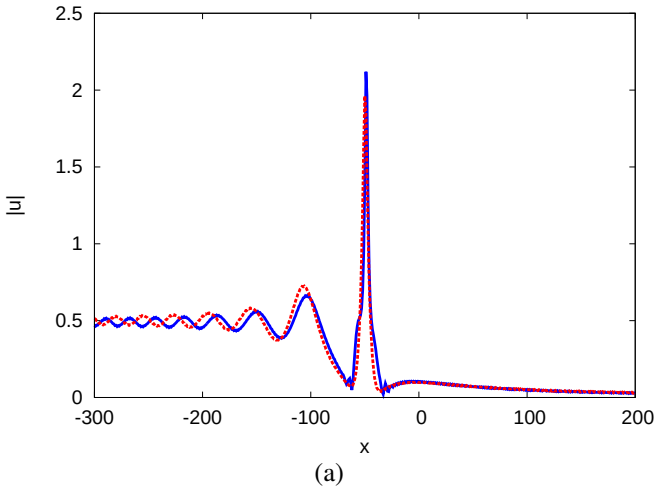

(a)

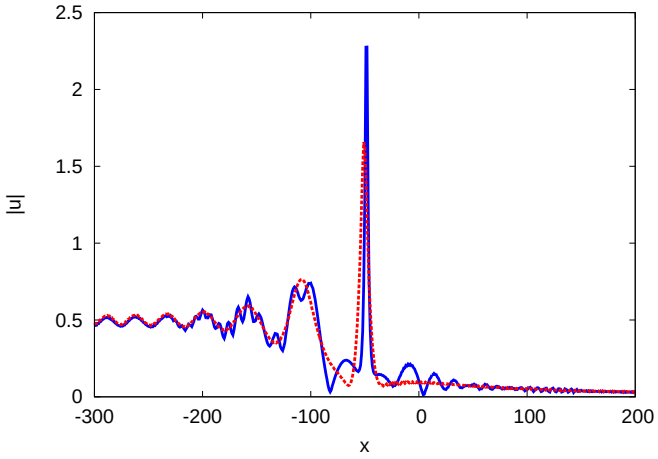

(b)

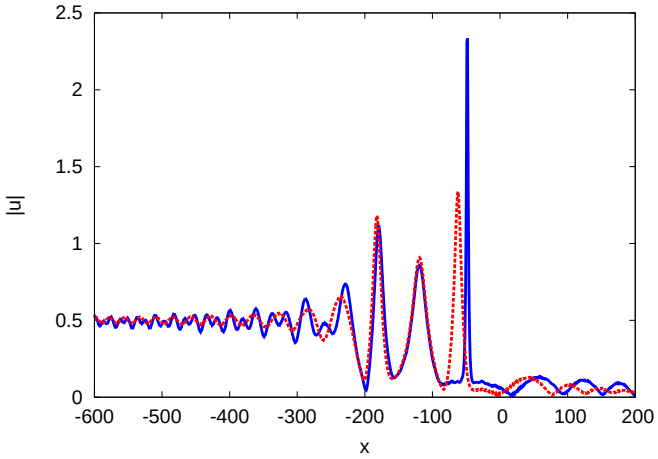

(c)

Figure 4.12: The electric field amplitude $|u|$ versus x for the temperature dependent line DSW. Shown are the numerical solutions at (a) the z values at which the first wave has fully formed (b) $z = 1200$ and (c) $z = 2500$ for temperature dependent models $T = 50$ (solid blue line) and $T = 100$ (dashed red line). The other parameters are $\eta_0 = 1 \times 10^{-2}$ and $\eta_m = 1.27 \times 10^{-2}$.

4.4 The (2+1)-D circular DSW

In this section, the semi-analytical solutions for a circular (2+1)-D DSW for both the HS model and a temperature dependent model is discussed. Solutions for the HD model will not be discussed here because the model is only appropriate for the line DSW. Here we use the HS coefficients (3.1.1). We also look at the effect of temperature by using the temperature dependent model as developed in Chapter 3. These choices allow us to explore the effects on the solitary waves and their stability as the temperature changes and the interactive forces change from repulsive to attractive. We also show that the theoretical results for the line DSW problem is able to generate results that are useful for describing the circular DSW problem at large radius where the solution properties can be deduced from the line DSW case.

For the (2+1)-D case, the colloid equations (2.1.1) with circular symmetry is discussed;

$$u = u(r, z), \quad \eta = \eta(r, z), \text{where } r = \sqrt{x^2 + y^2}, \tag{4.4.8}$$

with $\bigtriangledown^2 u$ given by $u_{rr} + \frac{1}{r}u_r$.

For the circular DSW, the boundary condition adopted here is

$$u = \begin{cases} a_m e^{i\theta}, & 0 < r < r_0, \\ 0, & r > r_0, \end{cases} \qquad \eta = \begin{cases} \eta_m, & 0 < r < r_0, \\ \eta_0, & r > r_0. \end{cases} \tag{4.4.9}$$

at $z = 0$ and $\theta = (1 - \exp -\alpha_1 r)kr$. At this condition, a_m and η_m are related by the same state relation as for the (1+1)-D case. This form is used because we want the boundary condition to have a quadratic chirp near the origin, where $\theta \to \alpha_1 k r^2$ as $r \to 0$. By using this form, we are sure that the Laplacian ∇^2 for the boundary condition (4.4.9) is bounded in the limit as $r \to 0$.

By applying the same parameters used in Marchant and Smyth [95], we choose $\alpha_1 =$

0.2 so that for $r \gtrsim 50$, the phase will be chirp free. Therefore, for any value at which r is large, we will get $\theta \to kr$, which represents the (1+1)-D continuous wave solution. Moreover, unlike the (1+1)-D case, the continuous wave will only be the exact solution of the (2+1)-D governing equations for a steady state DSW at which $k = 0$. For any value of $k > 0$, the continuous wave in (4.4.9) is only a correct approximation for $r \gg 1$ and will evolve in z, especially near the origin $r = 0$.

4.4.1 Hard sphere model

Figure 4.13 shows $|u|$ versus r for a HS circular DSW. Shown is the numerical solution of (2.1.1). The parameters are $\eta_0 = 1 \times 10^{-2}$, $\eta_m = 2.43 \times 10^{-2}$, $r_0 = 600$ and $\alpha_1 = 0.2$. We look at three different values of wavenumber to see how varying the wavenumber causes the DSW to evolve. For $k = 0$, the largest wave peak occurs at $z = 151$. For $k = 1.0$, the largest peak occurs at a longer length scale of $z = 210$. Finally, when $k = 1.5$, the largest peak occurs at $z = 271$. We note that $|u| \to a_m$ as $r \to 0$ for the stationary circular DSW, the continuous wave is an exact solution of the governing equations. The circular DSW for the HS model is similar to that considered by Marchant and Smyth [95] for the CS formula and we find a very close agreement between the numerical solutions for the two models with 2% difference.

For the HS model, when $k = 0$, the highest peak of the DSW occurs at $(a, \alpha) = (2.76, 0.31)$ at $r = 581$. These values are qualitatively similar to what have been obtained by Marchant and Smyth in [95] with only 2% difference in the a value. When we look at the case where $k \neq 0$, the circular DSW does not have the same profile as the stationary case as the circular DSW will propagate outwards, so the field intensity becomes low, and a central dark zone will be formed. This is qualitatively similar to what have been obtained by [90, 111] (see Figures 2 and 6 of [90] and Figure 5 of [111]). When $k = 1$, the peak amplitude is $(a, \alpha) = (2.38, 0.23)$ at $r = 788$ and when $k = 1.5$, the peak amplitude is $(a, \alpha) = (1.91, 0.13)$ at $r = 982$. If we compare these results to the CS model that

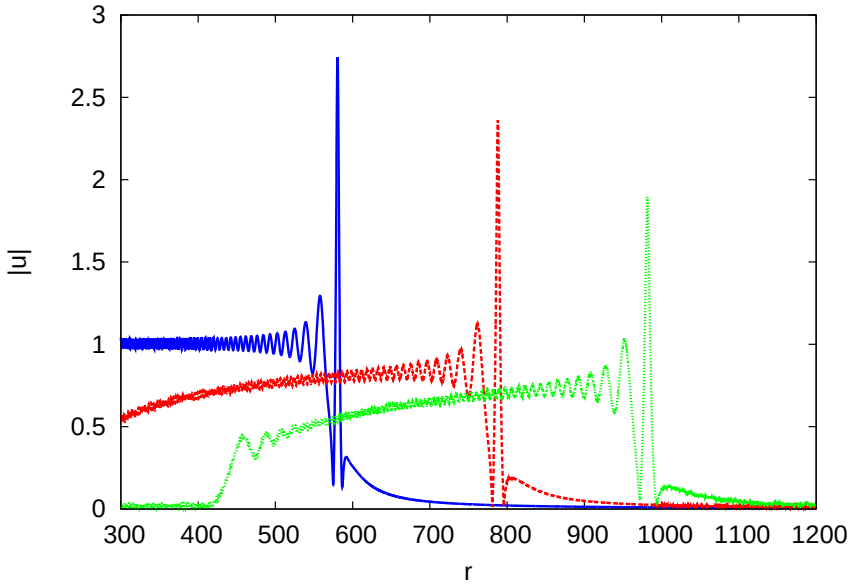

Figure 4.13: Electric field amplitude $|u|$ versus r for a HS circular DSW. The numerical solution of (2.1.1) is shown for $k = 0$ (solid blue line) at $z = 151$, $k = 1$ (dashed red line) at $z = 210$ and $k = 1.5$ (dotted green line) at $z = 271$. The other parameters are $\eta_0 = 1 \times 10^{-2}$, $\eta_m = 2.43 \times 10^{-2}$, $r_0 = 600$ and $\alpha_1 = 0.2$.

have been obtained by Marchant and Smyth [95], for $k = 1$, there is 4% difference in the value of a while for $k = 1.5$, the difference is 3%. The locations for the highest wave correspond to numerical values of $k = 0.996$ and $k = 1.479$, respectively. We can analytically show that the velocity is $V = k$ for the line DSW, therefore, the numerical propagation constants for the circular DSW obtained here are very close to the theoretical values in (1+1)-D HS model.

As r increases, the amplitudes of the waves in the expanding DSW decrease. This is referred to as geometric spreading. This is different to the (1+1)-D case for which the wave amplitudes in the DSW are independent of k. A simple geometric optics analysis shows that the electric field amplitude decreases like $a \sim r^{-1/2}$ for large r. By using this geometric optics analysis and numerical results for the stationary circular DSW we get a prediction for the amplitude of the largest wave in the bore of $a = (580.5/787.95)^{1/2}(2.76) = 2.37$ and $\alpha = (580.5/787.95)(0.3) = 0.23$ for $k = 1$. For $k = 1.5$, geometric optics gives predictions of $a = 2.13$ and $\alpha = 0.18$. Comparison of these results to the actual numerical

amplitudes of the expanding DSWs is excellent for $k = 1$ with almost 100% accuracy in a and α. However for $k = 1.5$, the prediction is still good but varies by about 10% and 33% for the amplitudes a and α.

As the DSW evolves further, the maximum amplitude for the line DSW varies in a complicated manner with z since there is an interaction between the individual waves of the DSW. For an expanding circular DSW, in order to allow for the effects of geometric spreading, we must modify the predictions of uniform soliton theory by combining it with geometric optics analysis. By applying this analysis, it is found that the average of the maximum amplitudes over the length of the DSW is compatible with the predictions from uniform soliton theory. For an expanding circular DSW, the z-weighted averages of the electric field in a domain extending from $z = 0$ to $z = z_1$ is

$$\frac{a}{z_1}\int_0^{z_1} \frac{dz}{(1+\frac{Vz}{r_0})^{\frac{1}{2}}} = \frac{2a}{Vz_1}[({r_0}^2 + kr_0z_1)^{\frac{1}{2}} - r_0], \tag{4.4.10}$$

For the line DSW and using the parameters from Figure 4.13, the predictions of uniform soliton theory are $a = 2.54$ and $\alpha = 0.252$. For the stationary circular DSW, with $r_0 = 600$ and $z_1 = 1200$, the average maximum amplitudes are $a = 2.56$ and $\alpha = 0.273$. By comparing these results with the line bore theoretical solution, there are 1% and 8% variations in the amplitudes a and α. However, for the expanding circular DSW, the predictions of the uniform soliton theory must be combined with (4.4.10). For the case where $k = 1$, by using $z_1 = 1200$ and other related information from Figure 4.13, the predictions are $a = 1.77$ and $\alpha = 0.13$ while the numerical averages are found to be $a = 1.64$ and $\alpha = 0.092$. From these solutions, we can see there exists 7% and 33% variation in the amplitudes a and α. When we look at the case where $k = 1.5$, the theoretical predictions are $a = 1.31$ and $\alpha = 0.06$ while the numerical averages are $a = 1.14$ and 0.04, thus there are variation by 12% and 34% in the amplitudes a and α. Hence we can conclude that the theoretical predictions are relatively close to the numerical solutions and the theoretical approach proposed here works well.

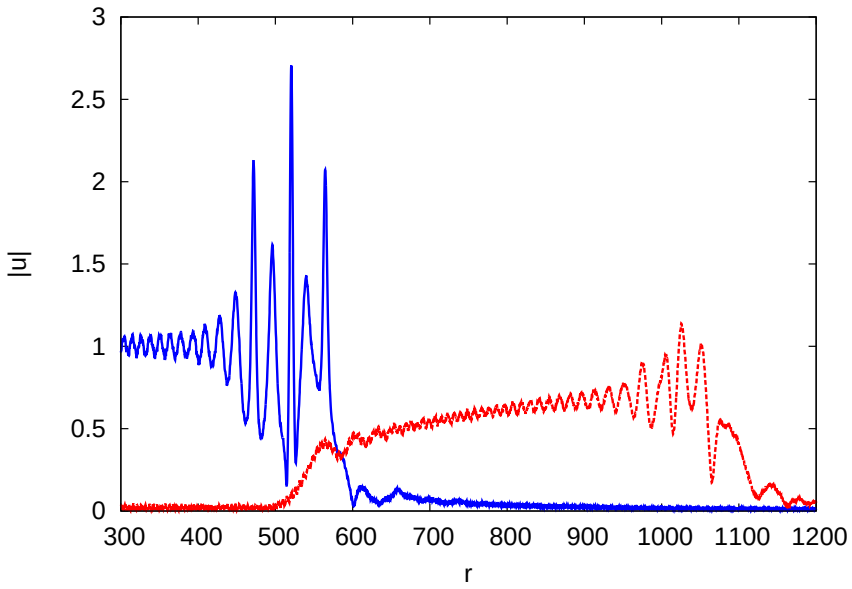

Figure 4.14: Electric field amplitude $|u|$ versus r for a HS circular DSW. The numerical solution of (2.1.1) is shown for $k = 0$ (solid blue line) and $k = 1$ (dashed red line) at $z = 500$. The other parameters are $\eta_0 = 1 \times 10^{-2}$, $\eta_m = 2.43 \times 10^{-2}$, $r_0 = 600$ and $\alpha_1 = 0.2$.

Figure 4.14 shows $|u|$ versus r for a HS circular DSW. Shown is the numerical solution of (2.1.1) at $z = 500$. The other parameters are $\eta_0 = 1 \times 10^{-2}$, $\eta_m = 2.43 \times 10^{-2}$, $r_0 = 600$ and $\alpha_1 = 0.2$. Shown are the cases for $k = 0$ and $k = 1$. When the circular DSW is stationary, the result obtained is qualitatively similar to the line DSW in Figure 4.7(a). As for the line DSW case, the individual waves do not completely separate, so they continue to interact with each other and are not ordered by amplitude. At $k = 0$, the largest solitary wave has $a = 2.71$ and $\alpha = 0.29$ at $r = 521$ while the leading edge of the DSW is located at $r = 575$. For $k = 1$, the leading edge is now at $r = 1071$ where the DSW propagates outwards. The amplitude of the largest wave in the expanding DSW is $a = 1.14$ and $\alpha = 0.03$. The locations for the highest wave correspond to numerical values of $k = 0.998$ and $k = 1.483$, respectively. These values are close to the theoretical estimates of $k = 1$ and $k = 1.5$ for the line DSW case.

Table 4.1: Data for the first fully formed solitary wave for the (2+1)-D circular DSW temperature dependent model. The parameters are $\eta_0 = 1 \times 10^{-2}$, $\eta_m = 2.43 \times 10^{-2}$, $r_0 = 600$ and $\alpha_1 = 0.2$. Numerical solutions of (2.1.1) are shown.

k	T	z	r	a	α
0	50	119	582.3	2.81	0.41
	100	142	581.0	2.78	0.33
	500	151	580.5	2.69	0.31
1	50	163	742.2	2.49	0.37
	100	200	777.5	2.42	0.26
	500	209	788.0	2.38	0.22
1.5	50	220	904.8	2.22	0.31
	100	257	981.8	1.98	0.16
	500	271	981.5	1.91	0.13

4.4.2 Temperature dependent model

For the circular DSW problem, we now consider the HS model with a temperature dependent second virial coefficient given by (3.1.3), where $B_2 = 4 - \frac{100}{T}$, so $B_2 \to 4$ as the temperature becomes large.

Figure 4.15 shows $|u|$ versus r for the temperature dependent (2+1)-D circular DSW. Shown is the numerical solutions of (2.1.1). The other parameters are $\eta_0 = 1 \times 10^{-2}$, $\eta_m = 2.43 \times 10^{-2}$, $r_0 = 600$ and $\alpha_1 = 0.2$ and for a scaled temperature of (a) $T = 50$, (b) $T = 100$, and (c) $T = 500$. We consider z values for which the first solitary wave has fully formed; Table 4.1 provides all the numerical values for these solitary waves. It can be seen that the z values at which the first solitary wave has formed increases as the temperature increases, while the amplitude of the fully formed solitary wave decreases, as the temperature increases.

Just like in the HS model, as r increases, the amplitudes of the waves in the expanding (2+1)-D circular DSW decrease like $a \sim r^{-\frac{1}{2}}$. So, by applying a geometric optics analysis and results for the stationary circular DSW, we get predictions for the amplitude of the largest wave in the DSW. Table 4.2 shows the predictions of the largest wave in the (2+1)-D circular DSW. The $k = 0$ results are those of uniform soliton theory for the line DSW

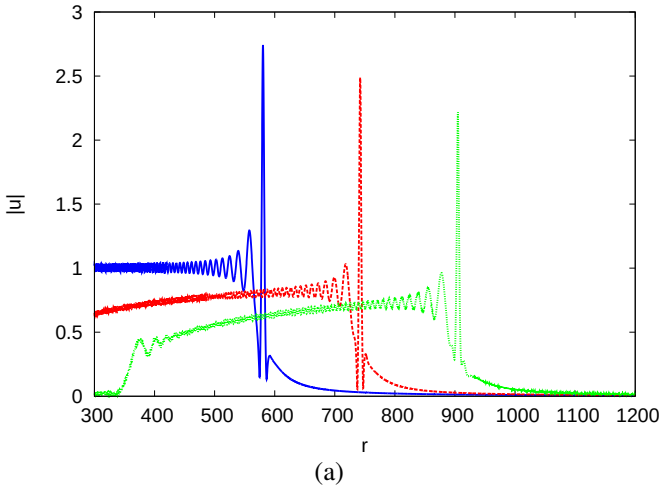

(a)

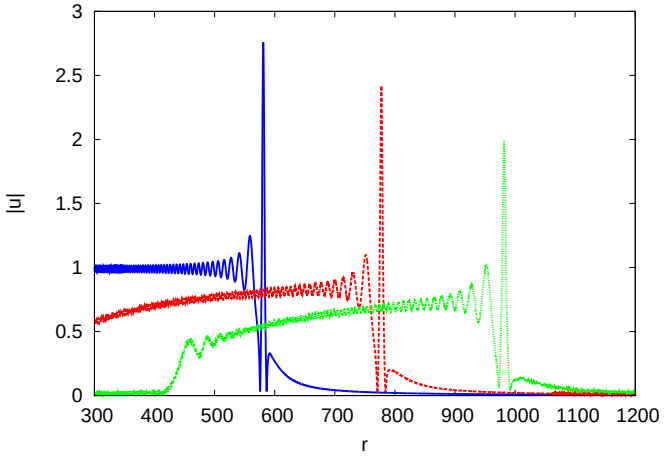

(b)

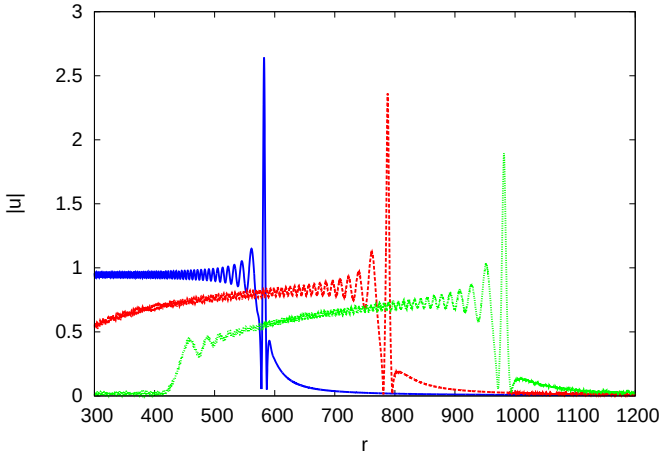

(c)

Figure 4.15: Electric field amplitude $|u|$ versus r for the temperature dependent circular DSW. Shown are numerical solutions of (2.1.1) for (a) $T = 50$, (b) $T = 100$, and (c) $T = 500$ for $k = 0$ (solid blue line), $k = 1$ (dashed red line) and $k = 1.5$ (dotted green line). The other parameters are $\eta_0 = 1 \times 10^{-2}$, $\eta_m = 2.43 \times 10^{-2}$, $r_0 = 600$ and $\alpha_1 = 0.2$.

Table 4.2: Predictions for the first fully formed solitary wave for the (2+1)-D circular DSW temperature dependent model. The parameters are $\eta_0 = 1 \times 10^{-2}$, $\eta_m = 2.43 \times 10^{-2}$, $r_0 = 600$ and $\alpha_1 = 0.2$. Shown are predictions using uniform soliton theory and geometrical spreading.

k	T	a	α
0	50	2.73	0.43
	100	2.59	0.39
	500	2.53	0.25
1	50	2.48	0.32
	100	2.40	0.25
	500	2.30	0.23
1.5	50	2.25	0.31
	100	2.15	0.21
	500	2.13	0.18

Table 4.3: Numerical solutions for the temperature dependent circular DSW for $|u|$ at $z = 500$. The parameters are $\eta_0 = 1 \times 10^{-2}$, $\eta_m = 2.43 \times 10^{-2}$, $r_0 = 600$ and $\alpha_1 = 0.2$.

k	T	r	a	α
0	50	525.3	2.66	0.41
	100	563.4	3.00	2.75
	500	520.7	2.72	2.76
1	50	1033.4	2.11	0.28
	100	1028.0	1.20	0.036
	500	1025.4	1.15	0.035

case. These results are very close to the actual numerical amplitudes of the stationary and expanding DSWs. The predictions of the amplitude a are very good for all cases, as compared to the numerical results, with only a maximum of 11% error. However, the predictions for the α values are higher in comparison with the numerical results with a maximum of 43% error.

Figure 4.16 shows $|u|$ versus r for the temperature dependent circular DSW. Shown is the numerical solutions of (2.1.1) at $z = 500$. The other parameters are $\eta_0 = 1 \times 10^{-2}$, $\eta_m = 2.43 \times 10^{-2}$, $r_0 = 600$ and $\alpha_1 = 0.2$ and for a scaled temperature of (a) $T = 50$, (b) $T = 100$, and (c) $T = 500$. The highest amplitudes for the circular DSW are recorded in Table 4.3 for the stationary circular DSW $k = 0$ and expanding circular DSW with $k = 1$.

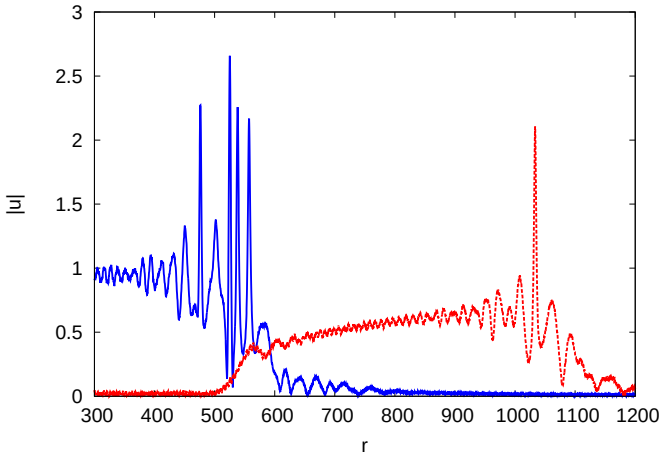

(a)

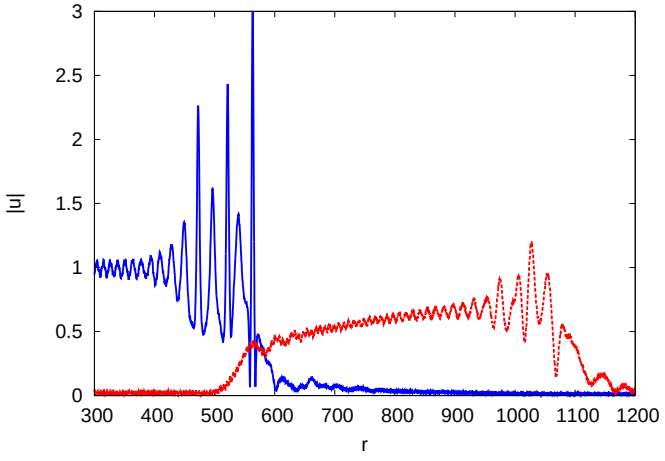

(b)

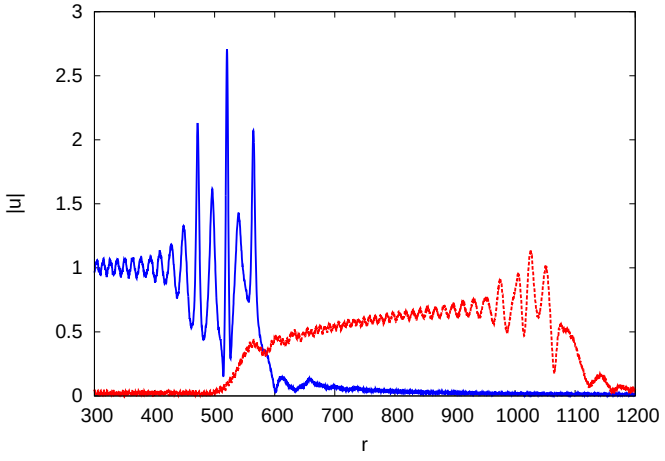

(c)

Figure 4.16: Electric field amplitude $|u|$ versus r for the temperature dependent circular DSW. Shown are numerical solutions of (2.1.1) for (a) $T = 50$, (b) $T = 100$, and (c) $T = 500$ for $k = 0$ (solid blue line) and $k = 1$ (dashed red line) at $z = 500$. The other parameters are $\eta_0 = 1 \times 10^{-2}$, $\eta_m = 2.43 \times 10^{-2}$, $r_0 = 600$ and $\alpha_1 = 0.2$.

Table 4.4: Predictions of uniform soliton theory and numerical averages of the stationary and expanding circular DSW for $z = 500$. The parameters are $\eta_0 = 1 \times 10^{-2}$, $\eta_m = 2.43 \times 10^{-2}$, $r_0 = 600$ and $\alpha_1 = 0.2$.

		Theoretical Predictions		Numerical Averages	
k	T	a	α	a	α
0	50	2.44	0.24	2.55	0.26
	100	2.28	0.22	2.26	0.20
	500	2.05	0.16	2.03	0.15
1	50	1.57	0.16	1.63	0.18
	100	0.89	0.022	0.86	0.021
	500	0.85	0.017	0.82	0.016

For a fixed z value, the maximum amplitude can be significantly different to the long z average, hence the wide differences from the long term averages in Table 4.4.

Table 4.4 shows the z-weighted numerical average amplitudes, using (4.4.10) and the uniform soliton theory for the line DSW, together with the geometrical optics analysis. We see that as temperature increases, the average maximum amplitude decreases. The difference between the theoretical and numerical solutions are quite small with a maximum of 4% and 11% errors in the a and α values. The theoretical approach for the circular DSW, that of using uniform soliton theory for the line DSW, together with geometric optics considerations is remarkably successful in predicting numerical amplitudes in the circular DSW, both for the initial wave and the long z average amplitude.

4.5 Summary

This chapter incorporates semi-analytical solutions for colloidal solitary waves and uniform soliton theory to predict the amplitude of solitary waves that form in colloidal dispersive shock waves. The governing equations are formulated using a series for the non-ideal gas law with hard sphere, hard disk and temperature dependent models all considered. The approximation for the solitary wave amplitudes is found to give good to excellent com-

parisons with numerical estimates. Three qualitatively different solitary wave amplitude versus jump height diagrams are obtained depending on the value of background packing fraction. When the background packing fraction is small, the upper solution branch separates from the middle unstable branch. At moderate values, we obtain an S-shaped response curve results, with multiple solution branches. For large background packing fractions, a single stable solution branch occur.

Chapter 5

Conclusion

5.1 Concluding remarks

This thesis examines semi-analytical solutions for colloidal solitary waves in the both one-dimensional and two-dimensional geometries and extends this work to a consideration of the formation of a dispersive shock wave in colloidal media. The governing equations are formulated using a series for the non-ideal gas law with hard sphere, hard disk and temperature dependent models all considered.

The formulation of the colloidal equations used throughout this research, which incorporates a series form for the compressibility, proves a convenient test bed for exploring different particle interaction models. It is hoped that this theoretical study will encourage experimental investigations of colloidal solitary waves and temperature dependent particle interaction effects.

An effective technique for deriving semi-analytical solutions that describes the stability and evolution of NLS-type systems is called variational approach. This approach is termed modulation theory and is based on using an averaged Lagrangian and suitable trial functions. From this approach, the approximate trial function method has been applied

to many problems in nonlinear optics and has been found to give solutions in excellent agreement with numerical and experimental results.

The differences in the behaviour of the hard sphere and hard disk cases is due to geometric effects. There are also some important differences in the properties of one-dimensional (stable) and two-dimensional (unstable) solitons of the related NLS equation, thus it is not surprising that geometrical effects also lead to significant differences in the stability properties of temperature dependent colloidal solitary waves. We obtained that, bistable behaviour occur at low to medium packing fractions, and single stable branch occurs at large packing fractions. For the temperature dependent model, multiple solution branches occur at larger temperature while at lower temperature, a single stable branch occur.

The effects of temperature dependency, on the particle interactions, is also explored as the interaction forces vary from attractive to repulsive. The results show that the regions of parameter space in which multiple solution branches occur vary significantly with temperature. For the (1+1)-D geometry increasing the temperature increases the parameter region in which multiple solutions occur, while for the (2+1)-D geometry the opposite effect occurs, with the parameter region shrinking as the temperature increases. This indicates the importance of geometrical effects on colloidal solitary wave properties and the need to use an appropriate particle interaction model.

An interesting extension to the model considered here would be to include thermal effects, due to the light beam heating the colloid and temperature losses from a finite boundary domain. This model would have some similarities to spatial solitary waves in thermal media [54], but the refractive index would depend both on particle density and temperature.

By using uniform soliton theory, the semi-analytical solitary wave solutions for the one-dimensional (line DSW) and two-dimensional (circular DSW) cases are used, together with conservation laws, to predict solitary wave amplitudes in a dispersive shock

wave. This approximation has found to give good to excellent comparisons with numerical estimates. The semi-analytical theory developed for the line DSW geometry also works well for the circular DSWs of large initial radius, giving accurate predictions.

The uniform soliton theory can be used directly for a stationary circular DSW, but must be combined with a geometric spreading analysis for an expanding circular DSW. The semi-analytical solutions for a circular DSW with both the HS model and a temperature dependent model are discussed. Comparisons between the numerical results and theoretical predictions are good for both the HS and temperature dependent models. The temperature dependent model results in changes to the parameter space, in which multiple solutions branches occur. From this semi-analytical theory, the critical background packing fractions at which multi-stability is lost are well predicted and changes in temperature are shown to effect the bifurcation patterns and the turning points.

It is hoped that this theoretical study will encourage experimental investigations of colloidal solitary waves, dispersive shock waves in colloidal media and temperature dependent particle interaction effects. The model and semi-analytical solutions developed here could be easily used by experimental groups simply by selecting appropriate virial coefficients, which correspond to their experimental colloidal medium. Hence we believe that the colloidal model equations and solutions presented here provide an extremely useful testbed for exploring different colloidal media and particle interaction models.

Appendix A

The numerical schemes

A.1 One-dimensional solitary waves

For the (1+1)-dimensional solitary waves, the numerical solutions of the colloid equation (2.1.1) were obtained by using centred finite-differences in the spatial coordinate x, and a fourth-order Runge-Kutta method for the time-like propagation direction z. We choose this method because of its high accuracy, relative to its computational cost. We discretize the solution as

$$\begin{aligned} u_{m,n} &= u(z_m = m\Delta z, x_n = n\Delta x), \\ \eta_{m,n} &= \eta(z_m = m\Delta z, x_n = n\Delta x), \quad n = 1, \ldots, N. \end{aligned} \tag{A.1.1}$$

We can write the colloid equation (2.1.1) in the form of an ode by discretizing the terms involving x-derivatives

$$\begin{aligned} u_{mz} = f(u_{m,n}) = \frac{i}{2\Delta x^2}(u_{m,n+1} + u_{m,n-1} - 2u_{m,n}) \\ + \frac{i}{2}(u_{m,n+1} + u_{m,n-1})(\eta_{m,n} - \eta_0), \quad \text{where} \quad |u_{m,n}|^2 = g(\eta_{m,n}) - g_0. \end{aligned}$$

The fourth order Runge-Kutta method then gives the solution at z_{m+1} as

$$u_{m+1,n} = u_{m,n} + \frac{1}{6}(a_{m,n} + 2b_{m,n} + 2c_{m,n} + d_{m,n}), \quad \text{where} \tag{A.1.2}$$
$$a_{m,n} = \Delta z f(u_{m,n}), b_{m,n} = \Delta z f(u_{m,n} + \frac{a_{m,n}}{2})$$
$$c_{m,n} = \Delta z f(u_{m,n} + \frac{b_{m,n}}{2}), d_{m,n} = \Delta z f(u_{m,n} + c_{m,n}).$$

The packing fraction η is defined as an implicit function of u. Thus, an explicit expression is needed in order to apply the Runge-Kutta method (A.1.2) for a small change in η corresponding to a small change in u. Expanding the second of (2.1.1) gives

$$\frac{\delta\eta = u\delta u^* + u^*\delta u}{g'(\eta)} \tag{A.1.3}$$

which is used to help calculate the expressions for b, c and d at each z-step in the Runge-Kutta method. Once $u_{m+1,n}$ is found, the corresponding value of $\eta_{m+1,n}$ is calculated by Newton iteration using the second of (2.1.1). At the boundaries, the values of u and η from (4.2.1) at $x = \pm\infty$ are applied. The accuracy of the numerical method at each z-step is $O(\Delta z^4, \Delta x^2)$. The step size used were $\Delta x = 0.15$ and $\Delta z = 0.01$

A.2 Two-dimensional solitary waves

For the (2+1)-dimensional solitary waves, we consider the colloid equation (2.1.1) with circular symmetry, i.e. $u = u(r, z)$ and $\eta = \eta(r, z)$, where $r = \sqrt{x^2 + y^2}$. The numerical solutions of the were obtained by using the same numerical scheme as for the (1+1)-D waves. centred finite-differences in the spatial coordinate r, and a fourth-order Runge-Kutta method for the time-like propagation direction z. We discretize the solution as

$$\begin{aligned} u_{m,n} &= u(z_m = m\Delta z, r_n = n\Delta r), \\ \eta_{m,n} &= \eta(z_m = m\Delta z, r_n = n\Delta r), \quad n = 1, \ldots, N. \end{aligned} \tag{A.2.4}$$

We can write the colloid equation (2.1.1) in the form of an ode by discretizing the terms involving r-derivatives

$$u_{mz} = f(u_{m,n}) = \frac{i}{2\Delta r^2}(u_{m,n+1} + u_{m,n-1} - 2u_{m,n})$$
$$+\frac{i}{4r\Delta r}(u_{m,n+1} - u_{m,n-1}) + \frac{i}{2}(u_{m,n+1} + u_{m,n-1})(\eta_{m,n} - \eta_0),$$
$$\text{where } |u_{m,n}|^2 = g(\eta_{m,n}) - g_0.$$

The remaining details of the solutions are then described by (A.1.2) and (A.1.3), as for the (1+1)-D scheme.

A.3 Steady state two-dimensional solitary waves

It is also necessary to find steady-state solitary wave profiles by a direct iteration method. For steady state (2+1)-D solitary waves solutions, a variety of different numerical schemes have been used, see Yang [112]. We consider the Imaginary Time Evolution Method (ITEM) for this work following the implementation used by Yang [113, 114].

To find solitary wave solutions of the governing equations (2.1.1), solitary waves are sought in the form

$$u(x,z) = A(x)e^{i\sigma z}, \quad \eta(x,z) = \eta(x), \tag{A.3.5}$$

where $A(x)$ and $\eta(x)$ are real-valued, localized functions, and σ is the propagation constant. Then, from equations (2.1.1) and (A.3.5), $A(x)$ is found to satisfy the equation

$$L_{00}A = \sigma A, \quad \text{where } L_{00} \equiv \frac{1}{2}\bigtriangledown^2 + (\eta - \eta_0)A. \tag{A.3.6}$$

For this research, L is the operator which corresponds to the matrix once a finite difference approximation for $\frac{\delta^2}{\delta x^2}$ is applied. For the ITEM method we consider the equation $A_z = L_{00}A$. This equation is numerically integrated using Euler method. At each iteration A_n, the solution must be normalized to a fixed power to prevent the solution from diverging

to infinity or decaying to zero. The ITEM iterative scheme is

$$A_n{}^* = \frac{P}{< A_n, A_n >} A_n, \;\; A_n = (1 + L_{00}\Delta z) A_{n-1}^*, \;\; < g, h >= \int_{-\frac{L}{2}}^{\frac{L}{2}} g(x)h(x)\mathrm{d}x, \tag{A.3.7}$$

where P is the fixed power of the converged solitary waves and Δz is the size of the discretization step. Note that Δz does not correspond to a step in spatial coordinate z, but is just a discretization step. The system (A.3.7) is iterated until the solution converges.

A.4 Steady-state one-dimensional solitary waves

In the (1+1)-D case, finding steady-state solitary wave profiles is simpler as the governing equations can be integrated once. Let $u(x, z) = A(x)e^{i\sigma z}$, which gives

$$-\sigma A + \frac{1}{2}A_{xx} + (\eta - \eta_0)A = 0. \tag{A.4.8}$$

We multiply (A.4.8) by A_x and integrate terms. We also have the relationship $A^2 = g(\eta) - g(\eta_0)$. Differentiating this gives $2AA_x = g'(\eta)\eta_x$. Substituting this into the third term and integrating gives

$$-\sigma A^2 + \frac{{A_x}^2}{2} + \int_0^\infty (\eta - \eta_0)g'(\eta)\mathrm{d}\eta = 0, \;\; g'(\eta) = \frac{1}{\eta} + 2B_2 + 3B_3\eta + \cdots . \tag{A.4.9}$$

So substituting $g'(\eta)$ into (A.4.9) and integrating gives

$$-\sigma A^2 + \frac{{A_x}^2}{2} + \eta + B_2\eta^2 + 3B_3\eta^3 - \eta_0(\ln\eta + 2B_2\eta + \frac{3}{2}B_3\eta^2) + \cdots = F(\eta_0). \tag{A.4.10}$$

In the limit as $x \to \infty$, $A \to 0$ and $\eta \to \eta_0$, so

$$F(\eta_0) = \eta_0(1 - \ln\eta + B_2\eta_0 - 2B_2 + B_3{\eta_0}^2 - \frac{3}{2}B_3\eta_0) + \cdots . \tag{A.4.11}$$

The expression (A.4.10) can be rearranged into an integral which can be solved by quadrature methods. This allows numerical power versus $\log \sigma$ curves to be obtained.

References

[1] J.S Russell. Report on waves. *Report of the fourteenth meeting of the British Association for the Advancement of Science*, 1844.

[2] J.V. Boussinesq. Thorie de lintumescence liquide appele onde solitaire ou de translation se propageant dans un canal rectangulaire. *C. R. Acad. Sci. Paris*, 72:755–759, 1871.

[3] Lord Rayleigh. On waves. *Phil. Mag.*, 1:257–279, 1876.

[4] N. Zabusky and M. Kruskal. Interaction of "solitons" in collisionless plasma and the reference of initial states. *Phys. Rev. Lett.*, 15:240–243, 1965.

[5] D. Korteweg and G. de Vries. On the change of form long waves advancing in a rectangular canal and on a new type of long stationary waves. *Phil. Mag.*, 39:422–443, 1895.

[6] E. Fermi, J. Pasta, and S. Ulam. Studies of nonlinear problems: Document 1a-1940. *Los Alamos Scientific Laboratory*, 1955.

[7] M.J. Ablowitz, D.J. Kaup, A.C. Newell, and H. Segur. The inverse scattering transform-Fourier analysis for nonlinear problems. *Stud. Appl. Math.*, 53:249–315, 1974.

[8] M.J. Ablowitz and H. Segur. Solitons and the inverse scattering transform. 1981.

[9] M.J. Ablowitz and P.A Clarkson. *Solitons, nonlinear evolution equations and inverse scattering*. Cambridge University Press, Cambridge, U.K., 1991.

[10] C. Gardner, J. Greene, M. Kruskal, and R. Miura. Method for solving the Korteweg-de Vries equation. *Phys. Rev. Lett.*, 19:1095–1097, 1967.

[11] A. Newell. Solitons in mathematics and physics. *SIAM*, 1985.

[12] R. Hirota. *Phys. Rev. Lett.*, 27:1192, 1971.

[13] V.E. Zakharov. Stability of periodic waves of finite amplitude on the surface of a deep fluid. *J. Appl. Mech. Tech. Phys.*, 9:190–194, 1968.

[14] V. E. Zakharov. The Instability of Waves in Nonlinear Dispersive Media. *J. Exp. Theor. Phys.*, 24:1107–1114, 1967.

[15] Y. C. Ma. The perturbed plane-wave solutions of the cubic Schrödinger equation. *Stud. Appl. Math.*, 60:43–58, 1979.

[16] K.B. Dysthe and K. Trulsen. Note on Breather type solutions of the NLS as models for freak-waves. *Phys. Scripta*, T82:48–52, 1999.

[17] A.R. Osborne, M. Onorato, and M. Serio. The nonlinear dynamics of rogue waves and holes in deep-water gravity wave trains. *Phys. Lett. A*, 275:386–393, October 2000.

[18] G. Agrawal. *Nonlinear Fiber Optics*. Academic Press, 3 edition, January 2001.

[19] A. Hasegawa and Y. Kodama. *Solitons in Optical Communications*. Oxford University Press, 1995.

[20] F. M. Mitschke and L. F. Mollenauer. Discovery of the soliton self-frequency shift. *Opt. Lett.*, 11:659–661, 1986.

[21] A. Hasegawa and F.D Tappert. Transmission of stationary nonlinear optical pulses in dispersive dielectric fibres I: Anomalous dispersion. *Appl. Phys. Lett.*, 23:142–144, 1973.

[22] L. F. Mollenauer, R. H. Stolen, and J. P. Gordon. Experimental observation of picosecond pulse narrowing and solitons in optical fibers. *Phys. Rev. Lett.*, 45:1095–1098, Sep 1980.

[23] L.H. Zhang and J.G Si. New soliton and periodic solutions of (1+2)-dimensional Nonlinear Schrödinger equation with dual-power law nonlinearity. *Commun. Nonlinear Sci. Numer. Simulat*, 15:2747–2754, 2010.

[24] V.E. Zakharov and A.B. Shabat. Exact theory of two-dimensional self-focusing and one dimensional self-modulation of waves in nonlinear media. *Soviet Phys. JETP*, 34:62–69, 1972.

[25] M. Wadati and M. Toda. The exact N-soliton solution of the modied Korteweg-de Vries equation. *J. Phys. Soc. Japan*, 32:1403–1411, 1972.

[26] M.J. Ablowitz, D.J. Kaup, A.C. Newell, and H. Segur. Method for solving the Sine-Gordon equation. *Phys. Rev. Lett.*, 30:1262–1264, 1973.

[27] R.C Cascaval, F. Gesztesy, H. Holden, and Y. Latushkin. Spectral analysis of Darboux transformations for the focusing NLS hierarchy. *J. Anal. Math.*, 93:139–197, 2004.

[28] M. Boiti and F. Pempinelli. Nonlinear Schrödinger equation, Backlund transformations and Painleve transcendents. *Nuovo Cimento B*, 59:40–58, 1980.

[29] R. Hirota. *The Direct Method in Soliton Theory*. Cambridge University Press, 2004.

[30] N.N. Akhmediev, V.M. Eleonskii, , and N.E. Kulagin. First-order exact solutions of the nonlinear Schrödinger equation. *Theoret. Math. Phys.*, 72:809–818, 2010.

[31] G.B. Whitham. *Linear and Nonlinear Waves*. New York.

[32] G. B. Whitham. Non-linear dispersive waves. *Proc. R. Soc. A. Mat.*, 283:238–261, 1965.

[33] J.C. Luke. A perturbation method for nonlinear dispersive wave problems. *Proc. R. Soc. A*, 292:403–412, 1966.

[34] M.J. Ablowitz and D.J. Benny. The evolution of multi-phase modes for nonlinear dispersive waves. *Stud. Appl. Math.*, 49:225–238, 1970.

[35] A.V. Gurevich and L.P. Pitaevskii. Nonstationary structure of a collisionless shock wave. *J. Exp. Theor. Phys.*, 65:590–604, 1974.

[36] B. Fornberg and G.B. Whitham. A numerical and theoretical study of certain nonlinear wave phenomena. *Phil. Trans. R. Soc. Lond. A*, 289:373–404, 1978.

[37] T.R. Marchant. Undular bores and the initial-boundary value problem for the modied Korteweg-de Vries equation. *Wave Motion*, 45:540–555, 2008.

[38] H. Flaschka, M. Forest, and D. McLaughlin. Multiphase averaging and the inverse spectral solution of KdV. *Commun. Pure Appl. Math.*, 33:739–784, 1979.

[39] M.G. Forest and D.W. McLaughlin. Modulations and sinh-Gordon and sine-Gordon wavetrains. *Stud. Appl. Math.*, 68:11–59, 1983.

[40] M.V. Pavlov. Nonlinear Schrödinger equation and the BogolyubovWhitham method of averaging. *Theoret. Math. Phys.*, 71:584–588, 1987.

[41] H. Flaschka, M.G. Forest, and D.W. McLaughlin. Multiphase averaging and the inverse spectral solution of the Kortewegde Vries equation. *Comm. Pur. Appl. Math.*, 33:739–784, 1980.

[42] G. A. El. Resolution of a shock in hyperbolic systems modified by weak dispersion. *Chaos: An Interdisciplinary J. Nonlinear Sci.*, 15:037103, 2005.

[43] G. A. El, R. H. J. Grimshaw, and N. F. Smyth. Unsteady undular bores in fully nonlinear shallow-water theory. *Phys. Fluids*, 18:027104, 2006.

[44] G. Assanto, T.R. Marchant, and N.F. Smyth. Collisionless shock resolution in nematic liquid crystals. *Phys. Rev. A*, 78:063808, 2008.

[45] T.R. Marchant and N.F. Smyth. Approximate techniques for dispersive shock wave in nonlinear media. *J. Nonlinear Opt. Phys.*, 21:1250035, 2012.

[46] R.H.J Grimshaw and N.F. Smyth. Resonant flow of a stratified fluid over topography. *J. Fluid Mech.*, 169:429–464, 1986.

[47] N. F. Smyth. Modulation theory solution for resonant flow over topography. *Proc. R. Soc. Lond. A*, 409:79–97, 1987.

[48] Y.S. Kivshar and G. Agrawal. *Optical solitons: From fibers to photonic crystals*. Academic Press, San Diego, 2003.

[49] W. P. Zhong and M. Beli. Kummer solitons in strongly nonlocal nonlinear media. *Phys. Lett. A*, 373:296–298, 2009.

[50] S. Suntsov, K. G. Markis, G. A. Siviloglou, R. Iwanow, R. Schiek, D. N. Christodoulides, G. I. Stegeman, R. Morandotti, H. Yang, G. Salamo, M. Volatier, V. Aimez, R. Ares, M. Sorel, Y. Min, W. Sohler, W. Xiaosheng, A. Bezryadina, and C. Zhigang. Observation of one- and two-dimensional discrete surface spatial solitons. *J. Nonlinear Opt. Phys.*, 16:401–426, 2007.

[51] C. Conti, M. Peccianti, and G. Assanto. Route to nonlocality and observation of accessible solitons. *Phys. Rev. Lett.*, 91:073901, 2003.

[52] G.C Duree, J.L Shultz, G.J Salamo, M. Segev, A. Yariv, B. Crosignani, P. Di Porto, J.K. Sharp, and R.R Neurgaonkar. Observation of self trapping of an optical beam to the photorefractive index. *Phys. Rev. Lett.*, 71:533–536, 1993.

[53] A. Pasquazi, S. Stivala, G. Assanto, J. Gonzalo, and J. Solis. Transverse nonlinear optics in heavy metal oxide glasses. *Phys. Rev. A*, 77:043808, 2008.

[54] C. Barsi, W. Wan, C. Sun, and J.W. Fleischer. Dispersive shock waves with nonlocal nonlinearity. *Opt. Lett.*, 32:2930–2932, 2007.

[55] G.Z. Zhu. Experiments on director waves in nematic liquid crystals. *Phys. Rev. Lett.*, 49:1332–1335, 1982.

[56] W. Helfrich. Alignment-inversion walls in nematic liquid crystals in the presence of a magnetic field. *Phys. Rev. Lett.*, 21:1518–1521, 1968.

[57] L. Leger. Observation of wall motions in nematics. *Solid State Commun.*, 10:697–700, 1972.

[58] L. Lin, C.Q. Shu, and G. Xu. Comment on solitary waves in liquid crystal. *Phys. Lett. A*, 109:277–278, 1985.

[59] M. Peccianti, I.B. Burgess, G. Assanto, and R. Morandotti. Space-time bullet trains via modulation instability and nonlocal solitons. *Opt. Express*, 18:5934–5941, 2010.

[60] G. Assanto and M. Peccianti. Spatial solitons in nematic liquid crystals. *J. Quantum Electron.*, 39:13–21, 2003.

[61] G. Assanto and M. A. Kapierz. Nematicons: self-localised beams in nematic liquid crystals. *Liq. Cryst.*, 36:1161–1172, 2009.

[62] A. Ashkin. History of optical trapping and manipulation of small-neutral particle, atoms, and molecules. *IEEE J. Quant. Electron.*, 6:841–856, 2000.

[63] H. L owen. Colloidal soft matter under external control. *J. Phys.: Condens. Matter*, 13:R415–R432, 2001.

[64] D.V. Grier. A revolution in optical manipulation. *Nature*, 424:810–816, 2003.

[65] J.E. Molloy and M.J. Padgett. Lights, action: Optical tweezers. *Contemp. Phys.*, 43:241–258, 2002.

[66] D. Kishan, M.D. Michael, and S. Gabriel. Optical tweezers:The next generation. *Phys. World*, 2002.

[67] I.N. Levine. *Physical chemistry*. McGraw-Hill, the University of Michigan, 6th edition, 2008.

[68] R. A. Terborg, J. P. Torres, and K. Volke-Sepulveda. Steering and guiding light with light in a nanosuspension. *Opt. Lett.*, 24:5284–5287, 2013.

[69] M.J. Maeso and J.R. Solana. Instabilities in the equations of state of hard-disk and hard-sphere fluids from the virial expansions. *J. Chem. Phys.*, 9:548–552, 1993.

[70] J. Tian, H. Jiang, Y. Gui, and A. Mulero. Equation of state for hard-sphere fluids offering accurate virial coefficients. *R. Sc. Chem: Chem. Phys.*, 11:47:11213–11218, 2009.

[71] A. Santos, M. Lopez de Haro, and S.B. Yuste. An accurate and simple equation of state for hard disks. *J. Chem. Phys*, 103:4622–4625, 1995.

[72] H. Reiss, H. L. Frisch, and J. L. Lebowitz. Statistical mechanics of rigid spheres. *J. Chem. Phys.*, 31, 1959.

[73] D. Henderson. A simple equation of state for hard discs. *Mol. Phys.*, 30:971–972, 1975.

[74] J. L. Colot and M. Baus. The freezing of hard disks and hyperspheres. *Phys. Lett. A*, 119:135–139, 1986.

[75] F .C Andrews. Simple approach to the equilibrium statistical mechanics of the hard sphere fluid. *J. Chem. Phys.*, 62:272–275, 1975.

[76] A. Baram and M. Luban. Divergence of the virial series for hard discs and hard spheres at closest packing. *J. Phys. C: Solid State Phys.*, 12:L659–L664, 1979.

[77] L. V. Woodcock. Hard-sphere fluid equation of state. *J. Chem. Soc., Faraday Trans. 2*, 72:731–735, 1976.

[78] J. J. Erpenbeck and M. Luban. Equation of state of the classical hard-disk fluid. *Phys. Rev. A*, 32:2920–2922, 1985.

[79] I. C. Sanchez. Virial coefficients and closepacking of hard spheres and disks. *J. Chem. Phys.*, 101:7003–7006, 1994.

[80] J.H. Dymond and E.B. Smith. *The virial coefficients of pure gases and mixtures: a critical compilation*. Oxford science research papers. Clarendon Press, 1980.

[81] T.R. Marchant and N.F. Smyth. Solitary waves and their stability in colloidal media: Semi-analytical solutions. *Dyn. Contin. Discret. I*, 19:525–541, 2012.

[82] M. Matuszewski, W. Krolikowski, and Y.S. Kivshar. Spatial solitons and light-induced instabilities in colloidal media. *Opt. Express*, 16:1371–1376, 2008.

[83] M. Matuszewski, W. Krolikowski, and Y.S. Kivshar. Bistable solitons in colloidal media. *Photon. Lett. Poland*, 1:4–6, 2009.

[84] A. Azmi and T.R Marchant. Colloidal solitary waves with temperature dependent compressibility. *J. Opt.*, 16:055203, 2014.

[85] A.H. Harvey and E.W. Lemmon. Correlation for the second virial coefficient of water. *J. Phys. Chem. B*, 106:5500–5505, 2002.

[86] A. Striolo, J. Ward, J.M Prausnitz, W.J Parak, D. Zanchet, D. Gerion, D. Milliron, and A.P Alivisatos. Molecular weight, osmotic second virial coefficient, and extinction coefficient of colloidal CdSe nanocrystals. *J. Phys. Chem. Ref. Data*, 33:369–376, 2004.

[87] A. Striolo, C. Mc Cabe, and P.T. Cummings. Effective interactions between polyhedral oligomeric sislesquioxanes dissolved in normal xexadecane from molecular simulation. *Macromolecules*, 38:8950–8959, 2005.

[88] J. Tian and Y. Gui. Equations of state for fluids: empirical temperature dependence of the second virial coefficient. *J. Phys. Chem. B*, 111:10970–10974, 2007.

[89] C. Barsi, W. Wan, C. Sun, and J. W. Fleischer. Dispersive shock waves with nonlocal nonlinearity. *Opt. Lett.*, 32:2930–2932, 2007.

[90] W. Wan, S. Jia, and J. W. Fleischer. Dispersive, superfluid-like shock waves in nonlinear optics: Properties and interactions. In *Conference on Lasers and Electro-Optics/Quantum Electronics and*

Laser Science Conference and Photonic Applications Systems Technologies, page QME2. Optical Society of America, 2007.

[91] W. Wan, D. V. Dylov, C. Barsi, and J. W. Fleischer. Dispersive shock waves with negative pressure. In *Conference on Lasers and Electro-Optics/International Quantum Electronics Conference*, page IThM5. Optical Society of America, 2009.

[92] W. Wan, D. V. Dylov, C. Barsi, and J. W. Fleischer. Diffraction from an edge in a self-focusing medium. *Opt. Lett.*, 35:2819–2821, 2010.

[93] Z. Chen, M. Segev, S. R. Singh, T. H. Coskun, and D. N. Christodoulides. Sequential formation of multiple dark photorefractive spatial solitons: experiments and theory. *J. Opt. Soc. Am. B*, 14:1407–1417, 1997.

[94] G. Couton, H. Maillotte, and M.Chauvet. Self-formation of multiple spatial photovoltaic solitons. *J. Opt. B: Quantum S. O.*, 6:S223–S230, 2004.

[95] T.R. Marchant and N.F. Smyth. Semi analytical solutions for dispersive shock waves in colloidal media. *J. Phys.B: At. Mol. Opt. Phys.*, 45:145401, 2012.

[96] R. El-Ganainy, D.N. Christodoulies, C. Rostchild, , and M. Segev. Soliton dynamics and self-induced transparency in nonlinear suspensions. *Opt. Express*, 15:10207–10218, 2007.

[97] A. Alberucci, G. Assanto, D. Buccoliero, A. Desyatnikov, T.R. Marchant, and N.F Smyth. Modulation analysis of boundary induced motion of nematicons. *Phys. Rev. A*, 79:043186, 2009.

[98] W.L. Kath and N.F. Smyth. Soliton evolution and radiation loss for the nonlinear Schrödinger equation. *Phys. Rev. E*, 51:1484–1492, 1995.

[99] A.A. Minzoni, N.F. Smyth, and A.L. Worthy. Modulation solutions for nematicon propagation in non-local liquid crystal in the nonlocal limit. *Phys. D*, 237:1549–1556, 2008.

[100] G. Assanto, B.D. Skuse, and N.F. Smyth. Optical path control of spatial solitary waves in dye-doped nematic liquid crystals. *Photon. Lett. Poland*, 1:154–156, 2009.

[101] G. Assanto, B.D. Skuse, and N.F. Smyth. Solitary wave propagation and steering through light-induced refractive potentials. *Phys. Rev. A*, 81:063811, 2010.

[102] A. E. Kaplan. Bistable solitons. *Phys. Rev. Lett.*, 55:1291–1294, 1985.

[103] J. Yang and T.I Lakoba. Accelerated imaginary-time evolution methods for the computation of solitary waves. *Stud. Appl. Math.*, 120:265–292, 2008.

[104] M.I Weinstein. Nonlinear Schrödinger equations and sharp interpolation estimates. *Comm. Math. Phys.*, 87:567–576, 1983.

[105] A. Azmi and T. R. Marchant. Dispersive shock waves in colloids with temperature dependent compressibility. *J. Nonlinear Opt. Phys.*, Submitted, 2014.

[106] S. A. Arrhenius. Über die Dissociationswärme und den Einflußder Temperatur auf den Dissociationsgrad der Elektrolyte. *Z. Physik. Chem.*, 4:96–116, 1889.

[107] B. Liu and T. R. Marchant. The microwave heating of three-dimensional blocks: semi-analytical solutions. *IMA J. Appl. Math.*, 67:145–175, 2002.

[108] T.R Marchant and B. Liu. On the heating of a two-dimensional slab in a microwave cavity: Aperture effects. *J. ANZIAM*, 43:137–148, 2001.

[109] G. A. El, A. V. Gurevich, V. V. Khodorovskii, and A. L. Krylov. Modulational instability and formation of a nonlinear oscillatory structure in a focusing medium. *Phys. Lett. A*, 177:257–361, 1993.

[110] A.M. Kamchatnov, S.A. Darmanyan, and F. Lederer. Formation of solitons on the sharp front of the pulse in an optical fiber. *Phys. Lett. A*, 245:259 – 264, 1998.

[111] N. Ghofaniha, C. Conti, G. Ruocco, and S. Trillo. Shocks in nonlocal media. *Phy. Rev. Lett.*, 99:043903, 2007.

[112] J. Yang and T. I. lakoba. Accelerated imaginary-time evolution methods for the computation of solitary waves. *Stud. Appl. Math.*, 120:265–292, 2008.

[113] J. Yang. Newton-conjugate-gradient methods for solitary wave computations. *J. Comp. Phys.*, 228:7007–7024, 2009.

[114] J.R. Douglas and H.H. Rachford. On the numerical solution of heat conduction problems in two and three space variables. *Tr. A.M.S.*, 82:421–439, 1956.